

NANOGENERATORS FOR SELF-POWERED APPLICATIONS

A Dissertation
Presented to
The Academic Faculty

by

Guang Zhu

In Partial Fulfillment
of the Requirements for the Degree
Doctor of Philosophy in the
School of Materials Science and Engineering

Georgia Institute of Technology
May 2013

COPYRIGHT 2013 BY GUANG ZHU

NANOGENERATORS FOR SELF-POWERED APPLICATIONS

Approved by:

Dr. Zhong Lin Wang, Advisor
School of Materials Science and
Engineering
Georgia Institute of Technology

Dr. Naresh N Thadhani
School of Materials Science and
Engineering
Georgia Institute of Technology

Dr. Gleb Yushin
School of Materials Science and
Engineering
Georgia Institute of Technology

Dr. Meilin liu
School of Materials Science and
Engineering
Georgia Institute of Technology

Dr. Yulin Deng
School of Chemical and Biomolecular
Engineering
Georgia Institute of Technology

Dr. Benjamin Klein
School of Electrical and Computer
Engineering
Georgia Institute of Technology

Date Approved: April 01, 2013

ACKNOWLEDGEMENTS

Foremost, I would like to express my sincere gratitude to my advisor Prof. Zhong Lin Wang for the continuous support of my Ph.D study and research, for his trust, motivation, enthusiasm, immense knowledge, and personal support to me through the last four and half years. What he taught me was far beyond lab and research, which will keep motivating me to become a person with love, integrity, and goal, no matter what I do in the future. He is absolutely the best advisor that any student can ever wish for. I could not have imagined having a better mentor for my Ph.D study.

Besides my advisor, I would like to thank the rest of my thesis committee: Prof. Naresh N Thadhani, Prof. Gleb Yushin, Prof. Meilin liu, Prof. Yulin Deng, and Prof. Benjamin Klein, for their encouragement, insightful comments, and hard questions.

My sincere thanks also go to Prof. Rusen Yang at the University of Minnesota who used to be a postdoc in our group when I started my Ph.D study. It was him that taught me the experimental skills, answered my sometimes naïve questions, and offered support when I encountered problems in personal life.

I thank my fellow labmates in this lovely group: Chen Li, Prof. Yong Qin, Prof. Zhou Li, Yusheng Zhou, Jun Chen, Peng Bai, for the stimulating discussions, for the sleepless nights we were working together before deadlines, and for all the fun we have had in the last four and half years.

Last but not the least, I would like to thank my beloved ones. My parents Prof. Qi Zhu and Prof. Chunmei Ren gave birth to me at the first place and supported me spiritually throughout my life. I apologize for not being able to be on their side on

holidays, festivals, and special occasions. Their love is absolutely unconditional and supported me through hard times. Finally, I am grateful for my girlfriend, Xuebei Yu, for her unreserved support in the last three years. We travelled back and forth between Atlanta and Seattle where she works in the last two years for every three months. I should give apology for not being able to answer her phones when doing experiments, for not being able to take care of her when she was ill. I thank her with all my heart for her understanding and continuous love.

TABLE OF CONTENTS

	Page
ACKNOWLEDGEMENTS	iii
LIST OF FIGURES	viii
SUMMARY	xi
<u>CHAPTER</u>	
1 INTRODUCTION	1
1.1 Motivation	1
1.2 Mechanical-electrical energy transduction mechanisms	2
1.3 Thesis scope	4
2 ZINC OXIDE NANOWIRE BASED NANOGENERATOR	5
2.1 Zinc oxide nanowires	5
2.1.1 Crystal structure of Zinc oxide	5
2.1.2 Electrical property of zinc oxide	7
2.1.3 Piezoelectric properties of zinc oxide	9
2.1.4 Synthesis of zinc oxide nanowires by vapor method	9
2.2 Nanogenerators based on zinc oxide nanowires	10
3 LATERALLY INTEGRATED ZINC OXIDE NANOWIRE BASED NANOGENERATOR	15
3.1 Design and fabrication	15
3.2 Synthesis of ultra-long vertically aligned ZnO NWs	19
3.3 Electric measurement results and discussion	27
3.4 Summary	29
4 VERTICALLY INTEGRATED ZINC OXIDE NANOWIRE BASED NANOGENERATOR	31

4.1	Introduction	31
4.2	Design and fabrication	31
4.3	Electric measurement results and discussion	34
4.4	Summary	38
5	TRIBOELECTRIC NANOGENERATOR, CONCEPT AND THEORY	39
5.1	Introduction	39
5.2	Structure and fabrication	39
5.3	Fundamental mechanism	40
5.3.1	Open-circuit voltage	41
5.3.2	Short-circuit current	43
5.4	Electric measurement results and discussion	45
6	SCALABLE TRIBOELECTRIC NANOGENERATOR	51
6.1	Introduction	51
6.2	Structure and fabrication	52
6.3	Operation principle	54
6.4	Electric measurement results and discussion	56
6.5	Summary	62
7	SLIDING MODE OF TRIBOELECTRIC NANOGENERATOR	63
7.1	Introduction	63
7.2	Non-grating design	64
7.2.1	Structure and fabrication	64
7.2.2	Fundamental mechanism	65
7.2.3	Electric measurement results and discussion	71
7.3	Grating design	73
7.3.1	Structure and fabrication	73

7.3.2 Operation principle	74
7.3.3 Electric measurement results and discussion	76
7.4 Summary	82
8 SELF-POWERED APPLICATIONS	84
8.1 Storage-assisted applications for laterally integrated ZnO NW based nanogenerator	84
8.2 Real time applications	87
8.2.1 Functional electrical simulation by vertically integrated ZnO NW based NG	87
8.2.2 Electrochemical deposition by triboelectric NG	89
8.2.3 Powering LEDs by scalable triboelectric NG	92
9 CONCLUSION	94
REFERENCES	96

LIST OF FIGURES

	Page
Figure 2.1: Wurtzite structure of ZnO	6
Figure 2.2: Principle of the observed power-generation process of a piezoelectric ZnO NW	11
Figure 3.1: Experimental setup for transferring vertically grown ZnO NWs to a flexible substrate	16
Figure 3.2: SEM image of vertically grown ZnO NWs by physical vapor method on Si substrate	16
Figure 3.3: SEM image of as transferred horizontal ZnO NWs on a flexible substrate	17
Figure 3.4: Fabrication process for the laterally integrated NGs	18
Figure 3.5: Schematics of operating principles of the laterally integrated NGs	19
Figure 3.6: Schematic illustration of source material preparation and horizontal furnace system for the synthesis of ultra-long ZnO NW arrays.	20
Figure 3.7: SEM images of the synthesized ultralong vertically ZnO NW arrays on Si substrate	22
Figure 3.8: Structural and compositional characterization results of the ultralong ZnO NW	23
Figure 3.9: TEM image at the interface area between the grown ZnO crystal and the substrate, with catalyst particles highlighted by circles and arrows. Inset is the dark field TEM image of the interfacial area	24
Figure 3.10: HRTEM image of a single catalyst particle, revealing {111} surface of gold crystal.	24
Figure 3.11: SEM images of the ultralong ZnO NW arrays on different substrates	25
Figure 3.12: Schematic illustration of the ZnO NW growth process via three-stage mechanism.	26
Figure 3.13: Electric measurement results of the laterally integrated NG	28
Figure 3.14: Dependence of the laterally integrated NG's electric power output on strain and strain rate	29

Figure 4.1: Fabrication process of the vertically integrated NG	32
Figure 4.2: SEM images of the vertically integrated NG that show its structure	34
Figure 4.3: Electric measurement results of the vertically integrated NGs	35
Figure 4.4: Finite element calculation of the potential distribution across the nanogenerator under a stress of 1 MPa	36
Figure 4.5: Analysis of the merit of the segmented design	37
Figure 4.6: Electric measurement results of a NG pad that consists of 9 vertically integrated NGs in parallel connection	38
Figure 5.1: Sketch of the generator's structure and materials selection. The polymer nanowires (PNWs) are depicted with a different color from the substrate for clear visualization	40
Figure 5.2: Sketch that illustrates the operating principle of the generator under open-circuit condition	41
Figure 5.3: Sketch that illustrates the operating principle of the generator under short-circuit condition.	44
Figure 5.4: Electric measurement results of the triboelectric NG that works in contact mode	46
Figure 5.5: Dependence of the triboelectric NG's output power on external load resistance	48
Figure 5.6: Dependence of the triboelectric NG's output power on surface modification	49
Figure 6.1: Structure and fabrication process of the scalable triboelectric NG	53
Figure 6.2: Operating principle of the scalable triboelectric NG	55
Figure 6.3: Electric measurement results of the scalable triboelectric NG	57
Figure 6.4: Dependence of the I_{sc} on the contacting force	58
Figure 6.5: Dependence of the scalable triboelectric NG on external resistance	59
Figure 7.1: Structure of the triboelectric NG on sliding mode	65
Figure 7.2: Simulation results that show the operating principle of the sliding triboelectric NG	66

Figure 7.3: A schematic to illustrate the calculation of open-circuit voltage V_{oc} and the definition of the parameters.	67
Figure 7.4: Electric potential difference between the aluminum electrode and the copper electrode as a function of the displacement	70
Figure 7.5: A cycle of electricity generation process for illustrating the mechanism of the TEG	71
Figure 7.6: Current output of the sliding triboelectric NG	72
Figure 7.7: Electric measurement results of the sliding triboelectric NG	73
Figure 7.8 Fabrication process of a grating TEG.	74
Figure 7.9: Electric measurement results of the sliding triboelectric NG that has two gratings	76
Figure 7.10: Detailed examinations on electric measurement results of the sliding triboelectric NG that has two gratings	78
Figure 7.11: Current output results of the sliding triboelectric NG that has multiple gratings	79
Figure 7.12: Dependence of the sliding NG's output power on the number grating units	80
Figure 7.13: Different configurations in which the sliding mode can be applied	82
Figure 8.1: Powering a LED by a laterally integrated NG with storage assisted self-powered mode	85
Figure 8.2: Pictures that visualize real-time stimulation of the functional electrical stimulation by the NG pad	88
Figure 8.3: Experimental setup for electrodeposition	89
Figure 8.4: Electric measurement results of the contact triboelectric NG as the power source for electrodeposition	91
Figure 8.5: Results of the electrodeposition powered by the contact triboelectric NG	92
Figure 8.6: Pictures that show the scalable triboelectric NG as a power source for hundreds of LED bulbs	93

SUMMARY

We are surrounded by enormous amounts of ambient mechanical energy that goes to waste such as rain drops, human footfalls, air flow, ocean waves, just to name a few. If such otherwise wasted mechanical energy can be effectively converted into electricity, self-powered electronics are very likely to be realized, which can address the limitations of traditional power supplies in many cases, such as wireless sensor networks. Here in this work, two types of energy-harvesting nanogenerators (NGs) based were studied.

For piezoelectric nanogenerators, zinc oxide (ZnO) nanowires (NWs) were used as building blocks to develop integrated NGs based on a number of ZnO NWs instead of a single NW. Two types of integrated NGs were developed, which consist of lateral NW arrays and vertical NW arrays. The electric output power was substantially enhanced compared to the design with a single NW.

For triboelectric nanogenerators, triboelectric effect was innovatively used as an effective means of harvesting mechanical energy. The operating principle can be explained by the coupling between triboelectric and electrostatic effect. Two types of operating modes were invented, i.e. contact mode and sliding mode. Triggered by commonly available ambient mechanical energy such as footfalls, the maximum output power reached up to 1.2 W.

More importantly, self-powered systems were built by using the NG as a power source. It can provide real time power for up to 600 commercial LED bulbs. This research not only provides the fundamentals for NGs but also demonstrates the practicability of using the self-powered technology in our daily life.

CHAPTER 1

INTRODUCTION

1.1 Motivation

With the threat of global warming and energy crises, searching for renewable and green energy resources is one of the most urgent challenges to the sustainable development of human society. On the large scale, in addition to the well-known energy resources that power the world today, such as petroleum, coal, hydroelectricity, and natural gas, people are exploring alternative energy resources such as wind, solar energy, geothermal energy, biomass, and nuclear energy. At the much smaller scale, energy is also desperately needed to power small electronics, including independent, wireless, and maintenance-free sensor networks, micro-electromechanical systems (MEMS), and even portable/wearable personal electronics¹. However, when addressing the needs of small-scale electric power, traditional solutions such as city power and batteries have apparent limitations in many cases, which can be well elaborated by the following cases. For example, people have to measure the inclination and cracks of an underground tunnel to prevent catastrophic accident. Although wireless sensor networks that consist of a large number of stand-alone sensor nodes are well qualified for performing the monitoring task, proper power source to these sensor units are not readily available. The city power does not normally reach remote areas where tunnels are usually built; and it is impractical to equip every sensor unit with a battery simply because replacing batteries for thousands of sensors is unacceptably costly. A similar example is industrial sites where people need to measure the temperature, strain and vibration of equipment for preventive maintenance not responsive maintenance to drastically reduce maintenance cost and to shorten down time. Another example is patients who have pacemakers. They have to receive painful and dangerous surgeries in every five years to replace the battery. Besides, scientists who

study wild animals, such as sharks, may only be able to track them for a few months by attachable wireless trackers because batteries die out. Therefore, it is a real pain that traditional power solutions have limitations

This problem can be properly addressed if ambient energy can be effectively harvested and converted into electricity, building self-powered autonomous electronics. Photovoltaic, thermal electricity are the well-established technology for energy harvesting⁴. However, solar cells are only effective enough when exposed to adequate sunlight; and thermal gradient greater than 10°C is difficult to be found within a small volume, which greatly limits the efficiency of thermal-electric conversion². Taking the forms of irregular air flow/vibration, ultrasonic waves, body movement and hydraulic pressure, mechanical energy is ubiquitously available in our living environment around the clock. It covers a wide range of magnitude and frequency from cell contraction to ocean waves. If only a small fraction of such energy could be converted into electricity, it may be sufficient to power small electronics. Therefore, it is highly desirable to develop innovative approaches for converting ambient mechanical energy into electric energy.

1.2 Mechanical-electrical energy transduction mechanisms

For the conversion from mechanical energy to electrical energy, there are four transduction mechanisms, including piezoelectric effect, electrostatic effect, electromagnetic effect, and triboelectric effect. For generators based on each of these mechanisms, they have respective advantages as well as limitations.

Electrostatic generators utilize the relative movement between electrically isolated charged capacitor plates to generate energy. The work done against the electrostatic force between the plates provides the electrical energy. Electrostatic generators are effective in energy conversion. However, they require pre-charging on capacitor plates by a voltage source in order to get ‘jump started’³. Besides, fabrication process that makes micro-

sized features for enhancing conversion efficiency may greatly add cost to the electrostatic generator.

Electromagnetic induction, first discovered by Faraday in 1831, is the generation of electric current in a conductor located within a magnetic field. The conductor typically takes the form of a coil and the electricity is generated by either the relative movement of the magnet and coil, or because of changes in the magnetic field. This traditional technique takes a simple design⁴⁻⁶. However, reliance on specific magnetic materials not only leads to hardly reduced cost but also large volume provided that effective conversion is to be achieved.

Piezoelectric generators employ active materials that generate charges when they are mechanically stressed, converting mechanical energy into electricity. Conventional piezoelectric generators have piezoelectric cantilevers that vibrate at resonating frequency. However, this technique suffers some drawbacks, such as high cost on synthesis of high-quality piezoelectric materials, sophisticated fabrication process, and specific resonating frequency^{7,8}. In recent years, a series of rationally designed and cost-effective nanogenerators (NGs) based on piezoelectric zinc oxide (ZnO) nanowires (NWs) have shown great potential to scavenge tiny and irregular mechanical energy of low frequency⁹⁻¹⁴. But insufficient electric output still hinders their practical applications.

For triboelectric generators, they utilize triboelectric effect to generate contact charges on the surface of two different materials and build up the charges for a high voltage. This technique has little constraint on materials because theoretically any two different materials can produce surface charges upon contact because of the triboelectric effect. However, previously developed triboelectric generators were only applied to produce high voltage, not to harvest ambient mechanical energy. Besides, they are extremely bulky in size, which is not suitable as power sources for small electronics.

1.3 Thesis scope

The ultimate mission of energy harvesting technology is to realize self-powered electronics that are used in people's daily life. By doing so, we can replace, at least offset, the reliance of small electronics on traditional power supplies. When traditional power supplies have limitations for a particular case, self-powered technique can become a practical solution. If a technology is ever to be commercialized and transformed to true products on the market, one of the most important factor that determines whether it can successfully gain market share is how much it costs.

For the transduction mechanisms that are introduced above, piezoelectric nanogenerators and triboelectric generator have the advantage of relatively low cost when compared with the other two. Therefore, these two types of generators are targets of my research. While taking the advantage of low cost, I need to address respective limitations for each of the two generators in order to develop practical power source for self-powered electronics. For nanowire-based piezoelectric nanogenerators, the research goal is to substantially boost up the electric output power. For triboelectric generator, novel design needs to be developed for miniaturized triboelectric generator. Besides, new mechanism is also to be explored so that the triboelectric effect can be utilized for the purpose of energy harvesting, not just for producing a high voltage. Another important topic of the thesis is to investigate self-powered applications. Based on the specific needs of actual cases, different modes of the self-powered systems need to be developed. By successfully demonstrating the operation of various self-powered systems, the thesis not only provide theoretical justification but also experimental support to the fact the self-powered technology is very likely to be brought into people's daily in the near future.

CHAPTER 2

ZINC OXIDE NANOWIRE BASED NANOGENERATOR

2.1 Zinc oxide nanowires

2.1.1 Crystal structure of Zinc oxide

As a II–VI compound semiconductor, the ionicity of ZnO resides at the borderline between the covalent and ionic semiconductors. The crystal structures are shared by hexagonal wurtzite, cubic zinc blende, and rocksalt. Under ambient environments, the thermodynamically stable phase is wurtzite structure where each anion is surrounded by four cations at the corners of a tetrahedron, and vice versa. The zinc blended structure for ZnO is only stable when growing on cubic substrates; and rocksalt structure can only be obtained at high pressure.

The ZnO wurtzite structure has a hexagonal unit cell. The edge length of the basal plane hexagonal is universally designated as parameter a ; and the unit cell height is defined as the axial lattice parameter c perpendicular to the basal plane. For ideal wurtzite structure, the two lattice parameters have a ratio of $c/a = \sqrt{8/3} = 1.633$. The point group and space group belong to $6mm$ and $P6_3mc$, respectively, in the international notation. The structure can be disassembled into two interpenetrating hexagonal close-packed (hcp) sublattices. Each sublattice contains a type of atoms (Zn atoms or O atoms) which are displaced with respect to each other along the c -axis. Each hcp sublattice includes four ions per unit cell, with every ion surrounded by four ions of opposite charge which are coordinated at the corners of the tetrahedron. The crystallographic vectors are denoted as: $\vec{a} = a(1/2, \sqrt{3}/2, 0)$, $\vec{b} = a(1/2, -\sqrt{3}/2, 0)$, $\vec{c} = a(0, 0, c/a)$.

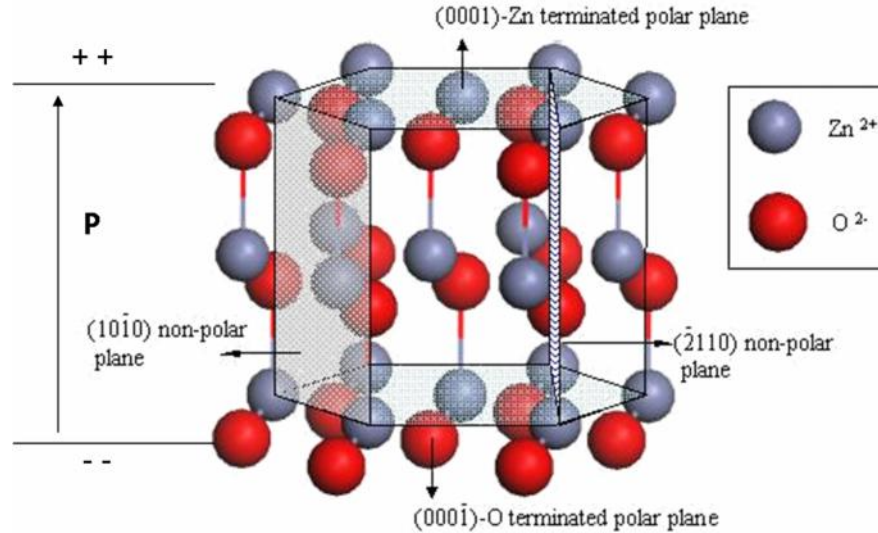


Figure 2.1 Wurtzite structure of ZnO

The main defects in the as-grown ZnO single crystal are point defects, including intrinsic defects and incorporated impurities. In the following, the properties of native point defects and doping impurities will be briefly summarized.

Oxygen vacancy (V_o), which behaves as a donor, is probably the most mentioned defect in the ZnO. Since the as-grown ZnO materials naturally exhibit n-type conductivity, for a long time, oxygen vacancies have often been invoked as source of the unintentional n-type conductivity because of the evidence that the electrical conductivity of ZnO increases with the decrease of oxygen partial pressure and that the oxygen vacancy has low formation energy. However, recent studies showed that an oxygen vacancy is a very deep rather than shallow donor, and thus cannot make contribution to n-type conductivity, which means that an oxygen vacancy is stable at neutral state in n-type ZnO at equilibrium contribution¹⁵.

From crystal structure point of view, a zinc interstitial (Zn_i) is supposed to occupy either the octahedral site or the tetrahedral site. For the tetrahedral site, the zinc interstitial has one Zn and one O atom as the nearest neighbor; for the octahedral site, the zinc interstitial has three Zn and three O atoms as the nearest neighbor. The distance to the

nearest neighbor at octahedral site is larger than that of the tetrahedral site. So it is expected that the Zn interstitial is more favorable to form in the octahedral site. This prediction has been confirmed that the Zn interstitial at the tetrahedral will spontaneously relaxes to the octahedral site¹⁶. It has been found that the Zn interstitial is a shallow donor, because which it was regarded to be partially responsible for the unintentional n-type conductivity. But recent research found that the Zn interstitial has a high formation energy, which makes it in very low concentrations in n-type ZnO and not be able to contribute to n-type conductivity¹⁷.

A zinc vacancy (V_{Zn}) is an electron acceptor, which can accept up to two additional electrons. Since the as-grown material is naturally a n-type semiconductor, the formation energy of a zinc vacancy as a donor is very low; actually it has the lowest formation energy among the native point defects, which indicates that modest concentration of the zinc vacancy is expected to be present in the n-type ZnO¹⁷. Also it has been recently found that zinc vacancy is likely to be responsible for a broad and weak green luminescence of ZnO¹⁸.

Other intrinsic point defects, including zinc antisites, oxygen interstitials and oxygen antisites, have high formation energies; therefore they are expected not to have much effect on the properties of ZnO under equilibrium conditions¹⁷.

2.1.2 Electrical property of zinc oxide

As a II–VI compound semiconductor, ZnO belongs to direct semiconductor and has a wide band gap of 3.37 eV at room temperature. All the as synthesized ZnO structures are found to naturally exhibit n-type conductivity without intentional doping. Typically, the donor concentration is on the order of 10^{17} per cubic centimeter. For a long time, the natural behavior was generally attributed to native point defects, such as oxygen vacancies and zinc interstitials. But recent research may suggest

other possible reasons, such as the presence of hydrogen interstitials or hydrogen substitution sites. The cause of unintentional n-type conductivity has recently been related to the incorporation of donor impurities such as hydrogen. It was found that hydrogen interstitials are likely to be responsible for the n-type conductivity of ZnO. A hydrogen interstitial behaves as a shallow donor. Besides interstitial positions, hydrogen was recently found to be able to replace oxygen as a substitutional hydrogen, which is also a shallow donor¹⁷. Hydrogen is always present for current techniques that are used to grow ZnO, including vapor phase transport, hydrothermal method, chemical vapor deposition, and pulsed laser deposition. Even in the ultra-high vacuum environment for MBE, the background concentration of hydrogen is still possible to introduce high-solubility contamination. In addition to hydrogen, fluorine is another known donor impurity that forms shallow donor in ZnO.

For a long time, it was very difficult to achieve p-type doping for many reasons¹⁷. First, progress towards understanding the unintentional n-type conductivity in ZnO was not made until recently. Second, there are only very limited options in making shallow acceptor doping. Substitutional doping from column-IA elements, such as Li, Na, and K, are deep acceptors and do not contribute to p-type conductivity. The same situation applies to column-IB elements, including Cu, Ag, and Au. For the column-V elements, such as P, As, and Sb, substitution on O sites also results in deep acceptors. Third, the defects such oxygen vacancies and zinc interstitials are source of compensation in p-type ZnO. It was found that nitrogen is suitable as a p-type dopant to form shallow acceptor because the atomic size and electronegativity of nitrogen are close to those of oxygen. Although some groups have achieved p-type doping by nitrogen, the stability of the doping is still in question.

As a semiconductor, the contact between ZnO and metals is an important aspect in its properties. Theoretically speaking, the contact characteristic is governed by the relative magnitude of the metal work function and the semiconductor electron affinity.

For n-type semiconductor, which is the case for ZnO, if the metal work function is larger than the electron affinity of the semiconductor, Schottky contact forms; otherwise, the contact has ohmic transport characteristic. Experimentally, stable Schottky contact can be achieved between ZnO and high work function metals, such as Pt and Au.

2.1.3 Piezoelectric properties of zinc oxide

Due to the lack of an inversion plane perpendicular to the c-axis, ZnO is a piezoelectric material, which becomes electrically polarized when subjected to a mechanical stress; conversely it experience a strain in response to an applied electric field. Because of the absence of centrosymmetry, surfaces have either Zn polarity designated as (0001), or O polarity designated as $(000\bar{1})$. Conventionally, the [0001] axis pointing from the face of the O plane to Zn plane is referred as positive c-axis. Therefore, when the bonds along the c-direction are from Zn cations to oxygen anions, the polarity is described as Zn polarity; otherwise, the polarity is referred to as O polarity. Many properties of ZnO are directly related to its polarity, such as spontaneous polarization, and piezoelectricity. Besides the primary polarity plane, there are some other important non-polar planes, including $(11\bar{2}0)$ (or a-plane) and $(1\bar{1}00)$ (or m-plane).

2.1.4 Synthesis of zinc oxide nanowires by vapor method

Among the thermal evaporation methods, the most reported method is the carbothermal reduction method, which has the vapor-liquid-solid (VLS) mechanism¹⁹. The source material is the mixture of ZnO powder and graphite powder of equal weight; and it is put at the center of a tube. At increased temperature, carbothermal reduction process occurs, leading to the release of Zn vapor. A thin layer of gold, or pre-synthesized gold nanoparticles, is used as a catalyst on a substrate positioned at downstream of the

tube, With constant incoming Zn vapor, the percentage of Zn components in the catalyst droplet increases and ultimately supersaturates; and Zn is precipitated out at the solid-liquid interface, which is then oxidized into ZnO by the oxygen in the carrier gas.

2.2 Nanogenerators based on zinc oxide nanowires

In recent years, Z.L. Wang's group has demonstrated a series of rationally designed NGs with one-dimensional ZnO nanowires⁹⁻¹⁴. ZnO is a very attractive material for semiconductor device applications. It has a direct and wide band gap ($E_g=3.37$ eV) in the near-UV spectral region, and a large free-exciton binding energy (60 meV). Besides, it is a piezoelectric material due the lack of centrosymmetry; and Zhao et al.'s²⁰ measurements showed that ZnO NWs exhibit even larger piezoelectric coefficient than that of the bulk. In 2006, Wang and Song⁹ proposed and demonstrated the basic concept of the ZnO-based NG with an atomic force microscope (AFM) (Figure 2.1). In the contact mode, a constant normal force was applied between an AFM tip coated with a Pt film and a vertical ZnO NW grown on a grounded conductive solid substrate. The as-synthesized ZnO NW is generally n-type in nature; thus it forms Schottky contact with the Pt coated AFM tip, which is a high work function metal. When the tip slowly pushes the NW, a positive piezoelectric potential is created because of the tensile strain; and the local potential difference between the tip and the NW results in reverse biased Schottky contact. Thus electrons from the ground cannot go through the interface and therefore accumulate at the tip. As the tip continuous to move to the compressive side of the NW, the local negative piezoelectric potential because of the compressive strain leads to forward biased Schottky contact. Then transient flow of electrons from the NW to the tip creates circular motion of the charge carriers. A maximum voltage output of 30 mV was obtained for a single NW. In essential, the principle of the NG is a transient flow of electrons in an external load as driven by the piezopotential; and the requisite Schottky

contact acts as a “gate” that holds and releases the electrons. Control experiments based on ohmic contact result in no detectable signal.

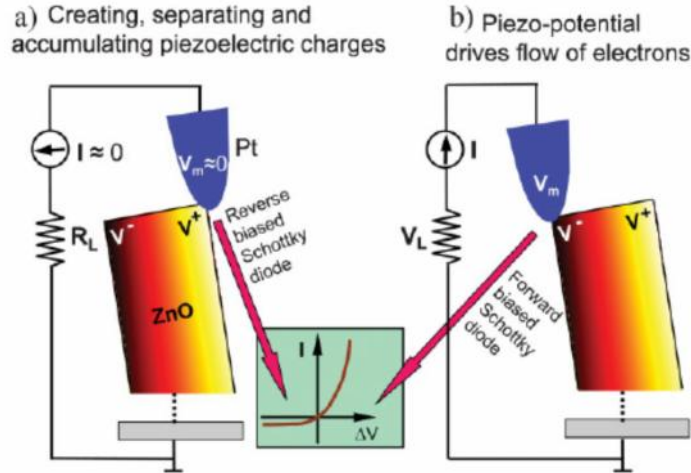


Figure 2.1. Principle of the observed power-generation process of a piezoelectric ZnO NW. Reverse and forward biased Schottky contact between the AFM tip and the ZnO NW due to the presence of the respectively positive and negative piezopotential at the contact area.

The advantages by ZnO NW based energy harvesting technology are described as follows². First, the ZnO NW can be subjected to extremely large deformation without plastic deformation or fracture, which ensures the stability and robustness of the NG. Second, the ZnO NW based generator can be triggered by small force, which makes it unique for harvesting energy from weak mechanical disturbance. Third, ZnO NWs with controlled density and position can be easily grown on almost any substrate at low temperature such that they are feasible for micro/nanosystem integration. Fourth, ZnO is a biocompatible, nontoxic, and environmentally friendly material, which makes it possible for developing in vivo implantable ZnO NW based generators.

As for practical applications, the AFM tip needs to be replaced by a fixed electrode, and a large number of NWs working simultaneously needs to be integrated. X.

Wang et al.¹¹ fabricated an integrated NG by putting an inverse v-shaped electrode coated with Pt on vertically grown ZnO NW arrays. Under external excitation, such as ultrasonic wave, the NWs are bent by the top electrode. As long as the compressive side gets in touch with the electrode, piezopotential drives electrons through the forward biased Schottky contact. Respectively, current and voltage output reached 500 nA and 10 mV. As for this design, the output current is the sum of those NWs that can actively contribute to the output, but the voltage is determined by a single NW because the NWs are essentially in parallel. The apparent drawback of this design is that though dense enough, the randomly distributed NWs have a variation in length, and only a fraction of NWs with the proper length can actively contribute to electric energy generation. An effort was made by Xu et al.¹³ to integrate layers of such NGs in serial to increase the voltage output. Though successful four-layer integration was demonstrated, the complexity in fabrication reduced the stability of the device; and the voltage output (62 mV) was still well below the threshold of the diodes used in conventional rectification circuits. Besides, the source of excitation (ultrasonic wave) was not always available under many circumstances; and a more universal approach needed to be developed.

More recently, Yang et al.¹⁴ demonstrated power generation with horizontally packaged single ZnO NW. The NW was bonded at both ends by metal electrodes on the surface of a flexible polymer substrate. Owing to much smaller diameter of the NW compared to the substrate thickness, outward bending of the substrate induces a uniaxial tensile strain in the NW. Due to the piezoelectric property of the ZnO NW, the strain results in a piezoelectric field along the length, with one end being positive and the other being negative. Electrons in the external circuit driven by the potential difference accumulate at the electrode end with positive piezopotential, where the presence of reverse biased Schottky contact blocks them from flowing through the interface. This process continues until the Fermi levels of the two electrodes are lined up, reaching to a new equilibrium. Upon releasing of the tensile strain, disappearance of the piezoelectric

potential will lead to back flow of the accumulated electrons, returning the system to its original states. As a result, the bending and releasing of the single-wire-NG gives rise to an alternating flow of the charges in the external circuit, with an output voltage of 50 mV. For this design, as long as the flexible substrate undergoes mechanical deformation, the power generation process can be triggered with little requirement on the forms of excitation.

Meanwhile, other groups have also been exploring this rising field. Using ZnO NWs or other one-dimensional piezoelectric materials, novel ideas were come up with; and some promising prototypes have been demonstrated²¹⁻²⁴. By virtue of the transparency of the ZnO materials, researchers from Kim's group²¹ developed a transparent flexible NG with a design similar to that of Wang's. ZnO nanorods were grown on a flexible indium tin oxide (ITO)-coated polymer substrate. Embossed top electrode was made of palladium gold, which forms Schottky contact with ZnO NWs. By pushing the top electrode with an external force, they obtained a maximum current density of 1 $\mu\text{A cm}^{-2}$. Most recently, they improved the robustness of the NG by replacing the ITO electrodes by graphene sheets, on which ZnO nanorods were epitaxially grown to form heterogeneous nanostructure²². The current density was increased to 2 $\mu\text{A cm}^{-2}$. Similar to Yang et al.'s¹⁴ design, Chang et al.²³ from Li's group fabricated a piezoelectric polymeric nanogenerator. Instead of horizontally bonded ZnO NWs, they made use of poly(vinylidene fluoride) (PVDF) nanofibers which were electrospun by means of near-field electrospinning with in situ mechanical stretching and electrical poling. Their measurement results were in good agreement with those done by Yang et al's on ZnO NWs. Besides, Qi et al.²⁴ achieved transferring of PZT micro-ribbons on a rigid substrate to a flexible substrate by dry transfer process, representing a feasible approach for implementing wearable energy harvesters.

However, for the already developed NGs up to date, insufficient electric output still impedes the practical applications. Therefore, a flexible, robust, and high output NG

needs to be developed so that it can be integrated in electric circuit to actually power functional electronics.

CHAPTER 3

LATERALLY INTEGRATED ZINC OXIDE NANOWIRE BASED NANOGENERATOR

3.1 Design and fabrication

The mechanism of converting mechanical energy by a single ZnO NW that is laterally bonded to a substrate has been discussed in details in our previous report¹⁴. Owing to much smaller diameter of the NW compared to the substrate thickness, outward bending of the substrate induces a uniaxial tensile strain in the NW. Due to the piezoelectric property of the ZnO NW, the stress results in a piezoelectric field along the length, which causes a transient charge flow in the external circuit. The Schottky contact at the bonded ends can regulate the charge flow. As a result, the bending and releasing of the single-wire-NG gives rise to an alternating flow of the charges in the external circuit. In this work, the power output has been scaled up with the integration of hundreds of thousands of horizontally-aligned NWs, which was made by a scalable sweeping-printing-method that is simple, cost-effective and highly efficient.

The method consists of two main steps. In the first step, the vertically-aligned NWs are transferred to a receiving substrate to form horizontally-aligned arrays. The major components of the transfer setup are two stages (Figure 3.1a). Stage 1 has a flat surface that faces downwards and holds the vertically-aligned NWs; stage 2 has a curved surface and holds the receiving substrate. Polydimethylsiloxane (PDMS) film on the surface of stage 2 is used as a cushion layer to support the receiving substrate and enhances the alignment of the transferred NWs. The radius of the curved surface of stage 2 equals the length of the rod supporting the stage, which is free to move in circular motion. In the second step, electrodes are deposited to connect all of the NWs together.

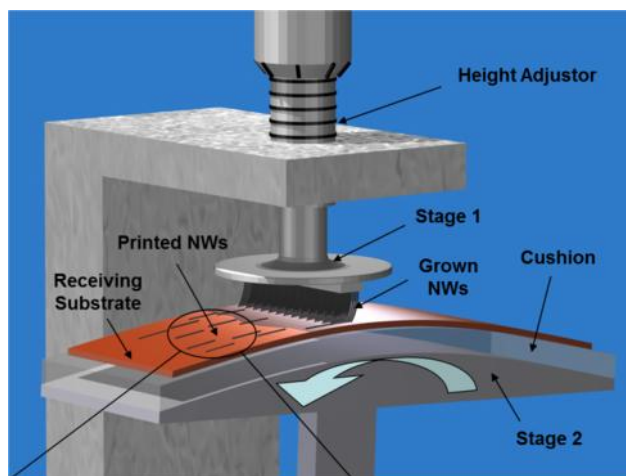


Figure 3.1 Experimental setup for transferring vertically grown ZnO NWs to a flexible substrate

Vertically-aligned ZnO NWs on Si substrates were synthesized using physical vapor deposition method²⁵⁻²⁶. The dense and uniform NWs have the length of $\sim 50\ \mu\text{m}$, diameter of $\sim 200\ \text{nm}$, and growth direction along c-axis (Figure 3.2). The same growth direction of NWs guarantees the alignment of the piezoelectric potentials in all of the NWs and a successful scaling up of the output, which will be elaborated later.

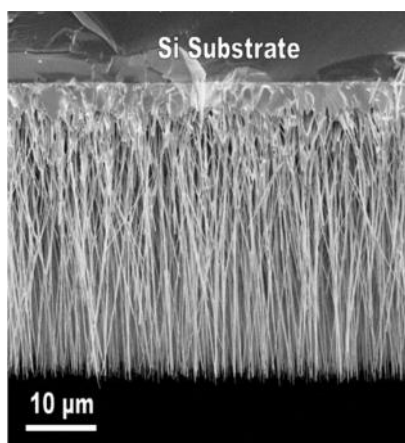


Figure 3.2 SEM image of vertically grown ZnO NWs by physical vapor method on Si substrate

A small piece of Si substrate with grown ZnO NWs was mounted onto stage 1 (Figure 3.1) and a piece of Kapton® film with the thickness of 125 μm was attached to stage 2 (Figure 3.1). The distance between the receiving substrate and NWs was precisely controlled to form a loose contact between the two. The receiving substrate then counterclockwise swept across the vertical NWs arrays, which were detached from Si substrate and aligned on the receiving substrate along the direction of sweeping due to the applied shear force (Figure 3.1). The as-transferred NWs are presented in Figure 3.3, with an estimated average density of $1.1 \times 10^6 \text{ cm}^{-2}$. The length variation is probably due to the fact that not all of the NWs were broken off at the roots.

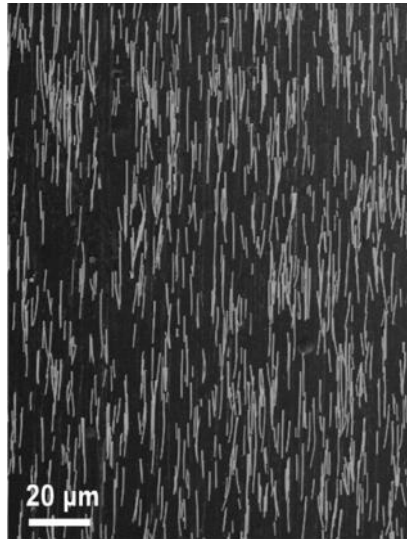


Figure 3.3 SEM image of as transferred horizontal ZnO NWs on a flexible substrate

Next, the evenly spaced electrode pattern over the aligned NWs was first defined using photolithography and then followed by sputtering 300 nm thick Au film (Figure 3.4A). After the lifting off the photoresist, 600 rows of stripe-shaped Au electrodes with 10 μm spacing were fabricated on top of the horizontal NW arrays (Figure 3.4B). Au electrodes form Schottky contacts with the ZnO NWs, which are mandatory for a working NG^{9,27}. Approximately 3.0×10^5 NWs in an effective working area of 1 cm^2 , as

pointed by an arrowhead in Figure 3.4B (inset), are in contact with electrodes at both ends. Finally, a PDMS packaging over the entire structure can further enhance mechanical robustness and protect the device from invasive chemicals.

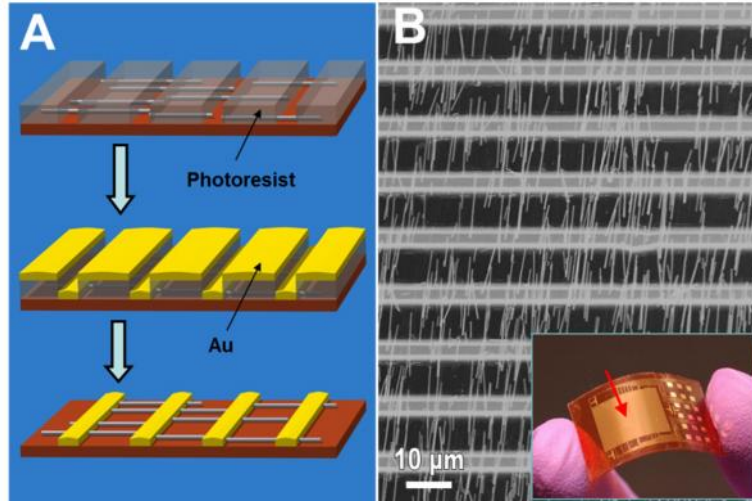


Figure 3.4 Fabrication process for the laterally integrated NGs. (A) Process of fabricating Au electrodes on horizontal ZnO NW arrays, which includes photolithography, metallization, and lift-off. (B) SEM image of ZnO NW arrays bonded by Au electrodes. Inset: demonstration of the as fabricated NG. The arrow indicates to the effective working area of the NG.

The working principle of the NG is illustrated by the schematic diagrams in Figure 3.5A, NWs connected in parallel collectively contribute to the current output; and NWs in different rows connected in serial constructively improve the voltage output. It is worth noting that, the same growth direction of all NWs and the sweeping printing method ensure that the crystallographic orientations of the horizontal NWs are aligned along the sweeping direction. Consequently, the polarity of the induced piezopotential is also aligned, leading to a macroscopic potential contributed constructively by all of the NWs (Figure 3.5B).

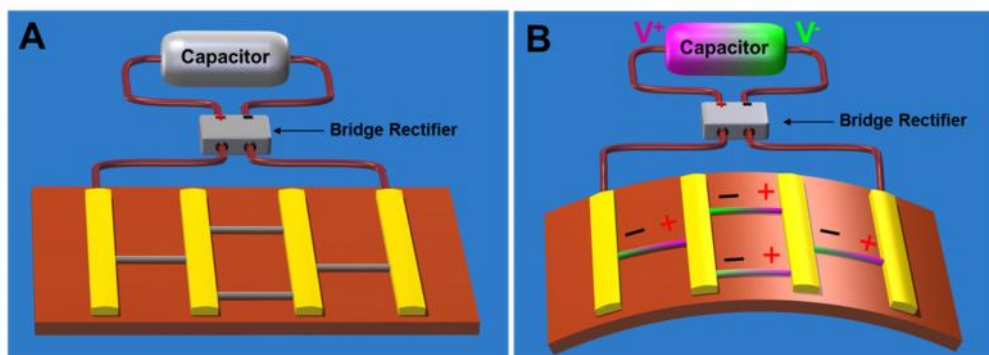


Figure 3.5 Schematics of operating principles of the laterally integrated NGs. (A) Schematic diagram of NG's structure without mechanical deformation, in which gold is used to form Schottky contacts with the ZnO NW arrays. (B) Demonstration of output scale up when mechanical deformation is induced, where the “+/-” signs indicate the polarity of the local piezoelectric potential created in the NWs.

3.2 Synthesis of ultra-long vertically aligned ZnO NWs

In the last decade, one-dimensional (1D) ZnO nanostructures, such as nanowires (NWs), nanobelts, and nanorods have been receiving considerable attention due to their unique properties as an electronic and optical material^{25,28-30}. A variety of ZnO NW based devices have been demonstrated, including field effect transistors³¹⁻³³, UV lasers³⁴⁻³⁵, light emitting diodes³⁶⁻³⁸, solar cells³⁹⁻⁴¹, photodetectors⁴²⁻⁴⁴, nano-generators^{9,11,14} and nano-piezoelectronics^{45,46}. As the basis for various applications, synthesis with control over size, orientation, and density is of great significance and very much desired. Main synthesis techniques include physical vapor deposition^{25,47-49}, chemical vapor deposition⁵⁰⁻⁵³, pulsed layer deposition⁵⁴ and wet chemical method⁵⁵⁻⁵⁷. For the widely employed vapor transport method, different growth mechanisms have been reported, including catalyst-assisted vapor-liquid-solid (VLS) growth and catalyst-free vapor solid (VS) growth. On one hand, VLS mechanism usually yields ZnO NWs with size and orientation uniformity, but residual metal catalyst particles often stay at the tips of NWs⁵⁸, which is very detrimental to further device integration because those particles

prevent intimate contact between NWs and electrode materials. Besides, as demonstrated by previous reports, the length of ZnO NWs grown from VLS mechanism is limited to only a few micrometers⁵⁰⁻⁵². On the other hand, methods with VS mechanism can grow ZnO NWs with length up to hundreds of micrometers, which nevertheless generally have rather poor alignment and uniformity^{25,59}. Here we report a general technique of synthesizing ultra-long ZnO NWs with great vertical alignment on different substrates, with length and aspect ratio exceeding 130 μm and 500, respectively. More importantly, pre-deposited metal catalysts were experimentally confirmed at the root instead of tip end of the NWs. Furthermore, a series of control experiments were conducted to shed light on the actual growth mechanism. Finally, a unique growth model was proposed, combining VLS and VS growth in three consecutive stages. Our synthesis technique opens up the path of fabricating various functional devices based on high-quality ZnO NW arrays.

Limited length of NWs synthesized by chemical vapor transport method is possibly due to relatively low reactive vapor concentration in the tube and thus slow growth speed. To address this issue, two strategies were employed in our work. The first one involves careful pretreatment of source materials, as schematically illustrated in Figure 3.6.

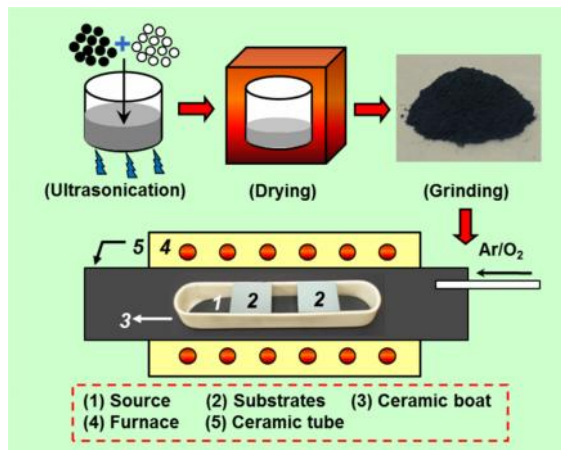


Figure 3.6 Schematic illustration of source material preparation and horizontal furnace system for the synthesis of ultra-long ZnO NW arrays.

Rather than simply grinding conventionally used ZnO powder and graphite powder for mixing, we used 1g of commercially available ZnO nanopowder and 1g of active carbon as source materials and dispersed them in ethanol. The suspension was ultrasonicated for 30 min to ensure uniform dispersion. Then it was put in a hot oven at 90 °C for another 30 min for drying. After the ethanol completely vaporized, the dried mixture was then well ground and ready for use. The use of small-sized source materials and the pretreatment measures are expected to largely increase the amount of reactive vapor released during the growth. The second strategy was to adjust the conventional synthesis configuration in which source materials and substrates are separately located at the center and downstream side of the furnace tube, respectively. As shown on the bottom of Figure 3.6, the already prepared source materials were transferred to an alumina boat. Precleaned silicon wafers (100) were cut to 1.8 cm X 1.8 cm pieces and rinsed by acetone, methanol, and isopropyl alcohol for 30 s, respectively. After being e-beam evaporated a 2-nm gold layer, the substrates were horizontally mounted on top of the boat with the gold layer facing down. This non-conventional configuration is expected to greatly increase the local concentration of the reactive vapor at the growth site and the growth speed as a result⁶⁰. The boat was then placed at the center of the furnace tube. Then temperature was ramped up to 960 °C at a rate of 60 °C/min with a constant flow of carrier gas (30 sccm of argon and 10 sccm of oxygen). After 30 min of reaction, the furnace was waited to cool down to ambient temperature for product collection.

The synthesized ZnO NWs are extremely long with a length up to 130 um (Figure 3.7A). They are very well aligned at vertical orientation and densely packed with great size uniformity (Figure 3.7B). For comparison, using traditional ZnO powder and graphite as source materials without previously described pretreatment yielded only a few micrometer NWs with less density and more random orientations. It is noteworthy that

there is a ZnO crystal film at the junction between the NWs and the substrate. Reports concerning this so called buffer layer or seed layer have been published. Some researchers took the opinion that this layer was deposited on the substrate first and then subsequent nucleation and growth of the NWs followed⁶¹. But some others believed that it was the convergence of the adjacent NWs that led to the formation of a continuous film. However, the origin of such a layer still remains controversial⁴⁹.

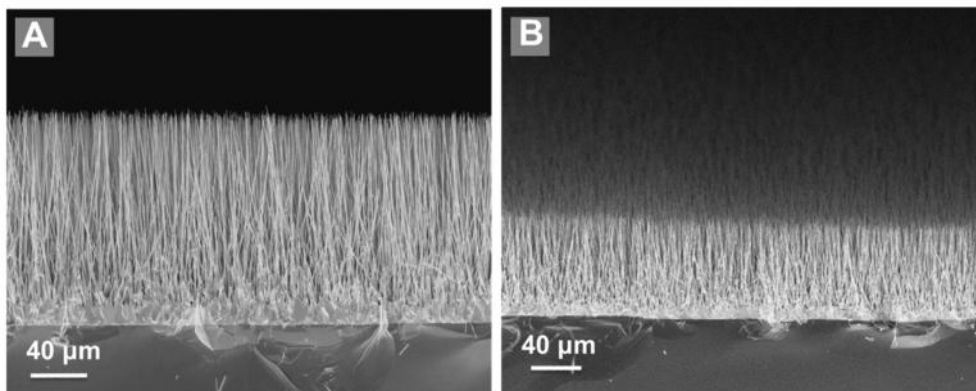


Figure 3.7 SEM images of the synthesized ultralong vertically ZnO NW arrays on Si substrate. (A) Cross-sectional view of the synthesized ZnO NWs on Si substrate. (B) 60° tilted view of the synthesized ZnO NWs on Si substrate.

The crystal structure of the NWs was characterized by x-ray diffraction (XRD) and transmission electron microscope (TEM). The XRD patterns reveal that the synthesized NWs are single crystalline ZnO (Figure 3.8A). Apparently, a strong (002) peak is overwhelmingly predominant with other peaks almost negligible, indicating uniform orientation as well as great density of the NWs. A TEM image of a single NW (Figure 3.8B) shows a typical diameter of 250 nm. The selected-area electron diffraction (SAED) pattern proves again single crystalline nature of the NW and exhibits the growth along the [0001] direction (right inset of Figure 3.8B). It is observed from the TEM image that the NW tip seems to be free of any catalyst particle. SAED pattern acquired at the tip shows no pattern other than ZnO crystal (left inset of Figure 3.8B). Besides, EDS

spectrum measured at the tip also gives no trace of gold element (Figure 3.8C), confirming that the gold catalysts are absent from the tip end.

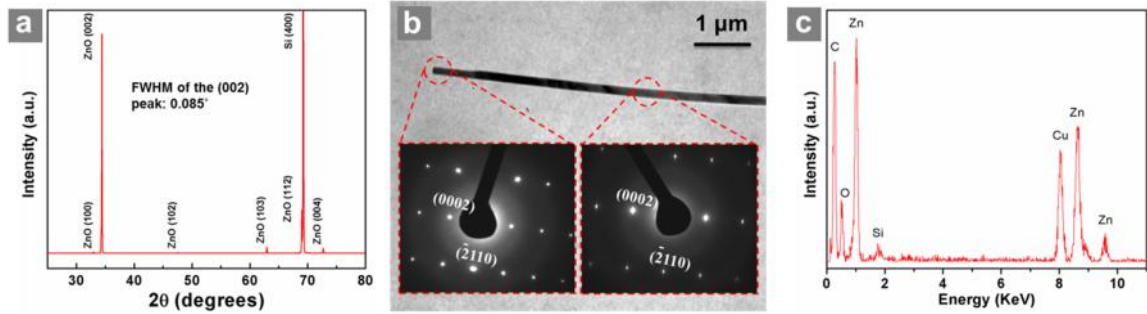


Figure 3.8 Structural and compositional characterization results of the ultralong ZnO NW. (A) X-ray diffraction patterns of the as-grown vertical aligned ZnO NWs on Si (100). (B) TEM image of a single ZnO NW. Insets are selected-area electron diffraction patterns at the tip (left) and the body (right). (C) Energy dispersive spectrum acquired at the tip of the NW.

Though the observation that catalyst-assisted growth produces NWs with catalyst-free tip ends has been reported^{9,11,60,62-64}, very few successful attempts were made to determine the underlying reason. Some researchers believed that the catalyst was doped into the NW as contamination⁴⁸, while some others suggested it evaporating during the growth process^{9,11}. However, convincing experimental results lacked. In this report, we prepared extremely thin cross-sectional samples for TEM characterization. The TEM image targeting at the NW-substrate interfacial area reveals a very interesting phenomenon. A layer of particles can be clearly spotted at the root of the NWs, which are highlighted in Figure 3.9. It is noticeable that they do not adhere closely to the underlying substrate and that their respective distance away from the substrate varies. The dark field TEM image (inset of Figure 3.9) reveals the continuous ZnO film lying between the NWs and the substrate to be a textured layer, which is composed of adjacent crystal domains.

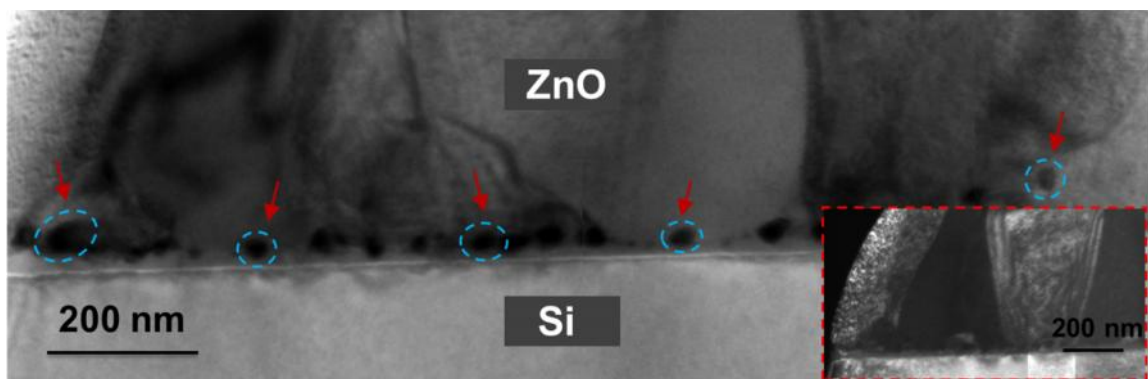


Figure 3.9 TEM image at the interface area between the grown ZnO crystal and the substrate, with catalyst particles highlighted by circles and arrows. Inset is the dark field TEM image of the interfacial area

High resolution transmission diffraction (HRTEM) image of a single particle exhibits a set of lattice planes with a measured distance of 2.355 \AA , corresponding to $\{111\}$ of gold crystal. The decisive experimental evidence confirms that metal catalyst stays at the root of the synthesized ZnO NWs. This phenomenon is a strong indication that the ZnO NW synthesis using our technique is not simply governed by the VLS mechanism, which is in consistent with previous report by Fan et al⁶².

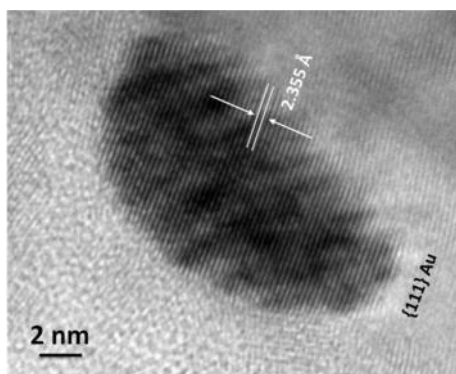


Figure 3.10 HRTEM image of a single catalyst particle, revealing $\{111\}$ surface of gold crystal.

Such unexpected discovery raises two important questions, i.e. how the metal catalyst winds up staying at the interfacial area and what role it plays during the growth

process. To shed light on the actual growth mechanism, a series of control experiments were performed.

In the first group, no gold catalyst was pre-deposited on the substrate, while other experimental parameters remained unchanged. As a result, NW growth was not observed, which is a strong proof that the gold catalyst is indispensable for initializing the growth^{60,64}.

In the second group, a sputtered ZnO film as a seed layer (~100nm) was prepared on bare Si substrate surface, and no catalyst was applied. The growth result was presented in Figure 11A. Vertically oriented ZnO NWs with a length of tens of micrometers were successfully synthesized, indicating that VS growth should be governing if a seed layer is provided^{48,49,61}.

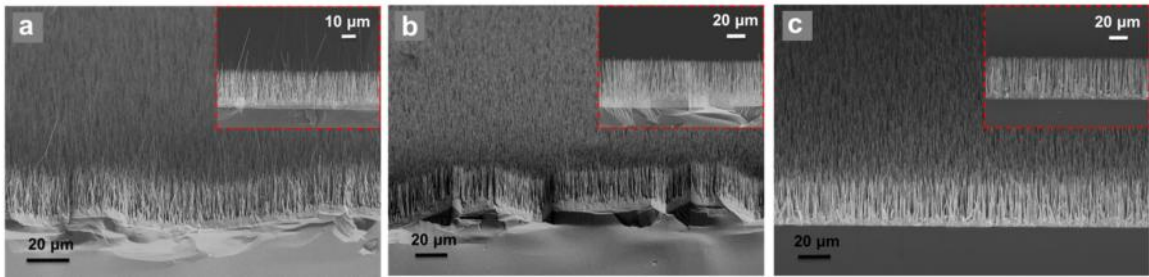


Figure 3.11 SEM images of the ultralong ZnO NW arrays on different substrates. (A) 60° tilted view of the synthesis result on ZnO substrate, with no catalyst applied before growth. Inset is the cross-sectional view. (B) 60° tilted view of the synthesis result on ITO substrate, with catalyst applied before growth. (C) 60° tilted view of the synthesis result on SiO₂ substrate, with catalyst applied before growth.

In the third group, ITO film (~100nm) was sputtered on Si bare substrate surface, followed by e-beam evaporating a 2-nm gold layer. Ultra-long ZnO NW arrays were synthesized with high quality, as shown in Figure 11B. Other substrates, such as thermally grown SiO₂, yielded similar results (Figure 11C). It is a strong indication that the growth is truly catalyst-assisted. As long as the gold catalyst is provided, the growth can take place no matter what the underlying substrate is. In addition, this observation

proves that our synthesis technique is very general, which is applicable to other substrates besides Si wafer. Therefore, various heterojunctions are expected to be formed.

Based on our characterization analysis and control groups, we propose a three-stage growth model, as schematically illustrated in Figure 3.12. During the growth, Zn vapor is generated by carbon-thermal reaction1



Another possible reaction that is worth consideration is27



Since our experimental design will lead to very high local concentration of Zn vapor and oxygen gas, reaction 2 is likely to be favorable, thus ample of ZnO vapor is anticipated. Between Zn vapor and ZnO vapor, which one would participate in the NW growth depends on the surface condition of the substrate.

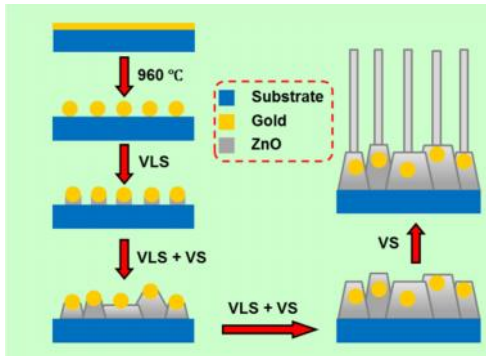


Figure 3.12 Schematic illustration of the ZnO NW growth process via three-stage mechanism.

In the early stage, it is the Zn vapor that can be easily dissolved into gold particles to form liquid alloys. Upon supersaturation, it reacts with oxygen, precipitating out very thin ZnO textured seeds beneath the catalyst particles. Thus the first stage is purely dominated by VLS growth.

Then the seeds provide nucleation and growth sites for ZnO vapor^{48,62}. The abundant and continuous arrival of ZnO vapor makes it possible for very rapid VS growth⁶⁰, which may far exceed VLS growth. Consequently, the catalyst particles will soon be submerged because of the VS growth, which can explain why the catalyst particles do not stick to the undying substrate but are encapsulated by ZnO crystal. Therefore, in the second stage, though VLS growth does not cease, it is the VS growth that prevails.

In the last stage, catalyst particles have been isolated from the reagent vapor and do not play any role afterwards. As a result, only VS mechanism contributes to further growth of ZnO NWs⁴⁸. Therefore, based on our model, the metal catalyst mainly plays two roles. First, it is crucial for initializing the growth by absorbing Zn vapor. Second, it precipitates ZnO texture seeds, which not only provides templates for further growth but also guides growth orientation, leading to alignment of the NWs.

3.3 Electric measurement results and discussion

In order to investigate the performance of the NG, a linear motor was used to periodically deform the NG in a cyclic stretching-releasing agitation (0.33 Hz). The open-circuit voltage (V_{oc}) and the short-circuit current (I_{sc}) were measured with caution to rule out possible artifacts¹⁹. At a strain of 0.1% and strain rate of $5\% \text{ s}^{-1}$, peak voltage and current reached up to 2.03 V and 107 nA, respectively (Figure 3.13). Assuming that all of the integrated NWs actively contribute to the output, the current generated by a single NW is averaged to be $\sim 200 \text{ pA}$; and the voltage from each row is $\sim 3.3 \text{ mV}$ in average. Considering the size of the working area of the nanogenerator (1 cm^2), a peak output power density of $\sim 0.22 \text{ } \mu\text{W}/\text{cm}^2$ has been achieved, which is over twentyfold increase compared to our latest report based on a more complex design¹⁴. For nanowires with the diameter of $\sim 200 \text{ nm}$, the power volume density is $\sim 11 \text{ mW}/\text{cm}^3$, which is 12-22 times of

that from PZT based cantilever energy harvester⁶⁵⁻⁶⁶. The durability test and further characterization were performed, which prove the stability and robustness of the NGs.

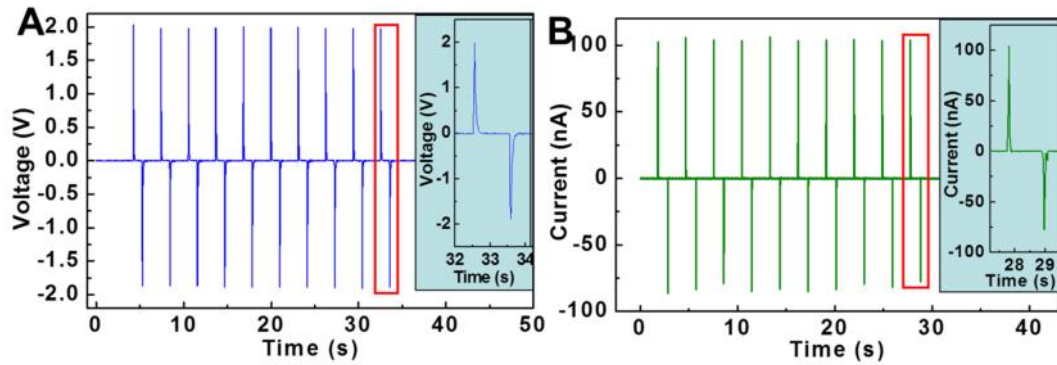


Figure 3.13 Electric measurement results of the laterally integrated NG. (A) Open circuit voltage measurement of the HONG. (B) Short circuit current measurement of the NG. The measurement is performed under a strain of 0.1% and strain rate of $5\% \text{ s}^{-1}$, with the deformation frequency of 0.33Hz. The insets are the enlarged view of the boxed area for one cycle of deformation.

Further scaling up the power output is expected to be technically feasible. If NWs can be uniformly and densely packed as a monolayer over the entire working area, and all can actively contribute to the output, the maximum power area density is expected to reach $\sim 22 \mu\text{W}/\text{cm}^2$. The power volume density is anticipated to be improved up to $\sim 1.1 \text{ W}/\text{cm}^3$. With 20 layers of such NW arrays stacked together, the power area density would be boosted up to $\sim 0.44 \text{ mW}/\text{cm}^2$.

The performance of the NG is affected by strain and strain rate. For a given strain rate ($5\% \text{ s}^{-1}$), an increase in strain leads to a larger output (Figure 3.14 A B). Likewise, at a constant strain (0.1%), the output is proportional to the strain rate (Figure 3.14 C D). Beyond a certain strain and strain rate, saturation of the magnitude occurs, probably due to the converse piezoelectric effect, which is the strain created by the piezopotential and it is opposite to the externally induced strain. It is noticed that 0.1% strain is sufficient to

induce effective output, which is much smaller than the 6% fracture strain of the ZnO NW predicted theoretically⁶⁷.

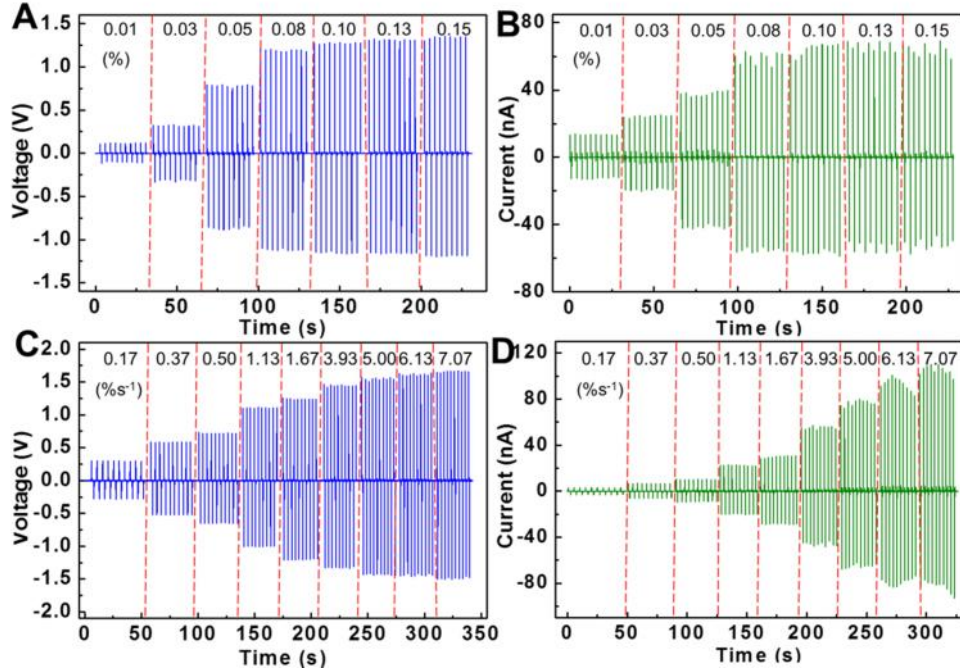


Figure 3.14 Dependence of the laterally integrated NG's electric power output on strain and strain rate. (A) Open circuit voltage measurement of the NG with increasing strain at a given strain rate of 5% s⁻¹. (B) Short circuit current measurement of the NG with increasing strain at a given strain rate of 5% s⁻¹. (C) Open circuit voltage measurement of the NG with increasing strain rate at a constant strain of 0.1%. (D) Short circuit current measurement of the NG with increasing strain rate at a constant strain of 0.1%. For all measurement, the mechanical deformation frequency is fixed at 0.33 Hz.

3.4 Summary

In summary, we have successfully fabricated high-output flexible nanogenerators using a sweeping-printing method. We managed to transfer vertically grown ZnO NWs to a flexible substrate and achieved horizontally aligned NW arrays that have crystallographic alignment, based on which an innovatively designed NG was fabricated. The electrical output of the NG reached a peak voltage of 2.03 V and current of 107 nA,

with a peak power density of $\sim 11 \text{ mW/cm}^3$, which is 12-22 times of that from PZT based cantilever energy harvester. An effective energy generation efficiency of 4.6% was demonstrated. This is a key step that is likely to bring nanogenerator based self-powering technology into people's daily life, with potential applications in mobile electronics, health monitoring, environmental inspection, cargo shipping tracking system, infrastructure monitoring and even defense technology.

CHAPTER 4

VERTICALLY INTEGRATED ZINC OXIDE NANOWIRE BASED NANOGENERATOR

4.1 Introduction

The modern life is inexorably dependent on emerging technologies in stand-alone portable systems designed to provide complete and personal solutions⁶⁸. Integration of microto-nanosized sensors, actuators/transducers, and medical implants leads to ultraminiaturized and multifunctional smart systems that are expected to provide unprecedented life quality for human kinds^{1,69,70}. For such a system that consumes much less power than do their bulky counterparts, it is not only significant but also very feasible to harvest ambient energy to build self-powered systems that can operate independently and sustainably. Here, we achieved real-time functional electrical stimulation (FES) of a sciatic nerve of a frog by a new type of ZnO-nanowire (NW)-based nanogenerator (NG) that produced electricity from biomechanical energy. The electric output from the NG reached a record high of 58 V and 134 μ A, with a maximum power density of 0.78 W/cm³. It was sufficient to directly and instantaneously induce innervating of the motor never and hence contraction of the frog's gastrocnemius muscle. Our demonstration suggests potential applications of the nanogenerator in biomedical and neurological fields, such as the power source for neuroprosthetic devices.

4.2 Design and fabrication

Since 2005, we have been developing "self-powered nanotechnology" by ZnO-nanowire-based NGs^{9,71}. By virtue of the piezoelectric effect of ZnO NWs, the NGs target ambient mechanical energy, transforming it into electrical energy. As a result of

worldwide efforts, such a concept is being developed into a practical technology with a variety of demonstrated applications⁷²⁻⁷⁸. However, a major limitation was that the output power of a NG was still not sufficiently high enough for real-time operation of conventional electronics.

The previously designed NGs utilized the Schottky barrier between metal–semiconductor contacts, which was required for charge accumulation^{11,14,79}. In this work we developed a novel design and process flow for fabricating an integrated NG based on position-controlled vertical ZnO NWs. The Schottky contact was replaced by a thin insulating layer that prevents the current leakage through the internal structure. The process flow for fabrication is shown in Figure 4.1.

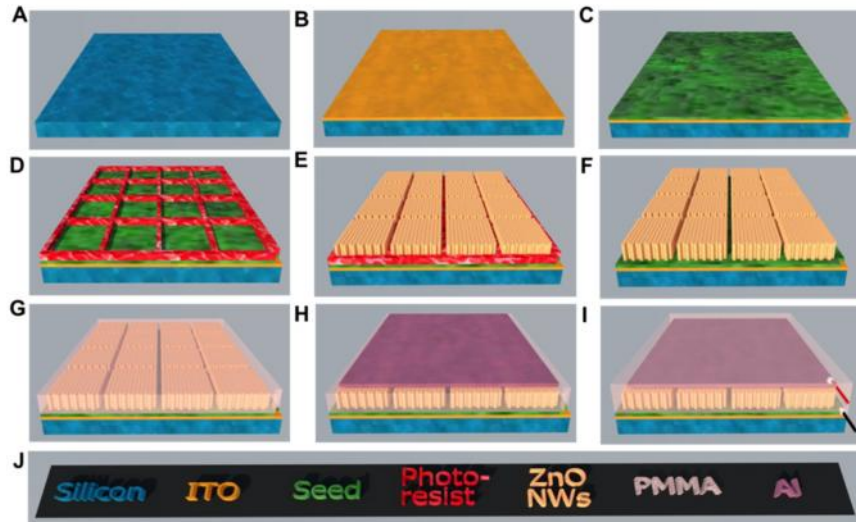


Figure 4.1 Fabrication process of the vertically integrated NG. (A) Silicon substrate. (B) Deposition of an ITO layer by sputtering. (C) Deposition of a ZnO seed layer by sputtering. (D) Window opening by photolithography. (E) Selective growth of ZnO NWs on the window areas by hydrothermal method. (F) stripping off residual photoresist by acetone. (G) Spin-coating a PMMA layer to cover the structure. (H) Deposition of a metal layer as an electrode by e-beam evaporation. (I) Packaging by spin-coating another PMMA layer. j, Legend of the figure.

A precleaned silicon substrate was consecutively deposited with an ITO layer and a ZnO seed layer by RF sputtering (Figure 4.1A-C). Not only does the ITO layer play a role as a conductive electrode, but also it promotes adhesion between the ZnO seed and the substrate. Photolithography was then performed to open an array of square windows on photoresist with narrow spacing in between (Figure 4.1D). The photoresist serves as a mask so that ZnO NWs only grow on the exposed seed surface in the subsequent synthesis step by wet chemical method (Figure 4.1E). Following stripping off any residual photoresist (Figure 4.1F), the NWs were thermally annealed. Then a layer of PMMA was applied to cover the synthesized NWs (Figure 4.1G) by spin-coating, followed by depositing a top metal electrode of aluminum (Figure 4.1H). Finally, another layer of PMMA was used for packaging (Figure 4.1I). Two terminal leads rested on the ITO layer and the aluminum layer for electrical measurement. The process flow is compatible with batch fabrication techniques, which allow multiple silicon wafers to be parallel processed, followed by being diced into individual devices. Therefore, it is superior in terms of production scale-up and cost reduction.

The result of the position-controlled synthesis is shown in Figure 4.2. ZnO NWs grew only in designated areas defined by photolithography (Figure 4.2B). Such a design improves not only the effectiveness of NWs for energy harvesting but also the robustness of the NG for defect toleration because each unit can work independently. The high-magnification SEM image shows that the NWs are aligned vertically (Figure 4.2C). They are so densely grown that most of them are connected or even merged together (Figure 4.2D). The cross-sectional view of the structure (Figure 4.2E) reveals closely packed NWs that are submerged in PMMA.

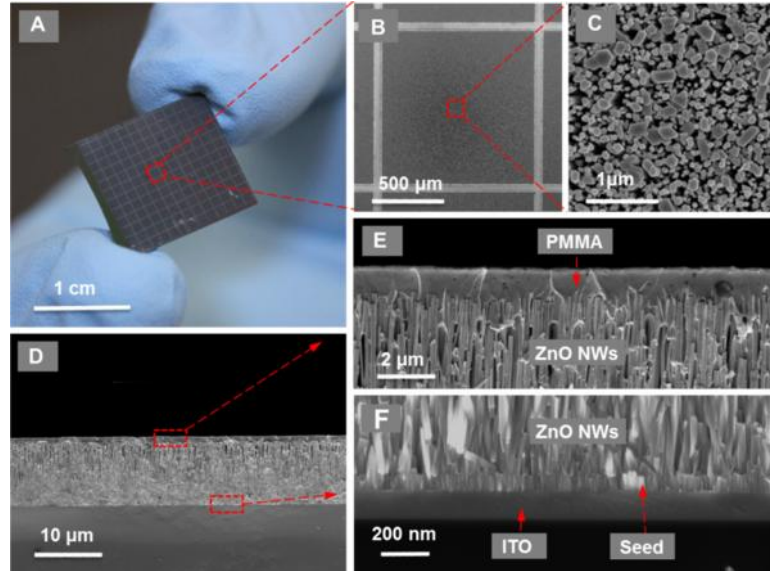


Figure 4.2 SEM images of the vertically integrated NG that show its structure. (A) Picture of the nanogenerator after position-controlled growth of ZnO NWs. (B) SEM image of one segment of the nanogenerator that is well defined by photolithography. (C) SEM image of the synthesized ZnO NWs with a top view. (D) SEM image of the device structure after spin-coating a PMMA on the grown NWs with a cross-sectional view. (E) SEM that shows coverage of NWs by the PMMA layer. (F) SEM image of the seed layer and the ITO layer between NWs and the substrate.

4.3 Electric measurement results and discussion

The as-fabricated nanogenerator was mechanically triggered by a linear motor that provided dynamic impact with controlled force, speed, and frequency. A commercial bridge rectifier was connected to the NG to convert the ac output into dc. For a NG with an effective dimension of 1 cm by 1 cm by 10 μm occupied by ZnO NWs, the open-circuit voltage (V_{oc}) and the short-circuit current (I_{sc}) reached up to 37 V (Figure 4.3A) and 12 μA (Figure 4.3B) under a stress of 1 MPa, respectively.

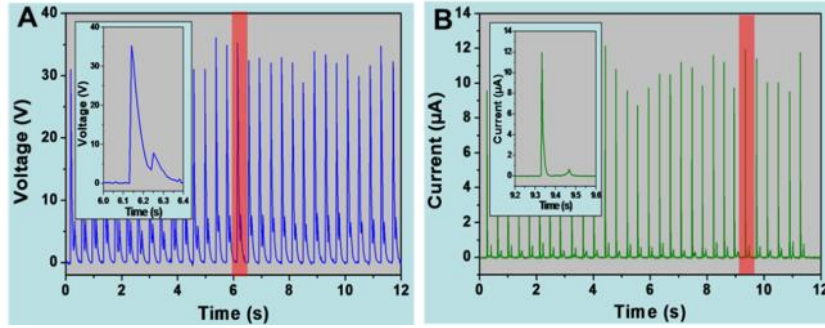


Figure 4.3 Electric measurement results of the vertically integrated NGs. (A) Open-circuit voltage of the nanogenerator rectified by a bridge rectifier under a stress of 1 MPa and an enlarged view of one cycle in the shadowed region (inset). (B) Short-circuit current of the nanogenerator rectified by a bridge rectifier under a stress of 1×10^6 Pa and an enlarged view of one cycle in the shadowed region (inset).

The working mechanism of the NG can be described by the transient flow of inductive charges driven by the piezopotential. When the NG is subject to a compressive stress, a piezopotential field is created along the NWs. As a result of electrostatic force, inductive charges are established on the top and bottom electrodes, which are the flowing charges through an external load. In other words, the strained NWs are analogous to polarized dipole moments in a plate capacitor filled by a dielectric material. Once the stress is released, the disappearance of the piezopotential leads to back flow of the inductive charges through the load^{73,74}. The COMSOL package was used to carry out theoretical calculations of the piezopotential^{73,74,79}. The calculated results predict an inductive potential difference of 45 V across the two electrodes at an applied stress of 1 MPa, as illustrated in Figure 4.4. Reduced magnitude of the experimental result in comparison to the simulated value is probably due to the screening effect of the free carriers within the NWs⁸⁰.

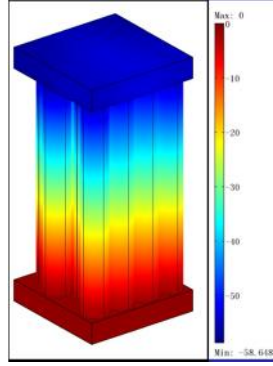


Figure 4.4 Finite element calculation of the potential distribution across the nanogenerator under a stress of 1 MPa

The superior performance and robustness of the newly designed NG are primarily attributed to the PMMA layer between the NWs and the metal electrode. Such a thin layer offers a number of advantages. First of all, it is an insulating layer that provides a potential barrier of infinite height, preventing the induced electrons in the electrodes from internal “leaking” through the ZnO/metal interface^{72,74,81}. It replaces the Schottky contact in early designs. Furthermore, the PMMA fills the gap between NWs by capillary force and forms a capping at the very top. Consequently, when a force is applied along the vertical direction, the stress can be transmitted through the capping layer to all NWs under the force-applied area, greatly enhancing the NG’s efficiency. This is a great improvement over some previous designs in which only a portion of NWs with proper length were in contact^{13,23,82}. Furthermore, it serves as a buffer layer protecting NWs from intimate interaction with the electrode, improving the NG’s robustness⁸³. It is also noteworthy that NWs were selectively grown in photolithography-designated regions. Such segmentation is designed to optimize the NG’s output. Though thermal annealing during the fabrication might help reducing the concentration of free charge carriers^{84,85}, there is still finite conductivity within ZnO NWs⁸⁰. As a result, free charge carriers within the NWs will partially screen the piezopotential, leading to reduced magnitude of it and

thus degraded performance of the NG. Shown by the cross-sectional image of the device in Figure 4.5, the NWs are so densely packed that they are all electrically connected in parallel. On condition that a force is applied on an area smaller than the device's dimension or the applied force has a nonuniform distribution, only the NWs located directly beneath the force-applied area will experience strain and thus generate piezopotential (Figure 4.5), which are referred to as active NWs. Owing to the presence of segmentation, native free charge carriers within the NWs that are not directly compressed under the force-applied area (referred to as inactive NWs) are isolated from the active NWs. Hence, they will not be involved in screening (left side of Figure 4.5), preserving the piezopotential from further degradation. However, if no segmentation is made among the NWs, the free carriers in the inactive NWs tend to drift toward the high piezopotential side of the active NWs (right side of Figure 4.5), which lower the local piezopotential and thus the output.

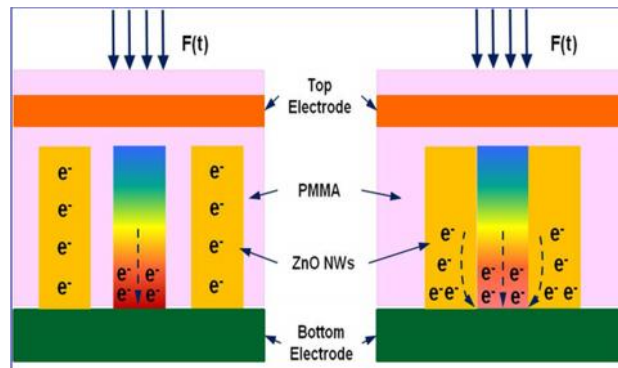


Figure 4.5 Analysis of the merit of the segmented design. The left-hand side schematic illustrates the case with segmentation, while the right-hand side one shows the case without segmentation (see text).

The electric output can be tremendously scaled up by linear superposition. An energy-harvesting pad was fabricated with nine NGs in parallel connection. Being punched by a human palm, the peak value of V_{oc} and I_{sc} exceeded 58 V and 134 μA , respectively (Figures 4.6 A B). Using such a significant output, we were able to charge a

capacitor of 2 μF to over 3 V with less than 20 times of palm impact (Figure 4.6 C).
20,24

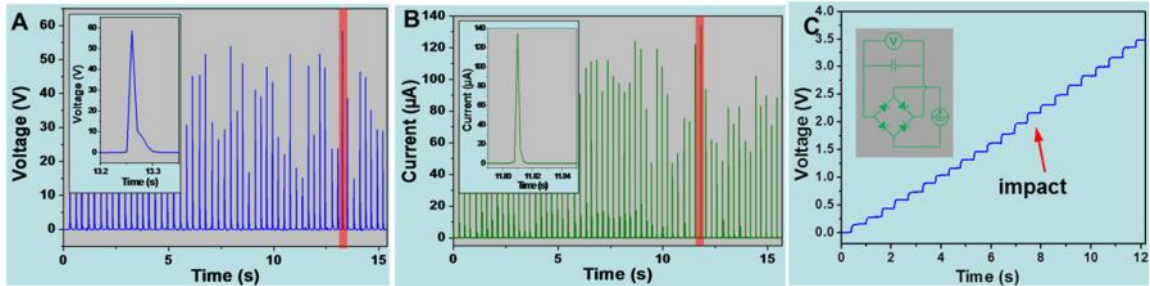


Figure 4.6 Electric measurement results of a NG pad that consists of 9 vertically integrated NGs in parallel connection. (A) Open-circuit voltage of the NG pad rectified by a bridge rectifier under impact by a human palm and an enlarged view of one cycle in the shadowed region (inset). (B) Short-circuit current of the NG pad rectified by a bridge rectifier under impact by a human palm and an enlarged view of one cycle in the shadowed region (inset). (C) Circuit diagram (inset) and voltage across a capacitor of 2 μF when being charged by the NG pad with every step corresponding to an impact.

4.4 Summary

In summary, using NGs based on ZnO NWs, the electric output from the NG reached a record high of 58 V and 134 μA , with a maximum power density of 0.78 W/cm^3 , which is by far the highest output power ever achieved by piezoelectric NGs. We suggest that the nanogenerator might be applicable as a power source for neuroprosthetic devices, although considerable work will be necessary to realize such integration in the future. The as-fabricated nanogenerator was mechanically triggered by a linear motor that provided dynamic impact with controlled force, speed, and frequency. A commercial bridge rectifier was

CHAPTER 5

TRIBOELECTRIC NANOGENERATOR, CONCEPT AND THEORY

5.1 Introduction

By converting ambient energy into electricity, energy harvesting is capable of at least offsetting, or even replacing, the reliance of small portable electronics on traditional power supplies, such as batteries^{1,68}. Especially when long-term operation of a large number of electronic devices in dispersed locations is required, energy harvesting distinguishes itself from batteries and hardwire power owing to inherent advantages, such as outstanding longevity, little maintenance, minimal disposal and contamination. Despite of these benefits, superior performance, miniaturized size and competitive prices are still to be sought after in order for the energy harvesting technology becoming prevalent. Here we demonstrate a novel and simple generator with extremely low cost for efficiently harvesting mechanical energy that is typically present in the form of vibrations and random displacements/deformation. Owing to the coupling of contact charging and electrostatic induction^{86,87}, electric generation was achieved with a cycled process of contact and separation between two polymer films. The instantaneous electric power density reached as high as 31.2 mW/cm³.

5.2 Structure and fabrication

Harvesting mechanical energy has been achieved by electromagnetic^{88,89}, piezoelectric^{9,90} and electrostatic^{91,92} mechanisms. However, widespread usage of these techniques is likely shadowed by possible limitations, such as structure complexity⁹³, fabrication of high-quality materials⁶⁸, and reliance on external power source⁹³. Here, our new type of generator can properly address all of these issues. Schemed in Figure 5.1, it has a multi-layer structure. Between two polymer layers, a cavity is formed, which is

sustained by a spacer, which is designed for the charge generation and separation processes.

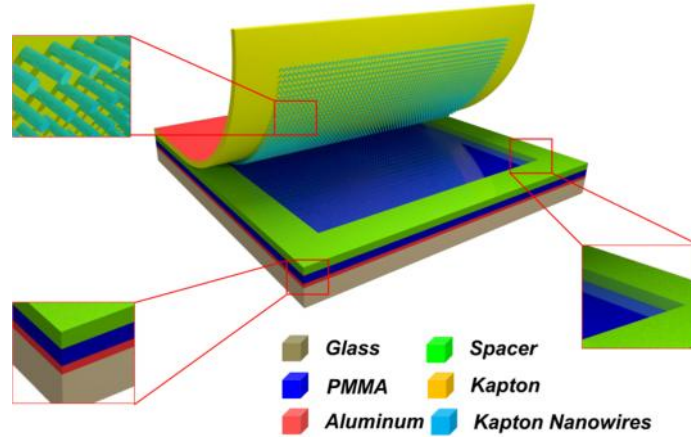


Figure 5.1 Sketch of the generator's structure and materials selection. The polymer nanowires (PNWs) are depicted with a different color from the substrate for clear visualization.

The fabrication process started with a square glass sheet, which was deposited with a thin layer of aluminum as the bottom electrode using electron beam evaporator. Then a thin layer of PMMA was spun-coated, followed by adding a spacer layer at the edges, leaving a square cavity at the center. One side of a Kapton film was deposited with a layer of aluminum as the top electrode, while the other side was dry-etched to create vertically aligned polymer nanowires (PNWs)⁹⁴. Then it was anchored on the spacer with the top electrode facing up. The spacer was made of insulating polymer with double-sided adhesive, keeping the Kapton film at a fixed distance away from the PMMA layer underneath.

5.3 Fundamental mechanism

5.3.1 Open-circuit voltage

The operating principle of the generator can be described by the coupling of contact charging and electrostatic induction. Respectively, Figure 5.2A and Figure 5.2B depict electric output of open-circuit voltage and short-circuit current. At original state, no charge is generated or inducted, with no electric potential difference (EPD) between the two electrodes (Figure 5.2 I). With an externally introduced displacement, the two polymers are brought into contact with each other. Surface charge transfer then takes place at the contact area due to triboelectric effect⁹⁵⁻⁹⁷. According to the triboelectric series⁹⁸ that is a list of materials based their tendency to gain or lose charges, electrons are injected from PMMA into Kapton, resulting in net negative charges at the Kapton surface and net positive charges at the PMMA surface, respectively. It is worth noting that the insulating property of the polymers allows a long-time retention of triboelectric charges for hours or even days⁹⁹. Since they are only confined on the surface^{100,101}, charges with opposite signs coincide at almost the same plane, generating practical no EPD between the two electrodes (Figure 5.2 II).

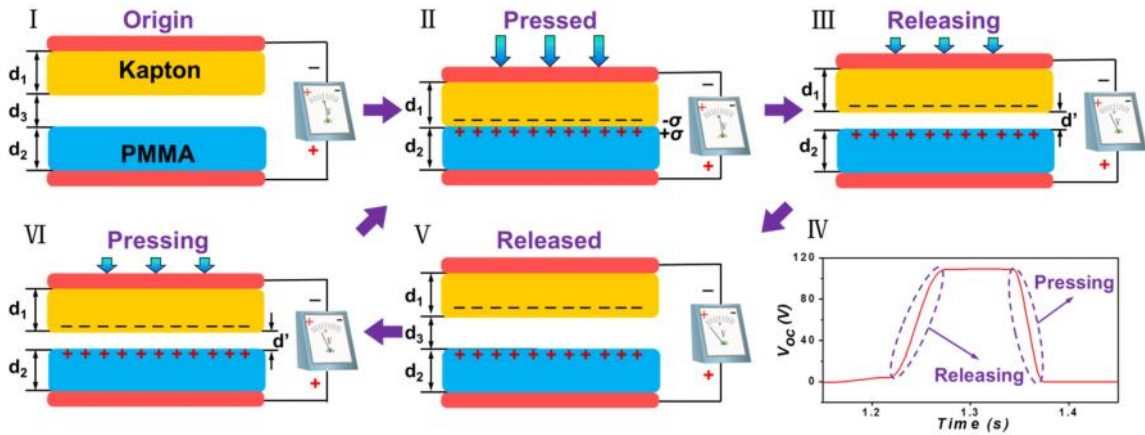


Figure 5.2 Sketch that illustrates the operating principle of the generator under open-circuit condition.

As the generator starts to be released, the Kapton film intends to revert back to its original position due to its own resilience. Once the two polymers separate, an EPD is

then established between the two electrodes (Figure 5.2 III). It is assumed that the two polymer layers are infinitely large planes because the lateral dimension is much greater than their thickness and the gap in between. Also, the Kapton film is simplified as a planar surface which retains its shape instead of having deformation when being pressed.

Once the two polymers separate, an electric potential difference (EPD) is then established between the two electrodes. Also we assume that relative permittivity of air is 1. If we define electric potential of the bottom electrode (U_{BE}) to be zero, electric potential of the top electrode (U_{TE}) can be calculated by

$$U_{TE} = \left(\frac{-\dagger |d_1}{2V_0 V_{rk}} - \frac{-\dagger |d'}{2V_0} - \frac{-\dagger |d_2}{2V_0 V_{rp}} \right) + \left(-\frac{\dagger d_1}{2V_0 V_{rk}} - \frac{\dagger d'}{2V_0} + \frac{\dagger d_2}{2V_0 V_{rp}} \right) \quad (5.1)$$

where \dagger is surface charge density, V_0 , V_{rk} , and V_{rp} are permittivity of vacuum, relative permittivity of the Kapton, and relative permittivity of the PMMA, respectively, d_1, d_2 and d' are thickness of the Kapton, thickness of the PMMA, and interlayer distance at a given state, respectively.

The terms within the first and the second parentheses represent contributions to U_{TE} from the negative triboelectric charges and the positive triboelectric charges, respectively. Upon simplification, U_{top} can be expressed as

$$U_{TE} = -\frac{\dagger d'}{V_0} \quad (5.2)$$

Then,

$$U_{TE} = -\frac{\dagger d'}{V_0} < 0 = U_{BE} \quad (5.3)$$

Therefore, as the generator starts to be released, V_{oc} keeps increasing until it reaches a maximum value when the Kapton film fully reverts to original position.

$$V_{\max} = -\frac{\dagger d_3}{V_0} \quad (5.4)$$

where d_3 is height of the spacer.

Here, we define a forward connection for measurement as a configuration with positive end of the electrometer connected to the bottom electrode (BE). All electric measurements in this work are based on the forward connection unless otherwise stated. Therefore, as the generator is being released, V_{oc} keeps increasing until reaching the maximum value when the Kapton film fully reverts to the original position (Figure 5.2 IV and Figure 5.2 V). Such a signal will remain constant provided that the input impedance of the electrometer is infinitely large.

If pressing is immediately followed, the EPD starts diminishing as the two polymer layers get closer to each other. As a result, V_{oc} drops from the maximum value to zero when a full contact is made again between the two polymers (Figure 5.2 V, VI).

5.3.2 Short-circuit current

If the two electrodes are shorted, any established EPD shown in Equation (1) as the two polymers separate drives electrons from the top electrode (TE) to the BE (Figure 5.3 III), resulting in an instantaneous positive current during the releasing process (Figure 5.3 IV). The net effect is that inducted charges accumulate with positive sign on the TE and negative sign on the BE (Figure 5.3 V).

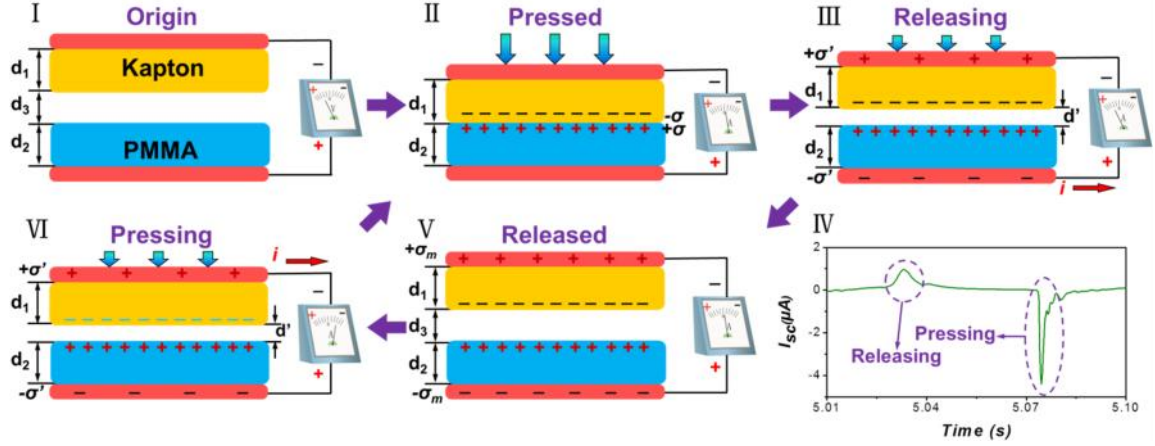


Figure 5.3 Sketch that illustrates the operating principle of the generator under short-circuit condition.

As the generator starts to be released, any EPD introduced from the triboelectric charges that are being separated will be instantly balanced by creation of more induced charges. Therefore, it is reasonable to assume that the generator stays at an equilibrium state at any moment. Therefore, the induced charge density (σ') can be calculated as follows.

$$\begin{aligned}
 U_{TE} &= \left(\frac{-\sigma' d_1}{2V_0 V_{rk}} - \frac{-\sigma' d'}{2V_0} - \frac{-\sigma' d_2}{2V_0 V_{rp}} \right) + \left(-\frac{\sigma' d_1}{2V_0 V_{rk}} - \frac{\sigma' d'}{2V_0} + \frac{\sigma' d_2}{2V_0 V_{rp}} \right) + \\
 &\left(\frac{-\sigma' d_1}{2V_0 V_{rk}} + \frac{-\sigma' d'}{2V_0} + \frac{-\sigma' d_2}{2V_0 V_{rp}} \right) + \left(\frac{\sigma' d_1}{2V_0 V_{rk}} + \frac{\sigma' d'}{2V_0} + \frac{\sigma' d_2}{2V_0 V_{rp}} \right) = 0 = U_{BE}
 \end{aligned} \tag{5.5}$$

The terms within the third and the fourth parentheses represent contributions to UTE from negative induced charges on the BE and positive induced charges on the TE, respectively. After simplification,

$$U_{TE} = -\sigma' d' + \sigma' \left(\frac{d_1}{V_{rk}} + d' + \frac{d_2}{V_{rp}} \right) = 0 \tag{5.6}$$

Therefore,

$$\dagger' = \frac{\dagger d' V_{rk} V_{rp}}{d_1 V_{rp} + d' V_{rk} V_{rp} + d_2 V_{rk}} \quad (5.7)$$

When the generator is fully released, \dagger' reaches a maximum value at

$$\dagger_{\max} = \frac{\dagger d_3 V_{rk} V_{rp}}{d_1 V_{rp} + d_3 V_{rk} V_{rp} + d_2 V_{rk}} \quad (5.8)$$

Once the generator is pressed again, an incremental reduction of the interlayer distance (d) would make

$$\begin{aligned} U_{TE} &= \left[\frac{-\dagger |d_1|}{2V_0 V_{rk}} - \frac{-\dagger |(d_3 - \Delta d)|}{2V_0} - \frac{-\dagger |d_2|}{2V_0 V_{rp}} \right] + \left[-\frac{\dagger d_1}{2V_0 V_{rk}} - \frac{\dagger (d_3 - \Delta d)}{2V_0} + \frac{\dagger d_2}{2V_0 V_{rp}} \right] + \\ & \left[\frac{-\dagger' |d_1|}{2V_0 V_{rk}} + \frac{-\dagger' |(d_3 - \Delta d)|}{2V_0} + \frac{-\dagger' |d_2|}{2V_0 V_{rp}} \right] + \left[\frac{\dagger' d_1}{2V_0 V_{rk}} + \frac{-\dagger' |(d_3 - \Delta d)|}{2V_0} + \frac{\dagger' d_2}{2V_0 V_{rp}} \right] \\ &= \frac{\Delta d}{V_0} (\dagger - \dagger') \end{aligned} \quad (5.9)$$

Since $\dagger > \dagger'$, as stated in the Equation 7,

$$U_{TE} > 0 = U_{BE} \quad (5.10)$$

As a consequence, electrons are driven from the BE back to the TE, reducing the amount of deducted charges on the electrodes. When the two polymers are in contact, all deducted charges get neutralized. This process corresponds to an instantaneous negative Isc signal.

Once the generator is pressed again, reduction of the interlayer distance would make the TE possesses a higher electric potential than the BE. As a consequence, electrons are driven from the BE back to the TE, reducing the amount of inducted charges (Figure 5.3 VI). This process corresponds to an instantaneous negative current (Figure 5.3 V). When the two polymers are in contact again, all inducted charges are neutralized (Figure 5.3 II).

5.4 Electric measurement results and discussion

As triggered by a vibration source with controlled frequency and amplitude, the generator produced an open-circuit voltage (Figure 5.4A) and a short-circuit current (Figure 5.4B) as predicted in the above analytical model.

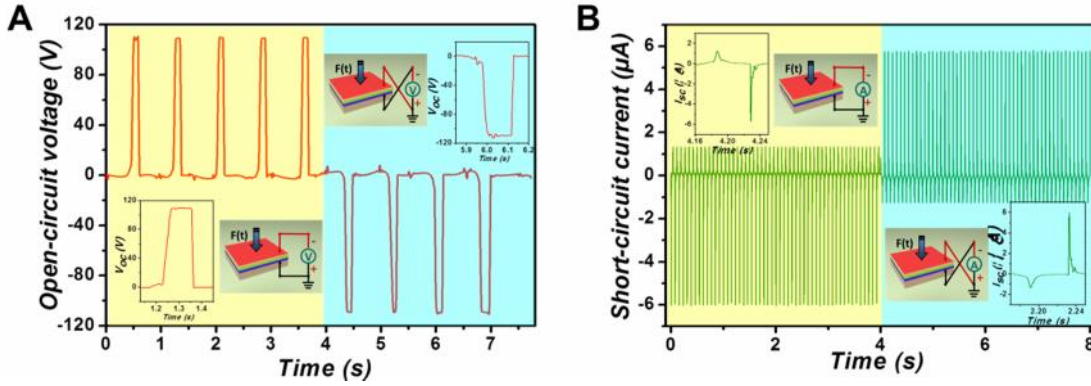


Figure 5.4 Electric measurement results of the triboelectric NG that works in contact mode. (A) Open-circuit voltage with forward connection on the left half (bottom-left insets) and reverse connection on the right half (upper-right insets). (B) Short-circuit current with forward connection on the left half (bottom-left insets) and reverse connection on the right half (upper-right insets).

Electric output with opposite sign was obtained by switching the polarity for electric measurement. The peak value of the V_{oc} and I_{sc} were up to 110 V and 6 μA , respectively. Substituting the experimentally determined V_{oc} into Equation 5.4, we obtained a theoretical triboelectric charge density:

$$\dagger = \frac{V_{oc} V_0}{d_3} = 97.39 \mu\text{C}/\text{m}^2 \quad (5.11)$$

Then based on Equation 5.8, the maximum inducted charge density (\dagger'_{\max}) was theoretically calculated to be:

$$\dagger'_{\max} = \frac{\dagger d_3 V_{rk} V_{rp}}{d_1 V_{rp} + d_3 V_{rk} V_{rp} + d_2 V_{rk}} = 73.72 \mu\text{C}/\text{m}^2 \quad (5.12)$$

Therefore, electrons are pumped back and forth between the two electrodes as a result of contact charging and electrostatic induction. For one cycle of contacting-sliding-separating the integration of current over time for releasing has the same value as that for pressing, indicating that equal amount of electrons flow in the opposite direction. It is observed that the current peak corresponding to releasing has a smaller magnitude but lasts longer than that for pressing (insets in Figure 5.4 B). Such an observation can be explained by the fact that pressing is caused by the external vibration source while it is the resilience of the Kapton film that leads to releasing. Therefore, it is very likely that releasing corresponds to a slower process and thus a smaller but wider current signal. Having the maximum inducted charge (Q'), the corresponding charge density was obtained as:

$$t'_{\max} = \frac{Q'}{S} = 87.23 \mu\text{C}/\text{m}^2 \quad (13)$$

where S is the electrode area that is the same as the device area.

The experimental result in Equation 5.13 is only slightly larger than the theoretically calculated one in Equation 5.12, indicating that the model is fairly valid for explaining the working principle. The difference is probably attributed to simplifications made in the model and errors that may occur in the measurement.

External load matching for the generator has also been investigated. With an increase in the load resistance, the maximum current decreases due to ohmic loss, while the maximum voltage across the load has an opposite trend (Figure 5.5 A). Accordingly, the electric power exhibits an instantaneous peak value of $110 \mu\text{W}$ (Figure 5.5 B), in correspondence to a power density of $31.2 \text{ mW}/\text{cm}^3$. The measurement results reveal that the generator is particularly efficient provided that the load has a resistance on the order of mega ohms.

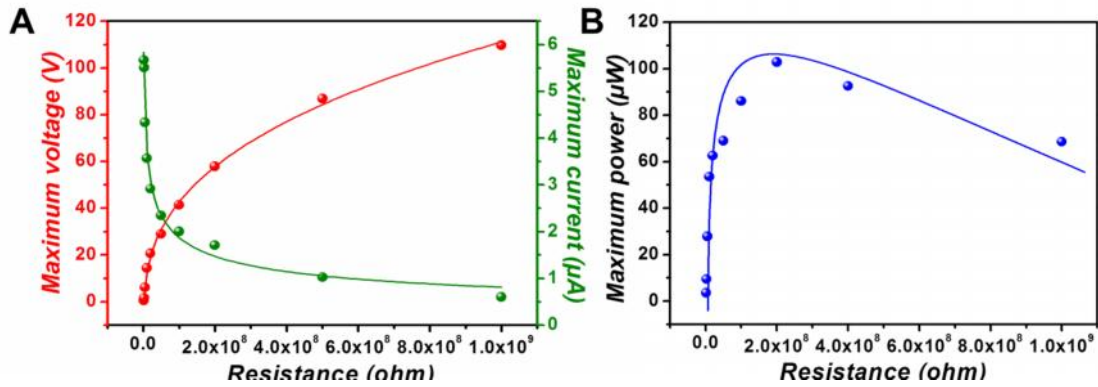


Figure 5.5 Dependence of the triboelectric NG's output power on external load resistance. (A) Electric voltage (left axis) and current (right axis) as a function of the load resistance. The dots are experimentally measured values, while the lines are fitted results. (B) Instantaneous electric power as a function of the load resistance. The dots are experimentally measured values, while the line is a fitted result.

Our demonstrated generator features simple fabrication/implementation, low cost, and strong performance. Previously reported electrostatic generators usually required precharging by external power source in order to introduce electrostatic force⁹¹. On the contrary, our generator is self-charged, with triboelectric charges instantly generated upon contact. Besides, the fabrication processing is highly straightforward with neither material synthesis nor micromachining. The selection of materials is cost-oriented. Extremely low cost for fabrication and materials is thus anticipated, which is likely to be further reduced for mass production.

The calculated triboelectric charge density shown in Equation 5.12 is substantially larger than previous reported^{96,97}. Moreover, the generator largely outperforms recent demonstrations based on electrostatic mechanism^{91,92}. Several factors may be attributed to this largely enhanced performance. The first one is appropriate selection of materials. Substantial polarity difference exists between Kapton and PMMA according to the triboelectric series, leading to very effective charge transfer upon contact. In addition, the spacer structure plays an important role. The spacer's height not only relates to V_{oc} , but

also affects I_{sc} . Without the spacer, only very little electric output could be detected. Furthermore, surface morphology modification is another key factor. Here, selective dry etching was applied on the Kapton surface to create vertically aligned polymer NWs, with longer etching corresponding to larger aspect ratio of the NWs. Enhanced surface roughness as a result of the NWs is expected to introduce additional friction as the two polymers are brought into contact. Such frictional movement is likely to generate more triboelectric charges⁹⁵; and thus enhanced electric output is achieved. However, experimental observation shows that the electric output substantially drops with excessive etching time (Figure 5.6 A). For NWs with proper length (hundreds of nanometers), the elastic property ensures retained orientation and morphology of the NWs even after numerous contacts. For overly long NWs, strain generated at the root is likely to exceed the elastic limit of the polymer material, resulting in permanent deformation (Figure 5.6 B). As a result, they are no longer able to introduce effective friction, which explains the less enhanced electric output.

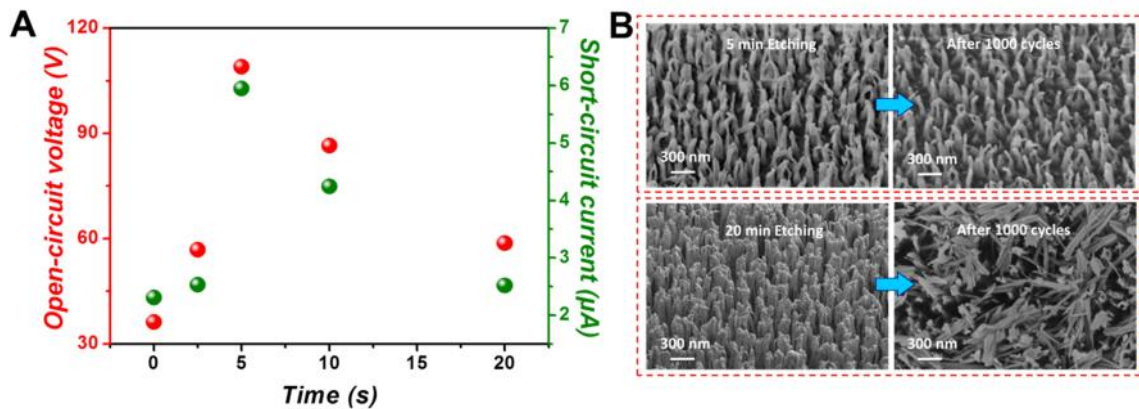


Figure 5.6 Dependence of the triboelectric NG's output power on surface modification. (A) The effect of time for etching polymer nanowires on open-circuit voltage (left axis) and short-circuit current (right axis). (B) SEM images of the PNWs before (left pairs) and after (right pairs) the generator operates for 1000 cycles to explain why PNWs with proper length (top pairs) contribute to much more enhanced electric output than do excessively long PNWs (bottom pairs).

In summary, we demonstrated a new type of self-charged generator for harvesting mechanical energy based on a coupled process of contact charging and electrostatic induction. The generator has the virtue of highly simple fabrication/implementation, strong performance and extremely low cost, which properly address limitations of energy-harvesting technology. The instantaneous electric power density was up to 31.2 mW/cm³. Our work not just only demonstrates a promising energy-harvesting technique but also greatly broadens the application of energy-harvesters.

CHAPTER 6

SCALABLE TRIBOELECTRIC NANOGENERATOR

6.1 Introduction

We are surrounded by enormous amounts of ambient mechanical energy that goes to waste such as rain drops, human footfalls, air flow, ocean waves, just to name a few. Research on mechanical energy harvesting falls into three established categories, i.e. electrostatic^{102,103}, piezoelectric^{9,65,90}, and electromagnetic⁸⁸⁻¹⁰⁴. It has been mainly focusing on small-scale energy harvesting, aiming at powering micro/nano-systems^{1,68,105} for applications including sensors^{93,106}, environmental monitoring¹⁰⁷, medical science^{108,109}, personal electronics^{110,111} and defense technology¹¹². With the advance in the technology developed for small-scale energy harvesting, it may be possible to scale up this type of technology at a large scope¹, such as ocean waves¹¹³ and wind power¹¹⁴. Such a potential needs to be explored with a consideration of the scalability of the technology, the cost of materials and fabrication process, environmental impact and practical feasibility for implementation.

Triboelectric effect is an old phenomenon and is usually undesirable because of potential hazards to electronics and public safety. However, it has recently been utilized as an extremely effective means to harvest mechanical energy by a new type of organic/polymer nanogenerators (NG)^{86,115}. Energy conversion is achieved by the coupling between triboelectric effect and electrostatic effect. Contact between two materials that differ in polarity of triboelectricity yields surface charge transfer. As they separate, a dipole moment is established, driving electrons through external loads. The NG acts as a charge-pump, in which current flows back and forth between the electrodes in AC characteristic. It provides an unprecedentedly simple and cost-effective means of harvesting ambient mechanical energy mainly using polymer based materials.

Here in this work, we developed a new triboelectric NG that has not only much simplified structure but also substantially higher power output enabled by nanoparticle-based surface modification. Short-circuit current reached a peak value of 2.0 mA, which corresponded to the instantaneous power output of 1.2 W and power density of 313 W/m². Average power output and energy conversion efficiency at device level were calculated to be 132.1 mW and 9.8 %, respectively. For the first time, we experimentally realized scaling up of the NG's power output, making it power not just a single electronic device but hundreds of them simultaneously. Triggered by commonly available mechanical source such as footfalls, the NG was capable of instantaneously lighting up 600 commercial LED bulbs in real time at an estimated output open circuit voltage of ~1200 V. This work unravels the practicability of harvesting mechanical energy by the NG on a large scale. The working mechanism demonstrated here can be further applied to potentially harvesting large-scale mechanical energy such as rolling wheels, wind power, and ocean waves.

6.2 Structure and fabrication

The NG has a layered structure with two substrates, as schemed in Figure 6.1. Polymethyl methacrylate (PMMA) was selected as the material for substrates due to its decent strength, light weight, easy processing, and low cost. On the lower side, a layer of contact electrode is prepared. The contact electrode plays dual roles of electrode and contact surface. It consists of a gold thin film and gold nanoparticles coated on the surface. Alternatively, nanoparticles of non-precious metals can also be used as replacements. Figure 1c shows uniform distribution of the nanoparticles on the surface. They modify the surface both physically and chemically, which will be discussed in detail later. On the other side, a thin film of gold is laminated between the substrate and a layer of polydimethylsiloxan (PDMS). This electrode is called back electrode for later

reference. The two substrates are connected by four springs installed at the corners, leaving a narrow spacing between the contact electrode and the PDMS. The as-fabricated NG is exhibited in Figure 1b. As sketched in Figure 1d, the fabrication flow is straightforward without sophisticated equipment and process.

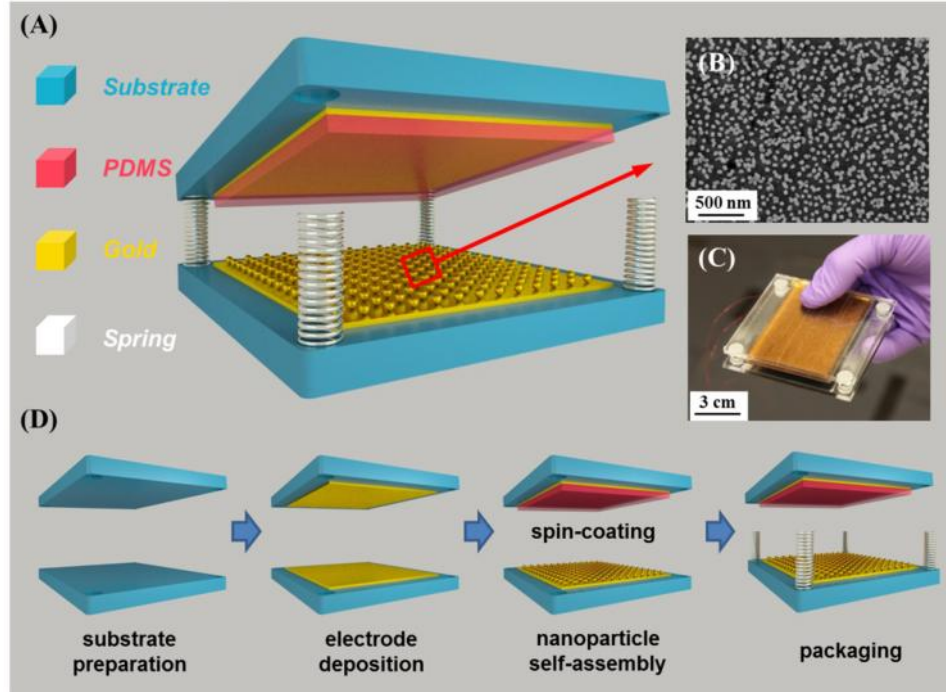


Figure 6.1 Structure and fabrication process of the scalable triboelectric NG. (A) Schematic and (B) photograph of a fabricated triboelectric NG. (C) SEM image of gold nanoparticles coated on gold surface. (D) Process flow for fabricating the NG.

To fabricate the NG, two pieces of cast acrylic glass were prepared as substrates with dimensions of 3 inch by 3 inch by 3/32 inch. Four half-thorough holes were drilled at corners as houses for spring installation. 50 nm of gold were deposited on both of the substrates by e-beam evaporator (2 inch by 3 inch). On one of the substrates, fluid PDMS that consists of base and curing agent in a ratio of 5:1 was spin-coated to form a 10 μm -thick layer. Then it was cured at 100 $^{\circ}\text{C}$ for 45 minutes. On the other substrate, gold nanoparticles were uniformly distributed on gold surface by self-assembly. Subsequently,

four springs (spring constant=7.3 lb/inch) were installed in the houses to connect the two substrates together, leaving a spacing of 1 mm between the gold and the PDMS. The spacing is required to be substantially larger than the polymer thickness to ensure effective generation of inductive charges³¹. Finally, conducting wires were connected to the two metal layers as leads for subsequent electric measurement.

Self-assembly of gold-nanoparticles is performed by the following method. A solution (50 mL) containing Sodium tetrachloroaurate dihydrate (1 mM) and hexadecyltrimethylammonium bromide (10 mM) was brought to a vigorous boil with stirring in a round-bottom flask fitted with a reflux condenser; Hydrazine hydrate solution (20 μ L) was then added rapidly to the solution. The solution was heated under reflux for another 8 min, during which time its color changed from pale yellow to pale red. The solution was cooled to room temperature while stirring continuously. The average size (56 nm) of the synthesized gold nanoparticles was verified through SEM analysis. Au films were derivatized by immersion in a solution of 1,4-benzenedithiol for 12 h and rinsed with methanol and then water. The derivatized Au films were then immersed in a solution of gold nanoparticles for 12 h to allow for complete adsorption of a single gold nanoparticle layer. Before the SEM characterization and electrical measurement, non-adsorbed gold nanoparticles were removed by rinsing with water.

6.3 Operation principle

The electric energy generation process can be explained by the coupling between triboelectric effect and electrostatic effect, as sketched in Figure 6.2.

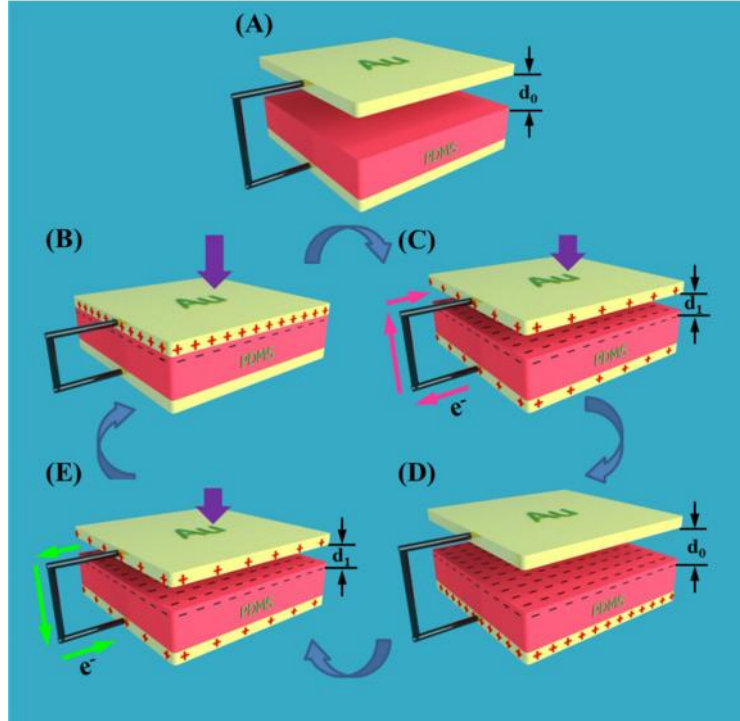


Figure 6.2 Operating principle of the scalable triboelectric NG. (A) Original position without mechanical force applied. (B) External force brings gold and PDMS into contact, generating positive triboelectric charges on the gold side and negative charges on the PDMS side. (C) Withdrawal of the force causes a separation. Potential difference drives electrons from the back electrode to the contact electrode, screening the triboelectric charges and leaving behind inductive charges. (D) Original position is recovered with all positive triboelectric charges screened on the contact electrode. (E) Electrons are driven back to the back electrode as the force is reapplied, screening the inductive charges. Note: For simplification, nanoparticles and springs are not shown in the schematics.

At original position, a separation distance is maintained by springs, as indicated by d_0 in Figure 6.2 A. When an external impact is applied on one of the substrates, gold and PDMS are brought into contact. According to the triboelectric series that ranks materials' tendency to gain or lose electrons, electrons are injected from gold into PDMS⁹⁵⁻⁹⁷ resulting in surface triboelectric charges (Figure 6.2 B)^{100,101}, which are retained on the PDMS. As the impact is withdrawn, the contacting surfaces move apart

due to restoring force from the springs. Once a separation forms, the back electrode possess a lower electric potential than the contact electrode, producing an electric potential difference. Such a potential difference drives electrons through external loads and screens the positive triboelectric charges on the contact electrode (Figure 6.2 C). When the NG reverts back to the original position, positive triboelectric charges on the contact electrode are completely screened, leaving equal amount of inductive charges on the back electrode (Figure 6.2 D). Subsequently, mechanical impact once again shortens the separation, producing an electric potential difference with reversed polarity. In consequence, electrons flow in a reversed direction (Figure 6.2 E). They keep screening inductive charges on the back electrode until a direct contact is again established (Figure 6.2 B). It is to be noted that the insulating PDMS allows long-time retention of the triboelectric charges on its surface⁹⁹ even though the triboelectric charges on the metal side are periodically screened by inductive charges. In this process, the NG acts as an electron pump that drives electrons back and forth between the two electrodes.²¹

6.4 Electric measurement results and discussion

To trigger the NG, a mechanical shaker was used to apply impulse impact. Here, the interaction force generated between the gold and the PDMS is defined as contacting force, which was monitored by a force sensor. Open-circuit voltage (V_{oc}) and short-circuit current (I_{sc}) were measured to characterize the NG's electric performance. With a contacting force of 10 N, the V_{oc} and the I_{sc} were presented in Figure 6.3 A and Figure 6.3 B, respectively. The V_{oc} switched between zero and a plateau value, respectively corresponding to the contact position and the original position. The I_{sc} exhibits AC behavior, with equal amount of electrons flowing in opposite directions within one cycle. The experimental data validate the working principle described in Figure 6.2. It is observed that the current signal for separation has a smaller magnitude but longer

duration than that for contact. It can be explained by faster contact resulting from external impact compared to slower separation caused by restoring force of the springs. The polarity of the measured electric signals can be reversed upon switching the connection polarity between the NG and the measurement instrument. Furthermore, the AC output could be transferred to pulse output in the same direction simply by a full-wave rectifying bridge (Figure 6.3 C).

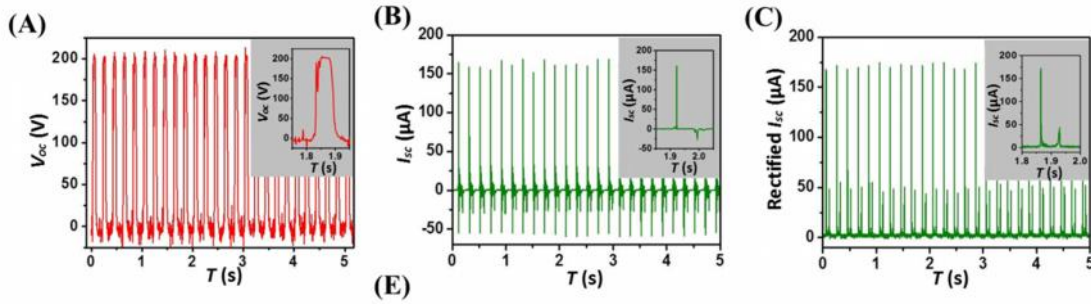


Figure 6.3 Electric measurement results of the scalable triboelectric NG. (A) Open-circuit voltage (V_{oc}) at contacting force of 10 N. Inset: enlarged view of one cycle. Contact causes rising of the V_{oc} to a plateau value and separation make it fall back to zero. (B) Short-circuit current (I_{sc}) at contacting force of 10 N. Inset: enlarged view of one cycle. Contact and separation correspond to a positive current pulse and a negative current pulse, respectively. (C) Rectified short-circuit current (I_{sc}) by a full-wave bridge at contacting force of 10 N. Inset: enlarged view of one cycle, showing two current pulses in the same direction.

The NG's electric output is strongly related to the contacting force, yielding higher output with larger force. At a force as small as 10 N, the NG can still produce I_{sc} ranging from 160 μA to 175 μA (Figure 6.4). When the force increases to 500 N, the electric output reaches a saturated value, producing a peak I_{sc} of 1.2 mA. This result is due to increased contact area with larger force. The two contacting surfaces are neither absolutely flat nor smooth. Surface roughness is caused by inherent curvature of the substrates, nanoparticle modification, and fabrication defects such as particle

contamination from the air. At small contacting force, the surface roughness prevents fully intimate contact between the contact electrode and the PDMS, leaving some areas untouched. With larger force, due to elastic property, the PDMS can deform and fill more vacant space, thus leading to larger contact area. As a result, the electric output increases until all the vacant spacing is completely filled by the PDMS, reaching a saturated limit.

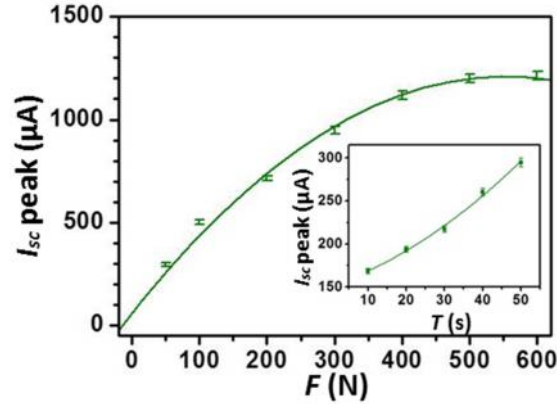


Figure 6.4 Dependence of the I_{sc} on the contacting force. Larger contacting force corresponds to higher current until saturation occurs. Inset: I_{sc} at contacting force less than 50 N. The data points represent peak value of current pulses while the line is fitted result.

Resistors were connected as external loads to further investigate the effective electric power of the NG. As demonstrated in Figure 6.5 A, the instantaneous current drops with increasing load resistance due to Ohmic loss, while the voltage builds up. Consequently, the instantaneous power output reached the maximum at a load resistance of $1 \text{ M}\Omega$. At a contacting force of 500 N, a power output of 0.42 W was achieved (Figure 6.5 B), corresponding to a power density of 109 W/m^2 for one layer of NG. This value is substantially larger than previously demonstrated ones by triboelectric nanogenerators. If the mechanical shaker was replaced by human footfalls which can generate a contacting force between 500 N to 600 N, the maximum I_{sc} could reach up to 2 mA, as demonstrated in Figure 6.5 C. It corresponded to an instantaneous current of 1.1 mA at a load of $1 \text{ M}\Omega$,

instantaneous output power of 1.2 W, and power density of 313 W/m². The power density can be further multiplied by stacking layers of the NGs in vertical direction. Integrating the largest I_{sc} signal (inset of Figure 6.5 C) with time gives the maximum inductive charges of 2.3 μC that flow between the two electrodes, giving a maximum triboelectric charge density of 594.2 μC/m². Compared to previous works, the surface charge density represents an increase of at least 8 times.²¹ The apparent deviation shown in Figure 6.5 C is probably caused by impact from footfall which lacks control on position, force, and direction. However, it is noted that the mean value is comparable to that obtained with the mechanical shaker (1.2 mA in Figure 6.4).

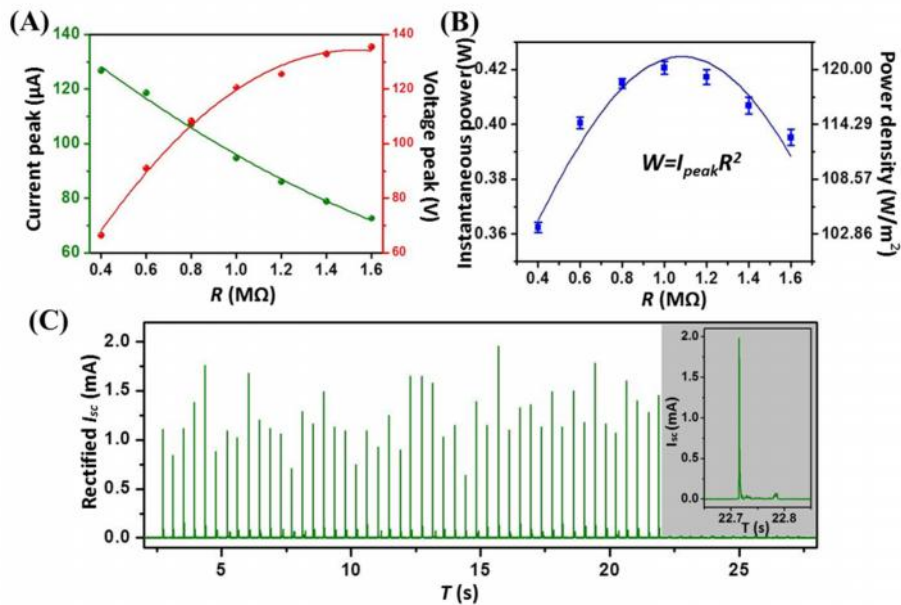


Figure 6.5 Dependence of the scalable triboelectric NG on external resistance. (A) Dependence of the current output on external load resistance at contacting force of 10 N. Increased load resistance results in lower current output but higher voltage output. The points represent peak value of electric signals while the line is fitted result. (B) Dependence of the power output on external load resistance at contacting force of 500 N, indicating maximum power output when $R=0.8 \text{ M}\Omega$. The curve is a fitted line. (C) Short-circuit current (I_{sc}) when triggered by human footfall that can generate contacting force between 500 N to 600 N. Inset: enlarged view of the highest current pulse.

As an important figure of merit, energy conversion efficiency of the NG was calculated. The conversion efficiency is defined as the ratio between the electric energy that is delivered the load by the NG and the mechanical energy the NG possesses. Figure 4a is a current pulse output produced by human footfall at load resistance of 1 M Ω . The time span between t_1 and t_2 represents a single contact. With an external load of pure resistance, the electric energy delivered by the NG is equal to the Joule heating energy, which is presented below.

$$E_{electric} = Q = \int_{t_1}^{t_2} I^2 \cdot R \cdot dt = R \cdot \int_{t_1}^{t_2} I^2 \cdot dt = 1 \times 10^6 (\Omega) \cdot \int_{22.7144}^{22.7200} I^2 \cdot dt = 0.74 \text{ mJ}$$

where Q is the Joule heating energy, I is the instantaneous current, and R is the load resistance. Consequently, the average power output ($W_{average}$) can be obtained by

$$W_{average} = \frac{E_{electric}}{t_2 - t_1} = \frac{0.74 \text{ mJ}}{(22.7200 - 22.7144) \text{ s}} = 132.14 \text{ mW}$$

As soon as the mechanical energy is introduced, it presents in two forms, i.e. elastic energy stored in the springs and kinetic energy carried by a moveable substrate of the NG. The elastic energy is later released without converting into electric energy, which is calculated by

$$E_{elastic} = \frac{1}{2} \cdot k \cdot x^2 \cdot N = 2.56 \text{ mJ}$$

where k is the spring constant ($k = 1278.88 \text{ N/m}$), x is the displacement of a spring that is equal to the spacing between the two contacting surfaces ($x = 1 \text{ mm}$), and N is the number of springs ($N = 4$).

For kinetic energy, at the moment when the two substrates make a contact, it completely transforms to other forms, including electric energy and thermal energy. It can be calculated by the following equation.

$$E_{kinetic} = \frac{1}{2} \cdot m \cdot v^2 = 4.97 \text{ mJ}$$

where m is the mass of the moveable substrate ($m = 13.45$ g, the mass of gold thin film and PDMS layer are negligible), and the v is the velocity of the substrate when a contact is just about to be made ($v = 0.86$ m/s).

Therefore, the energy conversion efficiency (η) is calculated as

$$\eta = \frac{E_{electric}}{E_{mechanical}} \times 100\% = \frac{E_{electric}}{E_{elastic} + E_{kinetic}} \times 100\% = \frac{0.74 \text{ mJ}}{2.56 \text{ mJ} + 4.97 \text{ mJ}} = 9.8 \%$$

It is to be noted that the above result is the overall efficiency at device level. However, at conversion process level, the elastic energy stored in the springs does not participate in energy conversion. Therefore if we solely take into account the kinetic energy that actually partially converts to electric energy, the direct efficiency at conversion process level is

$$\eta_{direct} = \frac{E_{electric}}{E_{kinetic}} \times 100\% = \frac{0.74 \text{ mJ}}{4.97 \text{ mJ}} \times 100\% = 14.9 \%$$

The unprecedentedly high power output of the NG is mainly attributed to three reasons. Firstly, the contact electrode plays dual roles of electrode and contacting surface. Compared to previously reported designs in which both of the contacting surfaces are made of polymers, more inductive charges will be generated for the new design. Secondly, the elastic property of PDMS enables conformal contact despite of surface roughness. The PDMS can easily deform in response to small pressure and fill the otherwise vacant space that result from substrate curvature and fabrication defects. The tolerance on surface roughness ensures as much contact area as it can be possibly obtained. Last but not the least, the surface modification by gold nanoparticles plays an important role for the output enhancement. It can offer five-fold increase on the current output compared to the device without modification, which in turn gives power enhancement of 25 times. Physically, the bumpy surface of the nanoparticle provides a larger contact area than a flat surface does. Chemically, the as-synthesized gold nanoparticles are positively charged in nature¹¹⁶. We suggest that the already carried positive charges can add up with triboelectric charges upon contact, leading to a largely

enhanced surface charge density and thus a substantially higher electric output. Follow-up study is being conducted to systematically investigate the mechanism for the nanoparticle-enabled enhancement. Therefore, optimized structure, proper selection of materials, and functional surface modification are the three key factors that contribute to the record high power output. If we take the whole size of the NG into consideration, volume power density of as high as 54268 W/m^3 can be expected. This value reveals an extremely attractive perspective for applying the NG on large-scale.

6.5 Summary

In summary, we invented a new type of triboelectric NG that delivered an unprecedentedly high power output. Simplified structure and nanoparticle-enabled surface modification are key factors that enabled this gigantic enhancement. Maximum short-circuit current of 2.0 mA was obtained. That gives instantaneous power output of 1.2 W, power density of 313 W/m^2 , average power output of 132.1 mW, open-circuit voltage of $\sim 1200 \text{ V}$, and energy conversion efficiency of 9.8% at device level. It unravels large-scale applications of the NG and broadens our horizons on the capability of the NG. With such a high power output, we vision energy harvesting by the triboelectric NG not only from human footfall but also from rolling wheels, wind power, and ocean waves.

CHAPTER 7

SLIDING MODE OF TRIBOELECTRIC NANOGENERATOR

7.1 Introduction

The triboelectric effect is a type of charge transfer by which two materials, after contacting with each other, become electrically charged in opposite signs¹¹⁷⁻¹¹⁹. Most daily static electricity can be explained by the triboelectric effect. Though the fundamental mechanism of this effect is still under investigation¹²⁰⁻¹²⁶, it has been utilized in applications including electrostatic separations¹²⁷, photocopying¹²⁸, laser printing¹²⁹, self-assembly¹³⁰⁻¹³⁷, and chemical systems¹³⁸⁻¹⁴¹. Recently, this effect has been innovatively applied in energy harvesting to fabricate triboelectric generators (TEGs) that convert small-scale mechanical energy into electricity^{86,87,115}. The TEG offers a new paradigm for simple, extremely low-cost, and scalable green energy technology. However, the previously demonstrated TEGs require periodic contact and separation of two materials that have opposite triboelectric polarities, making it only applicable to harvest energy from intermittent impact or shock. More critically, an indispensable design of the TEG is a cavity with constantly changing volume, which makes the TEG difficult for device packaging and largely limits its applications in atmospheres with high humidity, corrosive chemicals or gases, and in water or other liquids.

In this work, we present a new principle of TEG that is based on sliding electrification between two surfaces, which overcomes the limitations of previous TEGs and greatly expands the applicability of the TEG for diverse forms of mechanical motions. Owing to the coupling between triboelectric effect and electrostatic effect, inductive electrons form alternating current between electrodes as reciprocating sliding friction

occurs. With linear grating introduced to the sliding surfaces, substantial enhancements of output charge, output current and current frequency are achieved. At a sliding velocity of 10 m/s, a TEG (6.4 cm by 3.8 cm) with 10 grating units is equivalent to a continuous current source of 0.44 mA (corresponding current density of 0.18 A/m²) at an open-circuit voltage of 615 V. The electric output is expected to be further greatly scaled up with finer grating. The principle demonstrated in this work can be further applied to configurations other than planar surfaces, such as cylinders, tubes and rotational discs, harvesting mechanical energy not just from translational motion but also from rotational/rolling motion. Therefore, this work establishes the fundamentals of a versatile solution to harvest diverse forms of mechanical energy, including rolling wheels, wind power, and water flow, provided that robust engineering design and packaging technology are available. The principle can also be used to design self-powered motion sensors for detecting translation or rotation.

7.2 Non-grating design

7.2.1 Structure and fabrication

The basic structure of the TEG is sketched in Fig. 1a. It has a structure in which two contacting surfaces that can slide smoothly with one against the other. Acrylic was selected as a substrate material due to its decent strength, light weight and good machinability. On one substrate, aluminum thin film plays dual roles of an electrode and a sliding surface. On the other substrate, copper electrode is sandwiched between the substrate and a PTFE film. Two acrylic substrates with a size of 6.4 cm by 3.8 cm by 0.16 cm were prepared by laser cutter. On one of the substrate, aluminum layer with a

thickness of 100 nm was deposited by e-beam evaporator. On an PTFE film with a thickness of 100 μm , a copper electrode was prepared by depositing 100 nm of copper. Then, the copper-coated PTFE was adhered to the other substrate with the un-coated surface on the top. Finally, the two substrates were brought together with the aluminum contacting the un-coated PTFE. Lead wires were connected to the two metal electrodes for measurement.

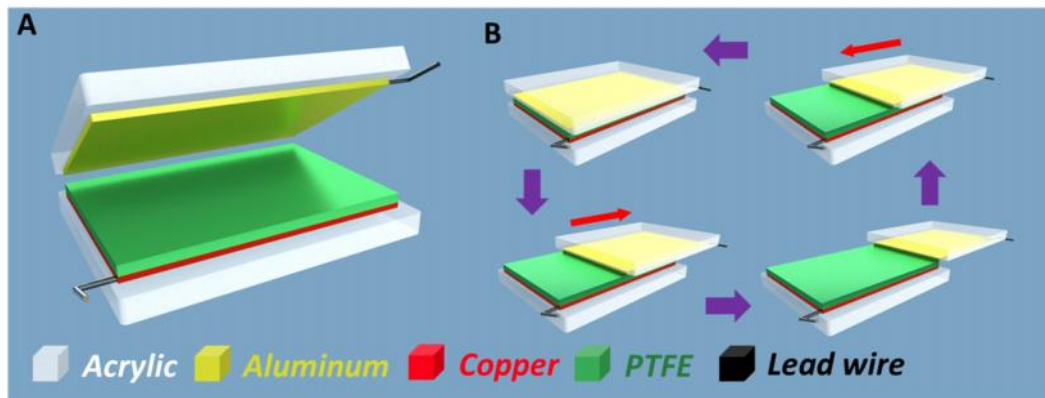


Figure 7.1 Structure of the triboelectric NG on sliding mode. (A) Schematic of a TEG without grating. The upper substrate is tilted to clearly demonstrate the structure. (B) A complete sliding cycle of the TEG at different percentage of plate mismatching areas.

At original position, the two sliding surfaces are fully aligned, with one sitting freely on the other. Driven by a tangential force applied to a substrate, relative displacement in contact mode occurs in lateral direction. After the two surfaces are fully displaced, the reciprocating force retraces them back to the aligned position (Figure 7.1 B).

7.2.2 Fundamental mechanism

Open-circuit voltage

The principle of the TEG is explained by the coupling between triboelectric effect and electrostatic effect. Once the PTFE film is brought into contact with the aluminum thin film, surface charge transfer takes place due to the triboelectric effect or contact electrification. Since PTFE is much more triboelectrically negative than aluminum, electrons are injected from aluminum into PTFE. At aligned position, though triboelectric charges present on the surfaces, positive ones on aluminum are fully compensated by the negative ones on PTFE, producing no electric field in surrounding space if the electric field at the edge is ignored (Figure 7.2 A).

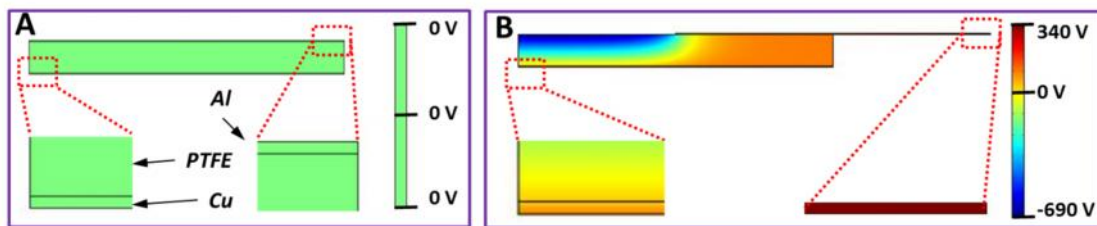


Figure 7.2 Simulation results that show the operating principle of the sliding triboelectric NG. (A) COMSOL simulation result of electric potential distribution when the two surfaces are fully aligned without any displacement caused by sliding. (B) COMSOL simulation result of electric potential distribution when the two surfaces are halfway displaced.

Once a relative displacement is introduced by an externally applied force in the direction parallel to the surfaces, triboelectric charges are not compensated at the displaced/mismatched areas, resulting in the creation of an effective dipole polarization parallel to the direction of the displacement. Therefore, the uncompensated charges generate electric potential difference (EDP) across the two electrodes, as illustrated by a simulation plot *via* COMSOL in Figure 7.2 B.

For simplicity of the mathematical derivation, the analytical model is built based on the following assumptions: (1) The two sliding surfaces of the TEG are infinitely large because the lateral dimension is much larger than the vertical thickness; (2) The generated triboelectric charges, which are non-mobile and non-annihilative, are uniformly distributed on the two surfaces. This is an excellent approximation if the two materials are insulative. In a case that one side is metal, this approximation is made for easy derivation; (3) Both the aluminum and the PTFE thin film can be simplified as planar surfaces which retain their shapes instead of having deformation when sliding laterally.

Once the two surfaces contact with each other, triboelectric charges are created due to contact electrification. Based on assumption (2) and assumption (3), the lateral displacement l brings about uncompensated positive and negative triboelectric charges in the displaced areas on the upper surface and the lower surface, respectively (Figure 7.3).

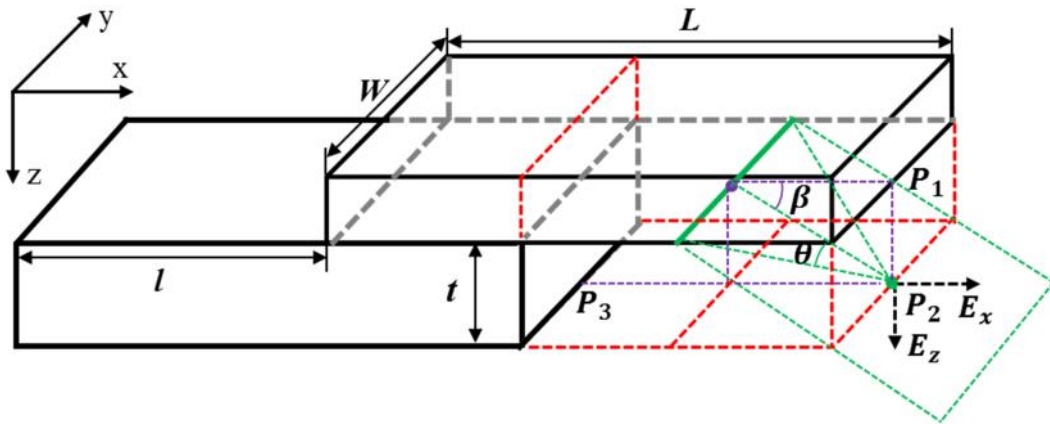


Figure 7.3 A schematic to illustrate the calculation of open-circuit voltage V_{oc} and the definition of the parameters.

If we define the electric potential of the copper electrode (U_{Cu}) to be zero, the open circuit voltage of the TEG is equal to the electric potential of the electrode electrode (U_{Al}), that is,

$$V_{oc} = U_{Al} - U_{Cu} = U_{Al} = U_{P_1} - U_{P_3} \quad (7.1)$$

Also, the electric potential difference can be expressed as

$$U_{P_1} - U_{P_3} = \int_{P_1}^{P_3} \mathbf{E} \cdot d\boldsymbol{\ell}_{1 \rightarrow 3} = \int_{P_1}^{P_2} \mathbf{E}_{1 \rightarrow 2} \cdot d\boldsymbol{\ell} + \int_{P_2}^{P_3} \mathbf{E}_{2 \rightarrow 3} \cdot d\boldsymbol{\ell} \quad (7.2)$$

Meanwhile, given assumption (1) and (2), we can consider the upper surface as charged plate of infinity in size, so that the electric lines of force are perpendicular to the surface of the plate as well as the patch from P2 to P3. As a result

$$\int_{P_2}^{P_3} \mathbf{E}_{2 \rightarrow 3} \cdot d\boldsymbol{\ell} = 0 \quad (7.3)$$

and
$$U_{Al} = \int_{P_1}^{P_2} \mathbf{E}_{1 \rightarrow 2} \cdot d\boldsymbol{\ell} \quad (7.4)$$

In order to calculate the electric field strength $E_{1 \rightarrow 2}$ in the path from P_1 to P_2 , let us consider an infinite, charged line in the displaced area on the upper surface, as indicated by the solid green line in Fig. S1. And the corresponding electric field strength E_{sl} at P_2 can be quantitatively expressed as

$$E_{sl} = \int_{-\theta}^{+\theta} \frac{\sigma}{4\pi\epsilon_0} \cdot \frac{\cos\theta}{\sqrt{t^2+l^2}} \cdot d\theta = \frac{\sigma}{2\pi\epsilon_0} \cdot \frac{\sin\theta}{\sqrt{t^2+l^2}} \quad (7.5)$$

where ϵ_0 is the permittivity of vacuum, t is the thickness of the PTFE film, l is the displacement, and σ is the line charge density

$$\sigma = \frac{q}{Wl} \quad (7.6)$$

where q is the total triboelectric charges, W and L are the width and length of the two sliding surfaces, respectively. Meanwhile, in our case, compared with the PTFE's thickness, the charged line is considered to be infinitely long, thus,

$$\theta = 90^\circ \quad (7.7)$$

Upon combination and simplification, E_{sl} can be expressed as

$$E_{sl} = \frac{q}{2\pi\epsilon_0 Wl\sqrt{(t^2+l^2)}} \quad (7.8)$$

However, only the component along Z axis of the electric field strength E_{sl} is parallel to the electric field, making the effective electric field strength expressed as

$$E_{eff} = E_{sl} \cdot \sin \beta \quad (7.9)$$

$$\sin \beta = \frac{t}{\sqrt{t^2+l^2}} \quad (7.10)$$

Upon combination and simplification,

$$E_{eff} = E_{sl} \cdot \sin \beta = \frac{q}{2\pi\epsilon_0 Wl} \cdot \frac{t}{(t^2+l^2)} \quad (7.11)$$

Thus, the total electric field strength $E_{1 \rightarrow 2}$ generated at P_2 along the z-axis by the triboelectric charges on the entire displaced area of the upper surface can be calculated as

$$E_{1 \rightarrow 2} = \int_0^l \frac{q}{2\pi\epsilon_0 Wl} \cdot \frac{t}{(t^2+l^2)} dl = \frac{q}{2\pi\epsilon_0 Wl} \cdot \tan^{-1} \left(\frac{l}{t} \right) \quad (7.12)$$

Submit the Equation (7.12) into the Equation (7.14)

$$U_{Al} = \int_0^t E_{1 \rightarrow 2} \cdot dt = \int_0^t \frac{q}{2\pi\epsilon_0 Wl} \cdot \tan^{-1} \left(\frac{l}{t} \right) dt \quad (7.13)$$

Finally, the open-circuit voltage V_{oc} between the two electrodes can be expressed as

$$V_{oc} = U_{Al} = \frac{q}{2\pi\epsilon_0 Wl} \cdot \left[\frac{1}{2} \ln(t^2 + l^2) + t \tan^{-1} \left(\frac{l}{t} \right) \right] \quad (7.14)$$

The EDP is essentially the open-circuit voltage (V_{oc}) that can be experimentally measured. The theoretical prediction on the V_{oc} from the analytical mode fits the trend of the experimental data (Figure 7.4). These two sets of results both reveal that the V_{oc} drastically increases once the displacement occurs and quickly reaches a nearly saturated

value. This observation can be derived from Equation 7.14 on the condition that the sliding surface has lateral dimensions that are much larger than the PTFE's thickness ($L \gg t, W \gg t$).

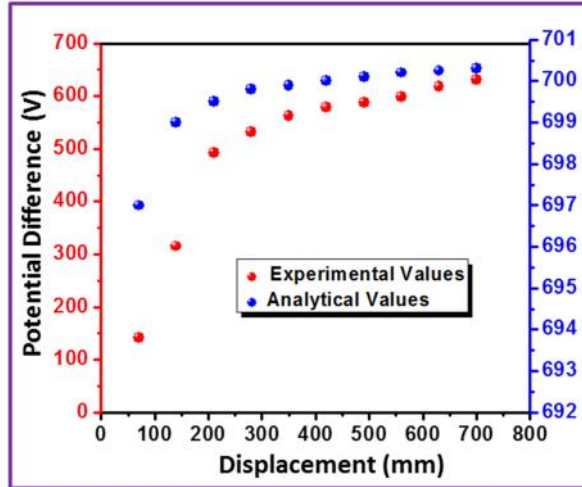


Figure 7.4 Electric potential difference between the aluminum electrode and the copper electrode as a function of the displacement. Red dots and blue dots represent experimental values and analytical values, respectively.

It is noticed in Figure 7.4 that the theoretical values saturate faster than the experimental values. It is likely to result from the simplifications made in the analytical derivation and non-ideal factors in experiment such as rough sliding surfaces and thus inevitably created gap in between. Therefore, the actual separation between the electrodes along vertical direction during sliding may be much larger than the PTFE's thickness, making the experimental values saturate at a slower rate.

Short-circuit current

If the two electrodes are electrically connected, once displacement is established, the uncompensated negative triboelectric charges on PTFE will repulsively drive free

electrons on the copper electrode to the aluminum electrode, neutralizing the positive triboelectric charges and leaving behind positive inductive charges (Figure 7.5 B).

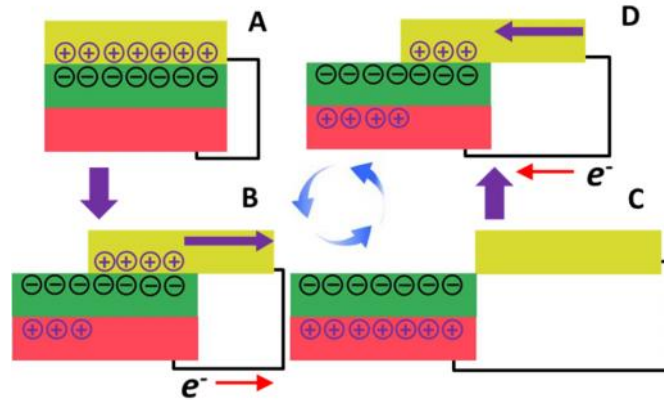


Figure 7.5 A cycle of electricity generation process for illustrating the mechanism of the TEG. (A) fully aligned position; (B) the two surfaces are sliding apart; (C) fully displaced position, and (D) the two surfaces are sliding back together.

The flow of inductive electrons lasts until the displacement reaches the maximum. Based on our assumptions made in the analytical model, the inductive charges equal the triboelectric charges in quantity. Therefore, at fully displaced position, the positive triboelectric charges are completely balanced out by inductive electrons (Figure 7.5 C), indicating no more current flow. As the displacement is diminished by the reciprocating force, the inductive electrons flow back to the copper electrode (Figure 7.5 D) until the fully aligned position is restored. Therefore, in the entire process, alternating current (AC) is produced through the external load.

7.2.3 Electric measurement results and discussion

To characterize the performance of an TEG with a plate size of 6.4 cm by 3.8 cm, the short-circuit current (I_{sc}) and open-circuit voltage (V_{oc}) were measured at an average sliding velocity of 0.6 m/s introduced by a linear motor. As shown in Figure 7.6 A, the I_{sc} exhibits peaks of alternating directions.

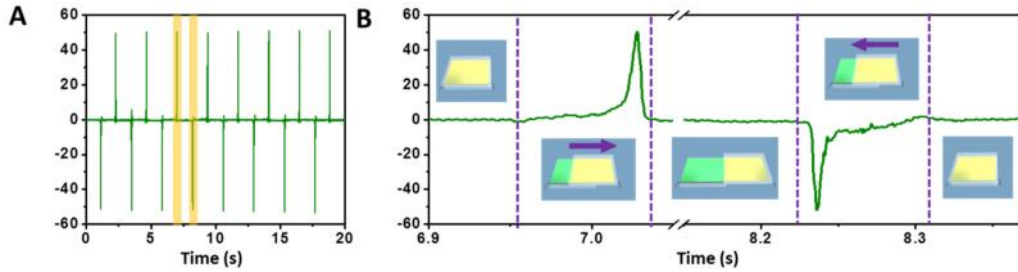


Figure 7.6 Current output of the sliding triboelectric NG. (A) Short-circuit current (I_{sc}) and (B) enlarged view of a cycle highlighted in (A). Insets: relative positions between the two sliding surfaces that correspond to the I_{sc} result.

An enlarged view of two adjacent peaks is displayed in Figure 7.6 B. Increasing displacement gives a positive current peak, while shrinking displacement leads to a negative one. No electric current is produced at either aligned or entirely displaced position, as illustrated by insets in Figure 7.6 B. The V_{oc} switches between zero and a maximum value, which corresponds to the aligned and fully displaced positions, respectively (Figure 7.7 A). The experimentally obtained results are fully consistent with the aforementioned theoretical analysis. Enabled by a full-wave diode bridge, the AC electric output can be rectified to a DC signal (Figure 7.7 B).

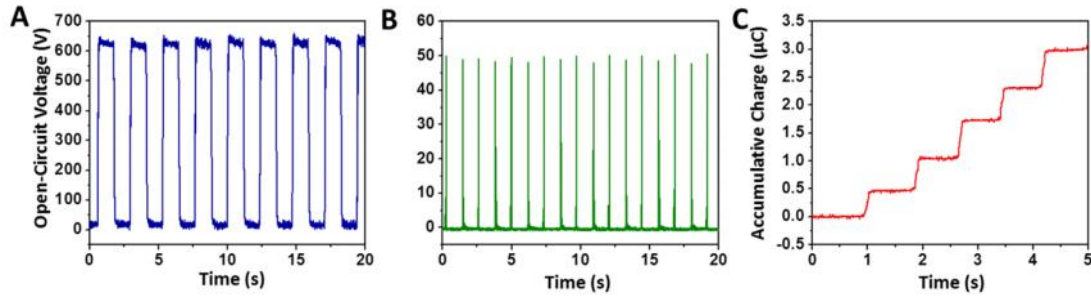


Figure 7.7 Electric measurement results of the sliding triboelectric NG. (A) Open-circuit voltage (V_{oc}); (B) Rectified current by a full-wave diode bridge; (C) Accumulative inductive charges generated by the TEG. Each step represents a one-way sliding process across the entire length of the TEG. The diode bridge is used so that the inductive charges can be added up. Note: The TEG has a size of 6.4 cm by 3.8 cm.

With the diode bridge, the total accumulative inductive charges, independent of sliding direction, can be added up. Demonstrated in Figure 7.7 C, every step represents an output current resulting from a one-way sliding motion, generating $0.6 \mu\text{C}$ of inductive charges on average. Correspondingly, the area density of the triboelectric charges is calculated to be $257 \mu\text{C}/\text{m}^2$, which is consistent with previous reports¹¹⁵.

7.3 Grating design

7.3.1 Structure and fabrication

Introducing linear grating on the sliding surfaces enables the new principle to become an extremely efficient means for energy harvesting; and it is far superior to the previously demonstrated ones in total output charge, current frequency and efficiency. Linear grating with uniform period is fabricated on both sliding surfaces. The rows of grating units have the same size as intervals in between, with all rows being electrically

connected at both ends by two buses. The grating patterns on both sliding surfaces are identical so that they can match well with each other when aligned.

The fabrication process of the grating TEG is illustrated in Figure 7.8.

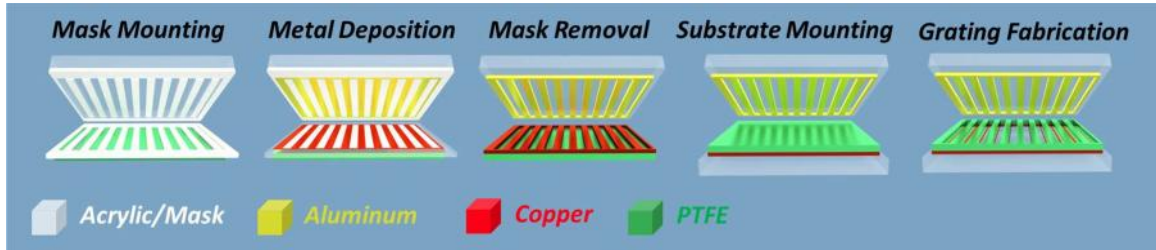


Figure 7.8 Fabrication process of a grating TEG.

Two acrylic substrates with a size of 6.4 cm by 3.8 cm by 0.16 cm were prepared by laser cutter. Two identical sets of masks for the grating pattern were also fabricated from acrylic by the laser cutter. One mask was mounted onto a substrate, while the other one was mounted onto the PTFE film. Then aluminum and copper were deposited through the open window areas of the masks onto the substrate and the PTFE film, respectively. After deposition, the masks were removed. The copper-coated PTFE was adhered to the other substrate with the un-coated surface on the top. Grating structure was created on the PTFE surface by cutting off the area that has no copper coating on the other side. Finally, the two substrates were brought together with the aluminum contacting the un-coated PTFE. Metal wires were connected to the two metal electrodes for measurement.

7.3.2 Operation principle

Although the grating design reduces the total contact area by half thus seemingly sacrifices half of the triboelectric charges, it increases the percentage of the mismatched area to 100% for a displacement of only a grating unit length rather than the entire length of the TEG so that it dramatically increase the transport efficiency of the inductive charges. Inductive free electrons can be pumped back and forth between electrodes for multiple times due to the grating structure, providing multi-folds of output charge compared to a non-grating TEG. Every row of the grating units can be considered as a reduced-sized TEG; and it is in parallel connection with all other rows through buses. In contrast to a non-grating TEG that needs to be fully displaced in order to complete pumping of the inductive charges for one time, the grating TEG only requires a displacement of a unit length to completely transport the inductive charges, largely improving the energy conversion efficiency. With further displacement of another length of the unit, back flow of the inductive charges can be realized. Therefore, for a one-way sliding process across the whole length of the TEG, the inductive charges can be pumped for $(2N-1)$ times in total, where N is the number of grating units. If we take into account that the contacting area decreases as the two surfaces slide apart, the following equation represents the total inductive charges Q that the grating TEG can provide for a single sliding across the entire length of the TEG:

$$\begin{aligned}
Q &= Nq' + |-q' \times (N - 1)| + q' \times (N - 1) + \dots + |-q'| + q' \\
&= Nq' + 2q' \times \sum_{i=1}^{N-1} i d \\
&= (2q'N)N/2d
\end{aligned} \tag{7.15}$$

where q' is the inductive charges generated from a single grating unit for a displacement of the unit length.

The total maximum inductive charges generated by a non-grating TEG of the same length is $2q'N$. Therefore, Equation 7.15 indicates that the total inductive charges linearly increase with the grating density.

7.3.3 Electric measurement results and discussion

To validate the above analysis, electrical measurement was performed on a grating TEG that has two units (inset in Figure 7.9 A) with unit length of $W = 1.5$ cm. Results of I_{sc} , V_{oc} , rectified current and accumulative charges are presented in Figure 7.9, respectively.

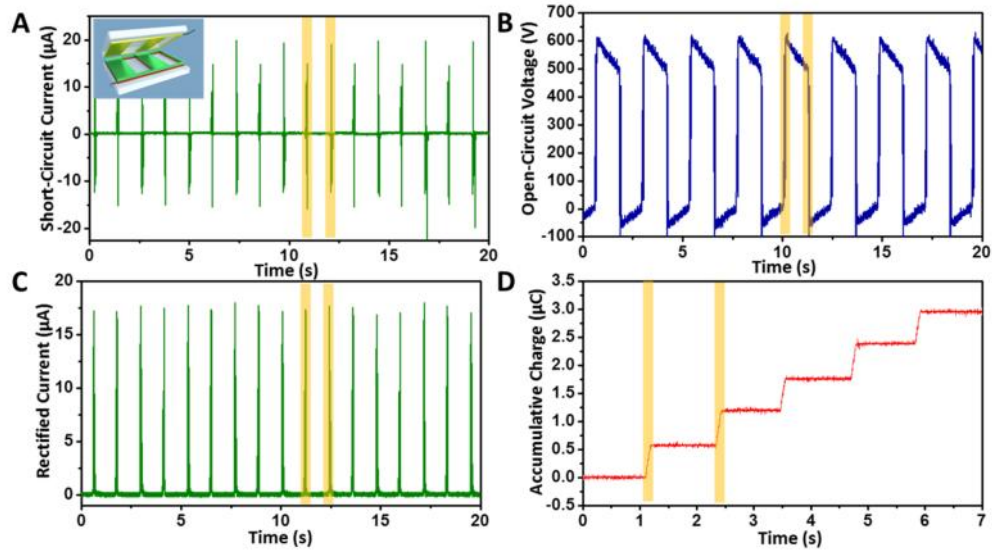


Figure 7.9 Electric measurement results of the sliding triboelectric NG that has two gratings. (A) Short-circuit current (B) open-circuit voltage of the TEG. (C) Rectified current and (D) accumulative inductive charges generated by the TEG.

Figure 7.10 displays the measured results in a sliding process from aligned position to a fully displaced position. The I_{sc} for the grating TEG exhibits alternating

direction, producing a total of three current peaks (Figure 7.10 A2). It indicates that the inductive electrons are pumped back and forth between electrodes for three times. Correspondingly, the Voc oscillates between zero and the maximum value also for three times (Figure 7.10 A3). By a diode bridge, all of the three current peaks are completely rectified (Figure 7.10 A4), leading to accumulative inductive charges that can be added up (Figure 7.10 A5). Close inspection on Figure 7.10 A2 and Figure 7.10 A5 reveals that the first current peak delivers twice as much charge quantity as the second and the third peaks. The total inductive charges provided by all of the three current peaks reach approximately 0.6 μC . This quantity equals that from a non-grating TEG, which is consistent with Equation 7.15. If sliding direction is reversed as indicated in Figure 7.10 B, measurement results are also reversed in both polarity and sequence.

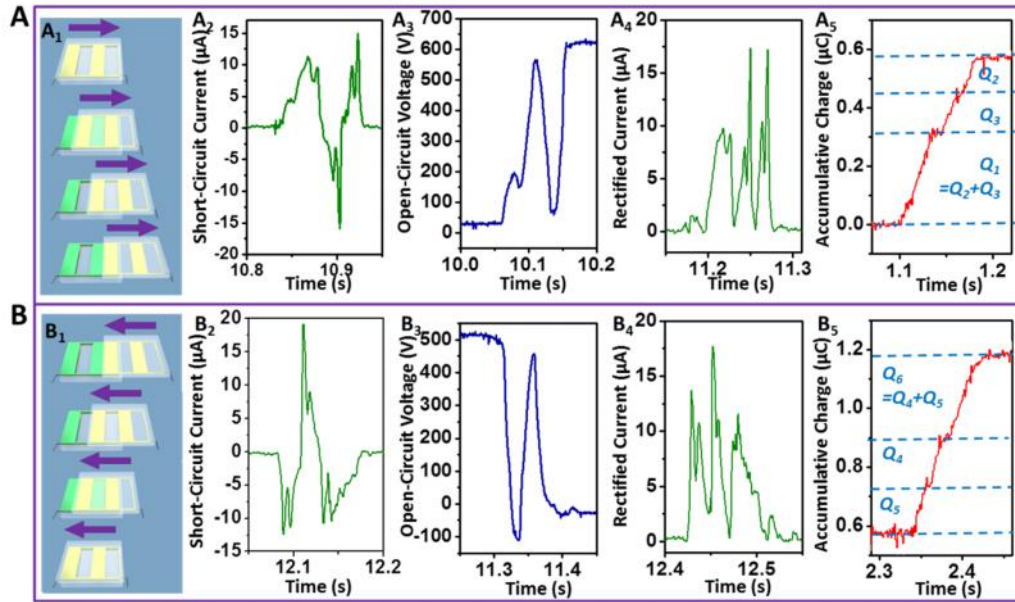


Figure 7.10 Detailed examinations on electric measurement results of the sliding triboelectric NG that has two gratings. (A) Electrical measurement results as the two surfaces are sliding apart. (A1) different stages of the sliding process; (A2) enlarged view of the I_{sc} in the first highlighted section in Figure 7.9 A; (A3) enlarged view of the V_{oc} in the first highlighted section in Figure 7.9 B; (A4) enlarged view of the rectified current in the first highlighted section in Figure 7.9 C, and (A5) enlarged view of the accumulative charges in the first highlighted section in Figure 7.9 D. (B) Electrical measurement results as the two surfaces are sliding back together. (A1) different stages of the sliding process; (A2) enlarged view of the I_{sc} in the second highlighted section in Figure 7.9 A; (A3) enlarged view of the V_{oc} in the second highlighted section in Figure 7.9 B; (A4) enlarged view of the rectified current in the second highlighted section in Figure 7.9 C, and (B5) enlarged view of the accumulative charges in the second highlighted section in Figure 7.9 D. Note: The TEG has a size of 6.4 cm by 3.8 cm with unit length of 1.6 cm.

Experimental data from grating TEGs with more units further confirm the validity of our theoretical analysis. For a single sliding process, the I_{sc} data produced by grating TEGs having 6, 8 and 10 units are presented in Figure 7.11, corresponding to a unit

length of 0.5 cm, 0.4 cm and 0.3 cm, respectively, with a constant full length of the TEG (6.4 cm). The total counts of AC peaks are in accordance with Equation 7.14.

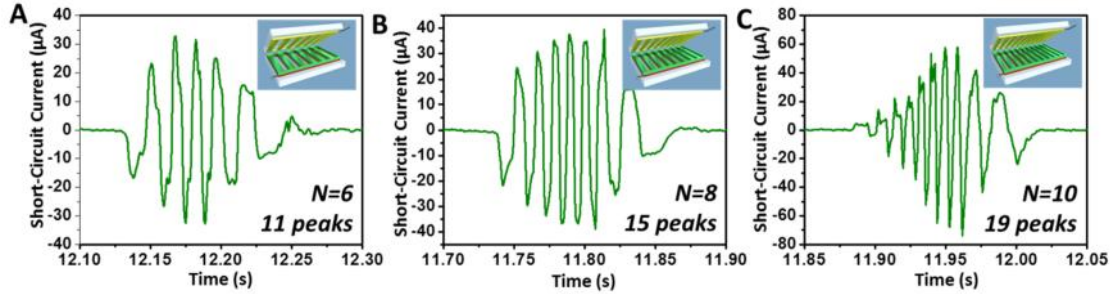


Figure 7.11 Current output results of the sliding triboelectric NG that has multiple gratings. (A) Short-circuit current of a grating TEG with 6 grating units for a single sliding process across the full width of the TEG. Inset: schematic of the TEG structure. (B) Short-circuit current of a grating TEG with 8 grating units for a single sliding process across the full width of the TEG. Inset: schematic of the TEG structure. (C) Short-circuit current of a grating TEG with 10 grating units for a single sliding process across the full width of the TEG. Inset: schematic of the TEG structure.

The enhancement of charge output by the grating structure is plotted in Figure 7.12. With 10 grating units, a total of $2.8 \mu\text{C}$ of inductive charges can be generated within 6.4 ms at a sliding velocity of 10 m/s, which is equivalent to a continuous DC source of 0.44 mA.

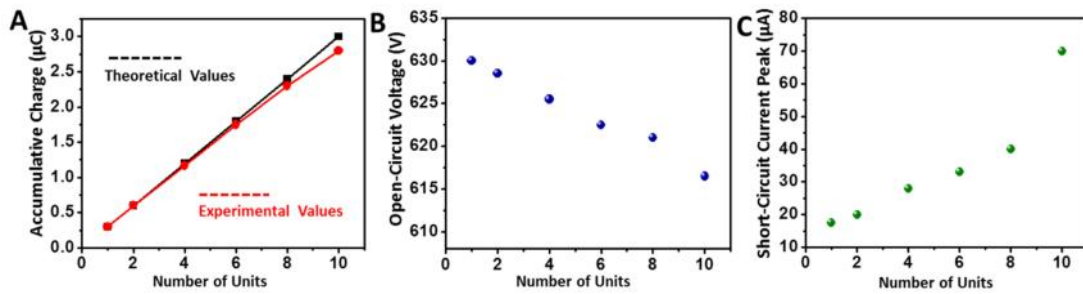


Figure 7.12 Dependence of the sliding NG's output power on the number grating units. (A) Accumulative inductive charges generated for a single sliding process across the full width of a TEG as a function of grating units. (B) Open-circuit voltage as a function of grating units. (C) Maximum values of short-circuit current as a function of grating units.

Ideally, according to Equation 7.14, the total inductive charges are proportional to the density of the grating units. If the grating size is further scaled down to $30\ \mu\text{m}$, an ideal enhancement of another 100 times is expected, making the TEG comparable to various types of solar cells in output current and in current density¹⁴²⁻¹⁴⁴. An estimation for the $N = 10$ gives an output conversion efficiency of $\sim 8-31\%$ (supporting information).

Though the experimental data closely match the theoretical values for $N \leq 4$, slight deviation starts to appear if N further increases (Figure 7.12 A). The deviation may be attributed to two probable reasons. The first is non-ideal orientation mismatch. The two sliding surfaces are likely to have an angle of mismatch that is introduced by experimental operation. As the length of the grating units shrinks, the angle of mismatch will exert more substantial effect on the effective contact area between the two surfaces, leading to increasingly reduced output charge. This effect can be largely eliminated by more precise alignment during experiment operation. Secondly, we suggest that

assumptions made in the analytical theory may become imprecise for very fine grating units due to the edge effect of each unit. The assumption of infinite charged plane will no longer hold once the grating edges can dominantly affect the electric field distribution, leading to reduced quantity of inductive charges. Further systematic investigation by both experiment and simulation is required to quantitatively understand this non-ideal effect. As diagramed in Figure 7.12 B, the V_{oc} is only weakly related to the number of grating units, though slight reduction can be observed. The reduction can also be attributed to the increasingly stronger effect from the mismatched angle. The advantages of the grating structure include not only the enhanced total transported charges but also improved output current. With constant sliding velocity, finer grating shortens the time to transport inductive charges between the electrodes for one time, resulting in higher output current (Figure 7.12 C). However, the peak of I_{sc} does not increase linearly with the number of units, which may result from non-uniform velocity during sliding process.

The principles demonstrated for the grating TEG can be applied to other configurations (Figure 7.13), greatly extending the practicability of this technology. Besides the planar design, other configurations include, but not limited to, concentric discs having relative rotation (Figure 7.13 A) and coaxial tubes having rotational motion (Figure 7.13 B) and piston motion (Figure 7.13 C). With these diverse designs, no matter whether the triggering force is intermittent impact or continual press, the sliding electrification principle of the TEG becomes a versatile solution to harvesting multiple forms of ambient mechanical energy, including translation, rotation/ rolling.

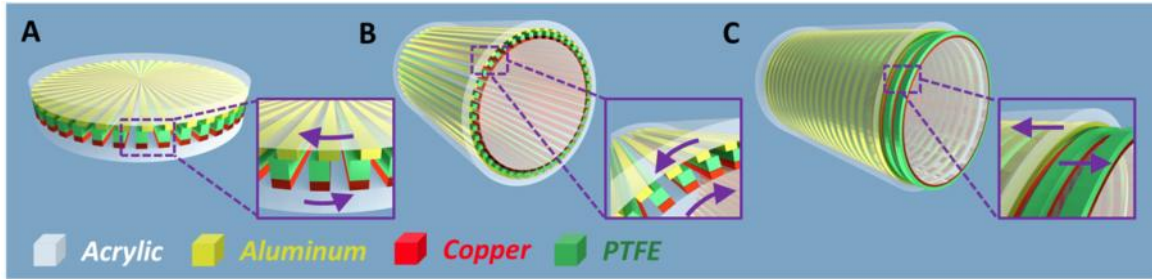


Figure 7.13 Different configurations in which the sliding mode can be applied. (A) Two concentric discs that can harvest energy from rotation. Inset: enlarged view that shows the rotational directions. (B) Two co-axial tubes that can harvest energy from rolling. Inset: enlarged view that shows the rolling directions. (C) Two co-axial tubes that can harvest energy from linear piston motion. Inset: enlarged view that shows the moving directions.

7.4 Summary

In summary, we invented a new principle of grating TEG based on sliding electrification. The sliding between the two contact surfaces lead to uncompensated triboelectric charges on displaced areas, which drive inductive charges between electrodes. Linear grating enables substantial enhancements of output charge, output current and current frequency. With 10 grating units that are 3 mm in length for each, the TEG is effectively equivalent to a continuous DC source of 0.44 mA (corresponding current density of 0.18 A/m^2), and an energy conversion efficiency of 8-31% has been demonstrated. Finer grating units can further greatly boost up the electric output, though non-linear effect needs to be investigated in order to achieve optimal design. The basic concept and design demonstrated in this work can be extended to other configurations that are applicable to harvest multiple forms of ambient mechanical energy. Therefore, this work lays a fundamental groundwork for a versatile solution to harvesting diverse

forms of mechanical energy, including rolling wheels, wind power, and water flow. Furthermore, the demonstrated principle can also be used to design self-powered motion sensors (active sensors) for detecting translation or rotational motions.

CHAPTER 8

SELF-POWERED APPLICATIONS

8.1 Storage-assisted applications for laterally integrated ZnO NW based nanogenerator

Storing the generated energy and driving functional devices are extremely important steps towards practical applications of the nanogenerator. In this work, they were accomplished by using a charging-discharging circuit with two consecutive steps (Figure 8.1). The circuit function is determined by the status of a switch (Figure 8.1 A inset). The switch is at position A for energy storage achieved by charging capacitors. Upon charging completion, the switch is switched to position B for energy releasing to power a functional device, such as a light emitting diode.

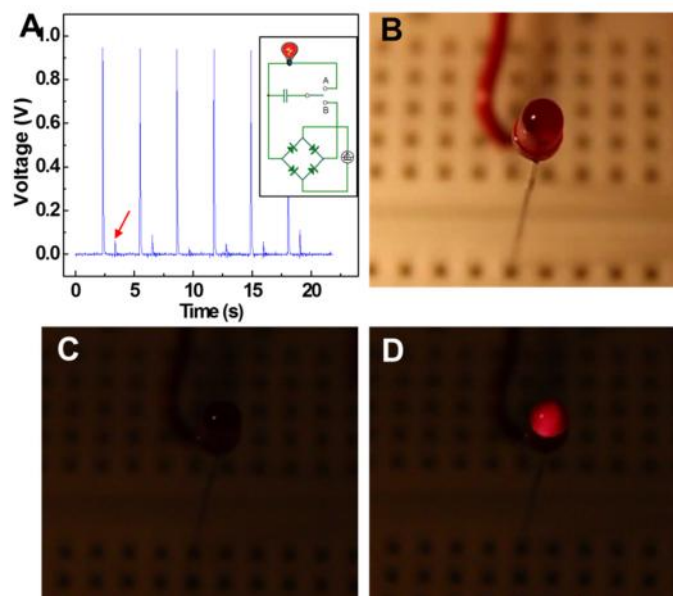


Figure 8.1 Powering a LED by a laterally integrated NG with storage assisted self-powered mode. (A) The electric output measured after a full wave rectifying bridge. Signals of negative signs are reversed, as pointed by the arrow. Inset: Schematic of the charging-discharging circuit for storing and releasing the energy generated by a laterally integrated ZnO NW based nanogenerator. (B) Image of a commercial LED, which is incorporated into the circuit. (C) Image of the LED in dim background before it is lit up. (D) Image of the LED in dim background at the moment when it is lit up by the energy generated from the nanogenerator.

It is the key for a successful and effect energy storage to take full advantage of the alternating output. As a result, an integrated full wave rectifying bridge was connected between the NG and capacitors. The output of the NG measured after the bridge exhibits only positive signals (Figure 8.1 A). Full wave rectification achieved by the bridge ensures energy storage at an enhanced efficiency, although the rectified signal (as pointed by an arrowhead in Figure 8.1 A) has appreciably reduced magnitude due to the reverse current leakage of the diodes in the bridge; and this reducing effect is rather notable at

small output current. In order to facilitate the charging process, the output frequency of the NG was tuned up to 3 Hz by reducing the periodicity of the mechanical deformation. Ten capacitors were connected in parallel such that they were simultaneously charged, and the voltage across a single capacitor finally reached 0.37 V.

Upon finishing charging, the capacitors were reconfigured from parallel connection to series connection, leading to a total voltage source of 3.7 V. The stored electricity was used to drive a commercial red LED (Figure 8.1 B), which has an emission spectrum centered at 635 nm. The turn-on voltage and forward-biased resistance are 1.7 V and 450 Ω , respectively. The discharging process was triggered, leading to a maximum discharging current of 4.5 mA and the LED was lit up. The emitted light lasted 0.1 s-0.2 s and was clearly captured in dim background (Figure 8.1 C D and Supplementary video 1). During the whole charging-discharging process, no other power sources were involved. The entire circuit is essentially a complete self-powered system, which consists of three components: an energy harvester (the NG), storage units (capacitors), and a functional device (the LED).

An effective energy generation efficiency is defined as the ratio between the energy stored by the capacitors and the strain energy input to all of the active NWs, and it takes into account the performance of the electronic components in the circuit. The total electrical energy stored by the capacitor can be calculated as $W_{\text{stored}}=CU^2n/2=1.37 \mu\text{J}$, where C is the capacitance of a single capacitor, U is voltage across the capacitor, n is the number of capacitors. Since the dominant strain in the ZnO NWs is tensile strain, with shear strain safely neglected, the totally strain energy can be estimated as $W_{\text{strain}}=\pi D^2L_0E\varepsilon^2fn_0/8=30 \mu\text{J}$, where D is the diameter of the NW (200 nm), L_0 is its

original length (10 μm) which is fixed by the electrode spacing, E is the Young's modulus (30 GPa), ε is the strain of NWs (0.1%), f is the frequency of deformation (3 Hz), t is the total charging time (7200 s), and n_0 is the number of integrated NWs (300,000). Therefore, the effective energy generation efficiency is estimated to be $\sim 4.6\%$. This value is naturally lower than the energy conversion efficiency of a single nano/micro wire ($\sim 7\%$), which is defined as the ratio between the generated electric energy ($W_{\text{generated}} = \int VI dt$, where V is the voltage, and I is the current) and the mechanical input strain energy. This is mainly attributed to the energy dissipation on rectifying bridge and capacitors, as elaborated in the supplementary materials.

8.2 Real time applications

8.2.1 Functional electrical simulation by vertically integrated ZnO NW based NG

Using the instantaneous electric output of the NG pad for each palm impact, we successfully achieved real-time FES of a sciatic nerve of a frog. For a nerve cell at rest, it is normally polarized with a negative transmembrane potential.¹⁴⁵ At excitation, depolarization of the membrane is elicited by opening up voltage-gated ion channels. The cycle of depolarization and repolarization, also called the action potential, propagates through the nerve to activate motor tracts supplied to a muscle. As a consequence, muscle contraction is induced. Therefore, a voltage input equal to or greater than the threshold voltage above the resting potential would be required for firing of the action potential.¹⁴⁶ For a frog's sciatic nerve, the cells' resting potential ranges from -60 to -80 mV, and a voltage input of at least 50 mV at 1 Hz is necessary for innervation of the sciatic nerve.¹⁴⁵⁻¹⁴⁸ The NG pad was connected to an amputated hind limb of a frog by inserting the positive and negative terminals of the NG pad into the white corded sciatic nerve..

Throughout the experiment, the nerve was kept wet by Ringer’s solution for amphibians. A human palm impacted the NG pad to generate electric impulses. Under the instantaneous electrical input, vibrant foot twitching was observed, resulting from contraction of the gastrocnemius muscle, as visualized in Figure 8.2.

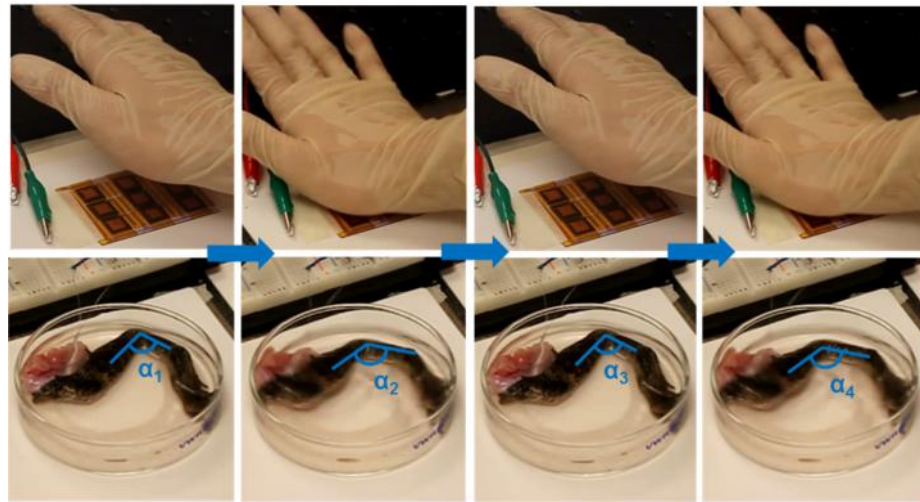


Figure 8.2 Pictures that visualize real-time stimulation of the functional electrical stimulation by the NG pad. The leftmost pair and the second pair on the right correspond to intervals between impacts, with the gastrocnemius muscle at a standstill. The second pair on the left and the rightmost pair correspond to moments of impacts, with contraction of the gastrocnemius muscle. We use a α angle to characterize the instantaneous change in muscle shape as a result of the electric stimulation: α_1 equals α_3 , while α_2 equals α_4 .

The palm impact and foot twitching were perfectly synchronized (Supplementary video 2), indicating real-time stimulation using the electricity generated by each impact of a palm. Since the resistivity of the nerve soaked with Ringer’s solution was very small, the actual voltage drop between the two terminal leads were expected to be much lower than the open-circuit voltage of the NG but still large enough to achieve FES.

8.2.2 Electrochemical deposition by triboelectric NG

We successfully achieved cyanide-free PED of silver structure on micrometer scale by using a triboelectric NG generator as a power source. The resultant electroplated silver material has excellent uniformity, density, and surface smoothness, which is suitable for either thin film deposition or structure fabrication.

The process of creating a desired silver structure is schemed in Figure 8.3 A. We deposited a silicon substrate with gold, followed by growth of silicon dioxide as a mask layer. High work function of gold ensures that it only acts as a seed material but not reacts with plating solution. Standard photolithography was conducted to generate the desired pattern on the oxide, which was then etched through so that gold surface with the defined pattern was exposed. Subsequently, electroplating was performed with the gold surface as the cathode and silver metal as the sacrificial anode. Finally, the oxide layer was removed by isotropic wet etching.

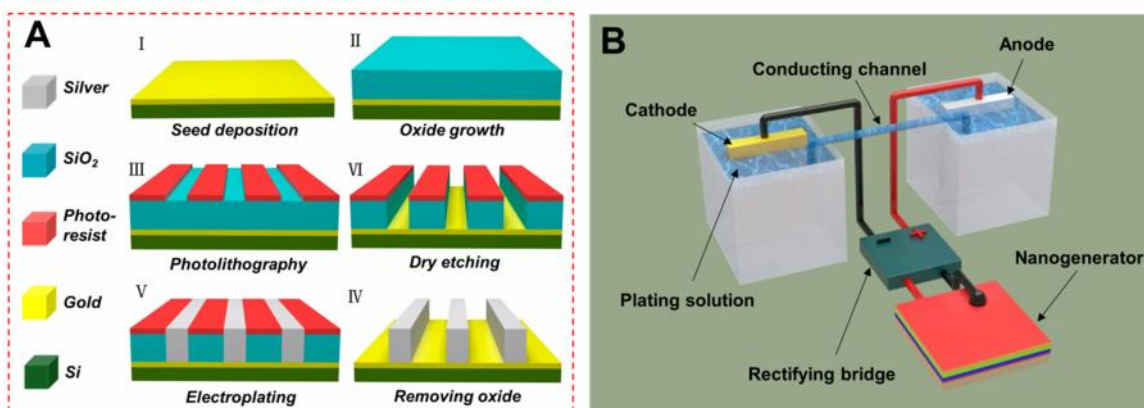


Figure 8.3 Experimental setup for electrodeposition. (A) Sketches that illustrate the process for fabricating the silver structure. (B) Setup for the pulse electrodeposition.

The setup for electroplating is schemed in Figure 8.3 B. Preparation of the plating solution is described as follows. In the first step, silver nitrate solution, sulfosalicylic acid

solution, ammonium acetate solution and potassium hydrate solution were prepared in separate containers. Then the silver nitrate solution was added into the potassium hydrate solution, forming dark-brown precipitate of silver hydroxide. Such a suspension was then added into the sulfosalicylic acid solution with strong agitation. After the precipitate disappears, the ammonium acetate solution was added. Finally, aqueous ammonia and DI water were applied to adjust pH and volume of the solution to desired levels, respectively. No additives, such as surfactant or brightening agent, were applied. The recipe for the solution is tabulated in the supplementary materials.

Different from conventional electroplating in which cathode and anode are bathed in the same container, our setup has separated baths that were connected by a long and thin hollow channel filled with the plating solution. As previously discussed, electric voltage delivered by the generator across an external load is a function of resistance. The purpose of adding the conducting channel is to increase the resistance of the solution so that a sufficient voltage between the cathode and the anode can be established for effective electroplating.

The voltage across the two electrodes and the current passing through the solution are demonstrated in Figure 8.4 A and Figure 8.4 B, respectively. The alternating electric output can be rectified by a full-wave bridge, resulting in bursts of pulses that are suitable for PED. Compared to DC power source, the pulsed waveform can significantly raise the limiting current density by replenishing metal ions in the diffusion layer¹⁴⁹. Besides, metal ions are able to migrate to depleted regions with high current density, such as edges and corners¹⁵⁰. Therefore, with improved mass transport and more evenly distributed ions, not only higher plating rate but also better coating quality is expected to be achieved¹⁴⁹. By modifying pulse parameters, deposits with desired composition, morphology, porosity and hydrogen content could be obtained^{151, 152}.

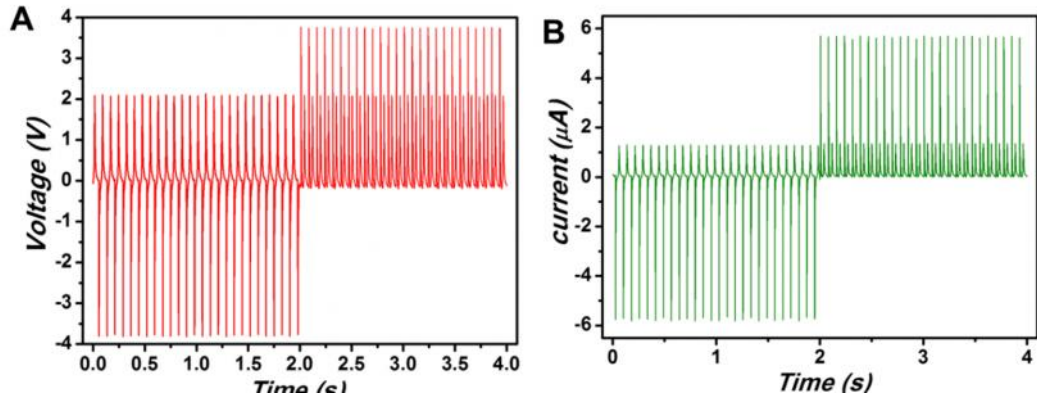


Figure 8.4 Electric measurement results of the contact triboelectric NG as the power source for electrodeposition. (A) Electric voltage between the cathode and the anode with (right half) and without (left half) rectification. (B) Electric current through the plating solution with (right half) and without (left half) rectification.

The waveform delivered by the generator is distinct from previously demonstrated waveforms. It provides pulses with constantly changing magnitude. Here, we have three independent variables, viz, (i) ON-time (TON), (ii) OFF-time (TOFF) and (iii) total charge within a cycle (Q). Based on these three variables, some characteristic pulse parameters can be calculated as below (supplementary materials):

$$\text{Duty cycle ()} = \frac{T_{ON}}{T_{cycle}} = \frac{(T_{ON1} + T_{ON2})}{(T_{ON} + T_{OFF})} \times 100\% = 42.9\% \quad (8.1)$$

$$\text{Average cathodic current density (IA)} = \frac{Q}{ST_{cycle}} = \frac{\int_0^{T_{cycle}} I(t) \cdot dt}{ST_{cycle}} = 0.38A / dm^2 \quad (8.2)$$

where S is the effective area of the work piece that is actually being deposited.

The SEM images of the electroplated silver structure are displayed by Figure 8.5 A and Figure 8.5 B. The deposit protrudes from the surrounding surface. It is clearly and uniformly defined. Further zoomed-in view reveals that extremely fine grain size from 0.1 μm to 0.5 μm are densely packed. The deposit is confirmed to be silver by EDS

analysis results, as demonstrated in Figure 8.5 D. The cathodic current efficiency was calculated to be 86.6%. Further systematic investigations are still needed to understand how the specific waveform affects properties of the deposit.

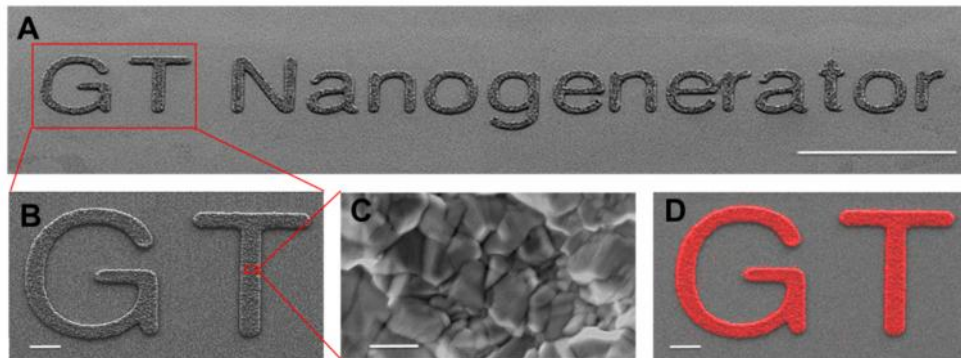


Figure 8.5 Results of the electrodeposition powered by the contact triboelectric NG. (A) SEM image of the deposit showing clearly and uniformly defined structure (tilted angle of 45 degree). The scale bar is 100 μm . (B) SEM image of the deposit with enlarged view (tilted angle of 45 degree). The scale bar is 5 μm . (C) SEM image of the densely packed grain structure. The scale bar is 200 nm. (D) EDS mapping which confirms the deposit is silver. The red color represents silver spacial distribution. The scale bar is 5 μm .

8.2.3 Powering LEDs by scalable triboelectric NG

The superior power output of the NG enables tremendous applications, not just only for powering a single small electronics. Here we demonstrated an application of the NG on a large scale, simultaneously driving a large number of electronic devices. Arrays of commercial multi-color LED lamps were assembled in serial to fabricate LED panels. The NG serves as a sole and direct power source for the LEDs. Triggered by human footfalls, the NG generated current pulses, instantaneously lighting up as many as 600 LED lamps (Figure 8.6). The footfalls and light emission were synchronized, indicating that the NG was a real-time power source (see Supplementary Movie 3, Supplementary Movie 4, and Supplementary Movie 5). This successful demonstration indicates other

immediate applications, such as self-lighting shoes and self-lighting tiles which can be luminous upon footfalls.

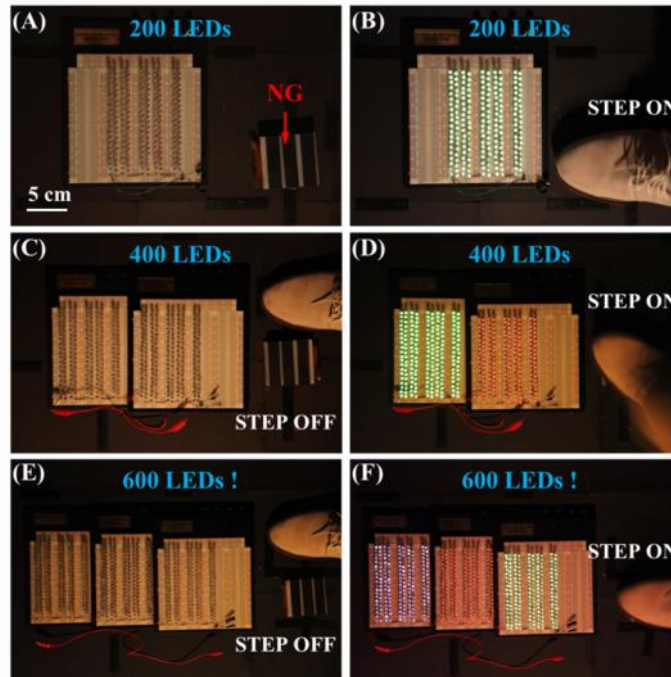


Figure 8.6 Pictures that show the scalable triboelectric NG as a power source for hundreds of LED bulbs. (A) Photograph of a setup in which the NG acts as a direct power source for 200 commercial green LED lamps and (B) when footstep falls on the NG, simultaneously lighting up the LEDs in real-time. (C) Photograph of a setup in which the NG acts as a direct power source for 200 commercial green and red LED lamps, respectively and (D) When footstep falls on the NG, simultaneously lighting up the LEDs in real-time. (E) Photograph of a setup in which the NG acts as a direct power source for 200 commercial green, red and blue LED lamps, respectively and (F) When footstep falls on the NG, simultaneously lighting up the LEDs in real-time. Note: all LEDs are connected in serial.

CHAPTER 9

CONCLUSION

Self-powered electronics based on energy harvesting technology are of great significance to address limitations of traditional power supplies in a number of cases. My research targets on two types of mechanical energy harvesting techniques that are cost effective and scalable, trying to solve their current limitations and aiming at developing practical self-powered electronics. Substantial improvements have been made on both of the techniques, as summarized below.

For NGs based on ZnO NWs, two types of integrated NGs were developed, integrating a large number of ZnO NWs together instead of using a single NW. One of them is NGs based on laterally integrated NWs. I managed to transfer vertically grown ZnO NWs to a flexible substrate and achieved horizontally aligned NW arrays that have crystallographic alignment, based on which an innovatively designed NG was fabricated. The electrical output of the NG reached a peak voltage of 2.03 V and current of 107 nA, with a peak power density of $\sim 11 \text{ mW/cm}^3$. An effective energy generation efficiency of 4.6% was demonstrated. Another type is NGs based on vertically integrated NWs. The electric output from the NG reached a record high of 58 V and 134 μA , with a maximum power density of 0.78 W/cm^3 , which is by far the highest output power ever achieved by piezoelectric NGs.

For NGs based on triboelectric effect, new mechanisms were developed to take advantage of triboelectric effect to harvest ambient mechanical energy. The new mechanisms gave rise to two types of operating modes. One is contact mode in which energy harvesting is realized through repeated contact and separation between two

different materials that differ in triboelectric polarities. The generator has the virtue of highly simple fabrication/implementation, strong performance and extremely low cost, which properly address limitations of energy-harvesting technology. Maximum short-circuit current of 2.0 mA was obtained. That gives instantaneous power output of 1.2 W, power density of 313 W/m^2 , average power output of 132.1 mW, open-circuit voltage of $\sim 1200 \text{ V}$, and energy conversion efficiency of 9.8% at device level. It unravels large-scale applications of the NG and broadens our horizons on the capability of the NG. Another mode is sliding mode in which displacement between two materials lead to transport of inductive charges back and forth in the external circuit. Linear grating enables substantial enhancements of output charge, output current and current frequency. With 10 grating units that are 3 mm in length for each, the TEG is effectively equivalent to a continuous DC source of 0.44 mA (corresponding current density of 0.18 A/m^2), and an energy conversion efficiency of 8-31% has been demonstrated.

The developed NGs were employed as power sources for self-powered electronics, which also had two operating modes, i.e. storage assisted mode and real time mode. A variety of applications were demonstrated, including functional electrical stimulation, electrochemical deposition, and powering small electronics. With such a high power output, we vision energy harvesting by the triboelectric NG not only from human footfall but also from rolling wheels, wind power, and ocean waves.

REFERENCES

1. Wang, Z. L. *Sci. Am.* 2008, **298**, 82-87.
2. Wang, Z. L. *Adv. Funct. Mater.* 2008, **18**, 3553-3567.
3. Beeby, S. P.; Tudor, M. J.; White, N. M. *Meas. Sci. Technol.* 2006, **17**, R175-R195.
4. Williams, C. B; Yates, R. B. *Sensors Actuat. A* 1996, **52**, 8-11.
5. El-Hami, M. *et al. Sensors Actuat. A* 2001, **92**, 335-342.
6. Glynne-Jones, P. *et al. Sensors Actuat. A* 2004, **110**, 344-249.
7. Roundy, S.; Wright, P. K. *Mater.Struct.* 2004, **13** 1131-1142.
8. Li, H.; Lal, A; Blanchard, J.; Henderson, D. *J. Appl. Phys.* 2002, **92**, 1479755.
9. Wang, Z. L.; Song, J. H. *Science* 2006, **312**, 242-246.
10. Song, J. H.; Zhou, J.; Wang; Z. L. *Nano Lett.* 2006, **6**, 1656-1662.
11. Wang, X. D.; Song, J. H.; Liu, J.; Wang, Z. L. *Science* 2007, **316**, 102-105.
12. Qin, Y.; Wang, X. D.; Wang, Z. L. *Nature* 2008, **451**, 809-813.
13. Xu.S.; Wei, Y.; Liu, J.; Yang R.; Wang, Z. L. *Nano Lett.* 2008, **8**, 4027-4032.
14. Yang, R.; Qin, Y.; Dai L.; Wang, Z. L. *Nat. Nanotech.* 2009, **4**, 34-39.
15. Janotti, A.; Van de Walle, C. G. *Appl. Phys. Lett.* 2005, **87**, 122102.
16. Janotti, A.; Van de Walle, C. G., *J. Cryst. Growth* 2006, **287**, 58-65.
17. Janotti, A.; Van de Walle, C. G., *Rep. Prog. Phys.* 2009, **72**, 126501.
18. Kohan, A. F. *et al. Phy. Rev B* 2000, **61**, 15019.
19. Michael, H. *et al. Adv. Mater.* 2001, **13**, 113-116.
20. Zhao, M. H.; Wang, Z. L. *Nano Lett.* 2004, **4**, 587-590.
21. Choi, M. *et al. Adv. Mater.* 2009, **21**, 2185-2189.

22. Choi, D. *et al. Adv. Mater.* 2010, **22**, 2187-2192.
23. Chang, C. *et al. Nano Lett.* 2010, **10**, 726-731.
24. Qi, Y. *et al. Nano Lett.* 2010, **10**, 524-528.
25. Pan, Z. W.; Dai, Z. R.; Wang, Z. L. *Science* 2001, **291**, 1947-1949.
26. Kuo, T. *et al. Chem. Mater.* 2007, **19**, 5143-5147.
27. Polyakov, A. Y. *et al. Appl. Phys. Lett.* 2003, **83**, 1575-1577.
28. Huang, M. H. *et al. Adv. Mater.* 2001, **13**, 113-116.
29. Yang, P. *et al. Adv. Funct. Mater.* 2002, **12**, 323-331.
30. Wang, Z. L. *ACS Nano* 2008, **10**, 1987-1992.
31. Wang, Z. L. *et al. Adv. Mater.* 2006, **18**, 3275-3278.
32. Wang, X. D. *et al. Nano Lett.* 2006, **6**, 2768-2772.
33. Wang, X. D. *et al. Adv. Mater.* 2007, **19**, 1627-1631.
34. Huang, M. H. *et al. Science* 2001, **292**, 1897-1899.
35. Zou, B. *et al. J. Phys. Chem. B* 2006, **110**, 12865-12873.
36. Lim, J. H. *et al. Adv. Mater.* 2006, **18**, 2720-2724.
37. Zhang, X. M. *et al. Adv. Mater.* 2009, **21**, 2167-2770.
38. Xu, S. *et al. Adv. Mater.* 2010, **22**, 4749-4753.
39. Law, M. *et al. Nat. Mater.* 2005, **4**, 455-459.
40. Weintraub, B.; Wei, Y.; Wang, Z. L. *Angew. Chem. Int. Ed.* 2009, **48**, 1-6.
41. Wei, Y. *et al. Nano Lett.* 2010, **10**, 2092-2096.
42. Law, M. *et al. Nat. Mater.* 2005, **4**, 455-459.
43. Weintraub, B.; Wei, Y.; Wang, Z. L. *Angew. Chem. Int. Ed.* 2009, **48**, 1-6.
44. Wei, Y. *et al. Nano Lett.* 2010, **10**, 2092-2096.

45. Wang, Z. L. *Nano Today* 2010, **5**, 540-552.
46. Wang, Z. L. *et al. Mate. Sci. Eng. R.* 2010, **70**, 320-329.
47. W. Z. *et al. Adv. Mater.* 2006, **18**, 3275-3278.
48. Chen, L. Y.; Wu, S. H.; Yin, Y. T. *J. Phy. Chem. C* 2009, **113**, 21572-21576.
49. Fang, Y. *et al. J. Phy. Chem. C* 2010, **114**, 12469-12476.
50. Huang, M. H. *et al. Adv. Mater.* 2001, **13**, 113-116.
51. Wang, X. D.; Summers, C. J.; Wang, Z. L. *Nano Lett.* 2004, **4**, 423-426.
52. Song, J.; Wang, X.; Riedo, E.; Wang, Z. L. *J. Phy. Chem. B* 2005, **109**, 9869-9872.
53. Park, W. I.; Yi, G. C.; Kim, M.; Pennycook, S. J. *Adv. Mater.* 2002, **14**, 1841-1843.
54. Hong, J. I.; Bae, J.; Snyder, R. L.; Wang, Z. L. *Nanotech.* 2009, **20**, 085609-058614.
55. Greene, L. E. *et al. Inorg. Chem.* 2006, **45**, 7535-7543.
56. Xu, S. *et al. J. Am. Chem. Soc.* 2008, **130**, 14958-14959.
57. Wei, Y. *et al. Nano Lett.* 2010, **10**, 3414-3419.
58. Pan, Z. W. *et al. Angew. Chem. Int. Ed.* 2005, **44**, 274-278.
59. Mensah, S. L.; Kayastha, V. K.; Yap, Y. K. *J. Phy. Chem. C* 2007, **111**, 16092-16095.
60. Kuo, T. J.; Lin, C. N.; Kuo, C. L.; Huang, M. H. *Chem. Mater.* 2007, **19**, 5143-5147.
61. Li, S.; Zhang, X.; Yan, B.; Yu, T. *Nanotech.* 2009, **20**, 495604-495613.
62. Fan, H. J. *et al. Small* 2006, **4**, 561-568.
63. Campos, L. C. *et al. Appl. Phys. Lett.* 2007, **90**, 181929.
64. Kang, Y. H.; Choi, C. G.; Kim, Y. S.; Kim, J. K. *Mater. Lett.* 2009, **63**, 679-682.
65. Round, S.; Wright, P. K.; Rabaey, J. *Comput. Commun.* 2003, **26**, 1131-1144.
66. Shen, D. N. *et al. Sens. Actuators A-Physical* 2009, **154**, 103-108.
67. Agrawal, R.; Peng, B.; Espinosa, H. D. *Nano Lett.* 2009, **9**, 4177-4183.

68. Wang, Z. L. *Adv. Mater.* 2011, **82**, 279-284.
69. Patolsky, F. *et al. Science* 2006, **313**, 1100-1104.
70. Tian, B. *et al. Science* 2010, **329**, 831-834.
71. Xu, S. *et al. Nat. Nanotechnol.* 2010, **5**, 366.
72. Zhu, G.; Yang, R.; Wang, S.; Wang, Z. L. *Nano Lett.* 2010, **10**, 3151.
73. Hu, Y.; Zhang, Y.; Xu, C.; Zhu, G.; Wang, Z. L. *Nano Lett.* 2010, **10**, 5025.
74. Hu, Y. *et al. Nano Lett.* 2011, **11**, 2572.
75. Hu, Y.; Lin, L.; Zhang, Y.; Wang, Z. L. *Adv. Mater.* 2012, **24**, 110.
76. Jung, J. H. *et al. ACS Nano* 2011, **5**, 10041.
77. Kim, K.; Lee, K. K.; Seo, J.; Kumar, B.; Kim, S. *Small* 2011, **7**, 2577.
78. Chang, C.; Tran, V. H.; Wang, J.; Fuh, Y.; Lin, L. *Nano Lett.* 2010, **10**, 726.
79. Gao, Y. F.; Wang, Z. L. *Nano Lett.* 2007, **7**, 2499-2505.
80. Gao, Y.; Wang, Z. L. *Nano Lett.* **2009**, **9**, 1103-1110.
81. Hu, Y. *et al. Adv. Mater.* 2011, **23**, 4068-4071.
82. Xu, S.; Hansen, B. J.; Wang, Z. L. *Nat. Commun.* 2010, **1**, 93-97.
83. Periasamy, C.; Chakrabarti, P. J. *Appl. Phys.* 2011, **109**, 054306-054306-7.
84. Pal, U. *et al. Opt. Mater.* 2006, **29**, 65-69.
85. Tam, K. H. *et al. J. Phys. Chem. B* 2006, **110**, 20865-20871.
86. Fan, F. R., Tian, Z. Q.; Wang, Z. L. *Nano Energy* 2012, **1**, 328-334.
87. Fan, F. R. *et al. Nano Lett. Online* 2012.
88. Beeby, S. P. *et al. J. Micromech. Microeng.* 2007, **17**, 1257-1265.
89. Saha, C. R.; Donnell, T. O.; Wang, N.; McCloskey, P. *Actuat. A-Phys.* 2008, 147, 248-253.
90. Jeon, Y. B.; Sood, R.; Jeong, J.; Kim, S. *Sensor. Actuat. A-Phys.* 2005, **122**, 16-22.

91. Mitcheson, P. D. *et al. Sensor. Actuat. A-Phys.* 2004, **115**, 523-529.
92. Basset, P. *et al. J. Micromech. Microeng.* 2009, **19**, 115025.
93. Beeby, S. P.; Tudor, M. J.; White, N. M. *Meas. Sci. Technol.* 2006, **17**, 175-195.
94. Fang, H.; Wu, W.; Song, J.; Wang, Z. L. *J. Phys. Chem. C.* 2009, **113**, 16571-16574.
95. Castle, G. S. P. *J. Electrostat.* 1997, **40-41**, 13-20.
96. Nemeth, E.; Albrecht, V.; Schubert, G.; Simon, F. *J. Electrostat.* 2003, **58**, 3-16.
97. Lungu, M. *Miner. Eng.* 2004, **17**, 69-75.
98. Cross, J. A. *Electrostatics: Principles, Problems and Applications.* Adam Hilger Chap. 2. (1987).
99. Whitesides, F., Wollmann, D., Terris, B. D.; Diaz, A. F. *Langmuir* 1992, **8**, 1199-1203.
100. Lee, L. H. *J. Electrostat.* 1994, **32**, 1-29.
101. Watson, P. K.; Yu, Z. Z. *J. Electrostat.* 1997, **40-41**, 67-72.
102. Pelrine, R. *et al. Proc. SPIE* 2001, **4329**, 148-156.
103. Miao, P. *et al. Microsyst. Technol.* 2006, **12**, 1079-1083.
104. Sari, I.; Balkan, T.; Kulah, H. *Sensor. Actuat. A* 2008, **145-146**, 405-413.
105. Vullers, R. J. *et al. Solid State Electron.* 2009, **53**, 684-693.
106. Roundy, S. *et al. Lect. Notes Comput. Sc.* 2004, **2920**, 1-17.
107. Lee, M. *et al. Energy Environ. Sci.* 2011, **4**, 3359-3363.
108. Li, Z. *et al. Adv. Mater.* 2010, **22**, 2534-2537.
109. Zhu, G. *et al. Nano Lett.* 2012, **12**, 3086-3090.
110. Paradiso, J. A.; Starner, *IEEE Pervas. Comput.* 2005, **4**, 18-27.
111. Guang, Z.; Yang, R.; Wang, S.; Wang, Z. L. *Nano Lett.* 2010, **10**, 3151-3155.
112. Slade, J. R.; Bowman, J.; Kornbluh, R. *Proc. SPIE* 2012, **8383**, 83830R1-83830R12.

113. Chiba, S.; Waki, M.; Kornbluh, R.; Pelrine, R. *Proc. SPIE* 2008 **6927**, 6927151-6927159 .
114. Kornbluh, R. *et al. Proc. SPIE* 2011, **7976**, 7976051-79760519.
115. Zhu, G. *et al. Nano Lett.* 2012, **12**, 4960-496.
116. Whitesides, G. M.; McCarty, L. S. *Angew. Chem. Int. Ed. Engl.* 2008, **47**, 2188-2207.
117. Lowell, J.; Rose-Innes, A. C. *Adv. Phys.* 1980, **29**, 947-1023.
118. Horn, R. G.; Smith, D. T. *Science* 1992, **256**, 362-364.
119. Horn, R. G.; Smith, D. T.; Grabbe, A. *Nature* 1993, **366**, 442-443.
120. Diaz, A. F.; Guay, J. *IBM J. Res. Dev.* 1993, **37**, 249-259.
121. Davies, D. K. J. *Phys. D: Appl. Phys.* 1969, **2**, 1533-1537.
122. Duke, C. B. J. *Appl. Phys.* 1978, **49**, 315-321.
123. Wiles, J. A.; Grzybowski, B. A.; Winkleman, A.; Whitesides, G. M. *Anal. Chem.* 2003, **75**, 4859-4867.
124. McCarty, L. S.; Winkleman, A.; Whitesides, G. M. *J. Am. Chem. Soc.* 2007, **129**, 4075-4088.
125. McCarty, L. S.; Whitesides, G. M. *Angew. Chem. Int. Ed.* 2008, **47**, 2188-2207.
126. Soh, S. *et al. J. Am. Chem. Soc.* 2012, **134**, 20151–20159.
127. Kwetkus, B. A. *Part. Sci. Technol.* 1998, **16**, 55-67.
128. Schein, L. B. *Electrophotography and Development Physics*, Laplacian Press, Morgan Hill (1996).
129. Pai, D. M.; Springett, B. E. *Rev. Mod. Phys.* 1993, **65**, 163-211.
130. Grzybowski, B. A. *et al. Nat. Mater.* 2003, **2**, 241-245.
131. Grzybowski, B. A.; Wiles, J. A.; Whitesides, G. M. *Phys. Rev. Lett.* 2003, **90**, 083903-1-4.
132. Kumar, A. *et al. Adv. Mater.* 2001, **13**, 341–344.

133. Tien, J.; Terfort, A.; Whitesides, G. M. *Langmuir* 1997, **13**, 5349–5355.
134. Caruso, F.; Lichtenfeld, H.; Giersig, M.; Mohwald, H. J. *Am. Chem. Soc.* 1998, **120**, 8523–8524.
135. Kalsin, A. M. *et al. Science* 2006, **312**, 420-424.
136. Bishop, K. J. M.; Grzybowski, B. A. *ChemPhysChem* 2007, **8**, 2171-2176.
137. Kalsin, A. M.; Grzybowski, B. A. *Nano Lett.* 2007, **7**, 1018-1021.
138. Liu, C.-Y.; Bard, A. J. *Nat. Mater.* 2008, **7**, 505-509.
139. Liu, C.-Y.; Bard, A. J. *J. Am. Chem. Soc.* 2009, **131**, 6397-6401.
140. Liu, C.-Y.; Bard, A. J. *J. Chem. Phys. Lett.* 2010, **485**, 231-234.
141. Baytekin, B.; Baytekin, H. T.; Grzybowski, B. A. *J. Am. Chem. Soc.* 2012, **134**, 7223–7226.
142. Law, M. *et al. Nat. Mater.* 2005, **4**, 455-459.
143. Brabec, C. J.; Sariciftci, N. S.; Hummelen, J. C. *Adv. Funct. Mater.* 2001, **11**, 15-26.
144. Huynh, W. U.; Dittmer, J. J.; Alivisatos, A. P. *Science* 2002, **295**, 2425-2427.
145. Dodge, F. A.; Frankenhauser, B. J. *Physiol.* 1958, **143**, 76-90.
146. Raymond, S. A. *J. Physiol.* 1979, **290**, 273-303.
147. Frankenhauser, B. J. *J. Physiol.* 1957, **135**, 550-552.
148. Schalow, G.; Schmidt, H. *Pflugers Arch.* 1977, **372**, 17-22.
149. Chandrasekar, M. S.; Pushpavanam, M. *Electrochim. Acta* 2008, **53**, 3313-3322.
150. Kelly, J. J., Bradley, P. E.; Landolt, D. J. *Electrochem. Soc.* 2000, **147**, 2975-2980.
151. Kollia, C.; Loizos, Z.; Spyrellis, N. *Surf. Coat. Technol.* 1991, **45**, 155-160 .
152. Alfantazi, A. M.; Brehaut, G.; Erb, U. *Surf. Coat. Technol.* 1997, **89**, 239-244 .